2018

CHARACTERIZATION OF METHANE-AIR DIFFUSION FLAMES FOR FLAME SYNTHESIS APPLICATION THROUGH OPTICAL DIAGNOSTICS

Zhaojin Diao
University of Kentucky, zhaojindiao@gmail.com
Digital Object Identifier: https://doi.org/10.13023/etd.2018.324

STUDENT AGREEMENT:

I represent that my thesis or dissertation and abstract are my original work. Proper attribution has been given to all outside sources. I understand that I am solely responsible for obtaining any needed copyright permissions. I have obtained needed written permission statement(s) from the owner(s) of each third-party copyrighted matter to be included in my work, allowing electronic distribution (if such use is not permitted by the fair use doctrine) which will be submitted to UKnowledge as Additional File.

I hereby grant to The University of Kentucky and its agents the irrevocable, non-exclusive, and royalty-free license to archive and make accessible my work in whole or in part in all forms of media, now or hereafter known. I agree that the document mentioned above may be made available immediately for worldwide access unless an embargo applies.

I retain all other ownership rights to the copyright of my work. I also retain the right to use in future works (such as articles or books) all or part of my work. I understand that I am free to register the copyright to my work.

REVIEW, APPROVAL AND ACCEPTANCE

The document mentioned above has been reviewed and accepted by the student's advisor, on behalf of the advisory committee, and by the Director of Graduate Studies (DGS), on behalf of the program; we verify that this is the final, approved version of the student's thesis including all changes required by the advisory committee. The undersigned agree to abide by the statements above.

Zhaojin Diao, Student

Dr. Michael Winter, Major Professor

Dr. Alexandre Martin, Director of Graduate Studies

CHARACTERIZATION OF METHANE-AIR DIFFUSION FLAMES FOR FLAME SYNTHESIS APPLICATION THROUGH OPTICAL DIAGNOSTICS

DISSERTATION

A dissertation submitted in partial fulfillment of the
requirements for the degree of Doctor of Philosophy in the
College of Engineering
at the University of Kentucky

By

Zhaojin Diao

Lexington, Kentucky

Co-Directors: Dr. Michael Winter, Assistant Professor of Mechanical Engineering
and Dr. Kozo Saito, Professor of Mechanical Engineering

Lexington, Kentucky

ABSTRACT OF DISSERTATION

CHARACTERIZATION OF METHANE-AIR DIFFUSION FLAMES FOR FLAME SYNTHESIS APPLICATION THROUGH OPTICAL DIAGNOSTICS

Flame synthesis is a growing field of research aiming at forming new materials and coatings through injection of seed materials into a flame. Accurate prediction of the thermal structure of these flames requires detailed information on the radiative properties and a thorough understanding of the governing combustion processes. The objective of this work is to establish a basic optical diagnostic characterization of different methane-air diffusion flames of different complexity. The basic principles are developed and demonstrated at a rotational symmetric co-flow burner and finally applied to a burner consisting of six clustered microflames which is designed for future flame synthesis work. This work focuses on the demonstration of the optical techniques for characterizing the optical emissions from diffusion flames and of the proposed method for the determination of radiating species properties from these optical measurements.

In the co-flow diffusion flame setup, the fuel of methane diluted with nitrogen is provided through an inner tube while the air is applied through an outer duct surrounding the fuel nozzle. Filtered imaging and spectrally resolved measurements of the chemiluminescence of CH^* and C_2^* and of water emission were conducted. A procedure for using the HITRAN database to support the spectroscopic analysis of the water emission was developed.

In the six clustered microflames burner setup, the burner consisted of six micro-nozzles arranged in a circle surrounding a central nozzle through which air and TaN seed particles with sizes between 0.3 and 3 μm were injected. Spectrally resolved measurements of the chemiluminescence of CH^* and C_2^* were conducted for temperature measurements. Imaging results obtained from a spectral integration of the molecular emission were compared to results from Japanese collaborators who applied a tomographic analysis method to filtered emission measurements of CH^* emission which can yield spatially resolved three dimensional mapping of the flame front. The analysis of the spatial distribution of the integrated band emission

of CH^* and C_2^* showed that the emission of both species is generated at the same locations in the flame which are the thin flame sheets shown in the tomography results of CH^*. The ratio of the C_2^* and the CH^* emission from the emission spectroscopy measurements was used to determine a local equivalence ratio through empirically derived correlations for premixed flames reported in literature. Rotational and vibrational temperature distributions of CH^* and C_2^* radicals throughout the entire flame were determined from the spectrally resolved emission from CH^* and C_2^*. The temperatures of TaN seed particles were characterized using VIS-NIR emission spectra while varying fuel-air flow rates. The temperature profiles of the particles at various heights above the base of the central nozzle, obtained by their VIS-NIR continuum emission, showed a well-defined constant temperature region that extended well beyond the actual flame front and changed as fuel and oxidizer flow rates were varied. The results demonstrate the ability to control the duration to which seed particles are subjected to high temperature reactions by adjusting fuel and oxidizer flow rates in the clustered microflames burner.

KEYWORDS: flame synthesis, optical diagnostics, molecular spectroscopy, microflames, temperature measurement

Zhaojin Diao
Student's Signature

July 25, 2018
Date

CHARACTERIZATION OF METHANE-AIR DIFFUSION FLAMES FOR FLAME SYNTHESIS APPLICATION THROUGH OPTICAL DIAGNOSTICS

By

Zhaojin Diao

Dr. Michael Winter
Co-Director of Dissertation

Dr. Kozo Saito
Co-Director of Dissertation

Dr. Alexandre Martin
Director of Graduate Studies

July 25, 2018
Date

To my family

ACKNOWLEDGEMENTS

I would like to foremost express my deepest gratitude to my advisor Prof. Michael Winter for your invaluable guidance and continued support without which I would not have been completed this study. Thank you for walking me through the ups and downs during my graduate study and personal life. I am very grateful to Prof. Kozo Saito for co-chairing my committee and for the great help throughout my research. I would also like to thank Profs. Brad Berron, David Murrugarra, Dusan Sekulic, and Kaveh Tagavi for being my committee members and providing valuable suggestions. I am also grateful to Prof. Taro Hirasawa from Chubu University, Japan for providing motivation and your microflames burner for this research, sharing your insights in this study, as well as for being as my external advisor.

I would also like to thank all my former and current colleagues from the Plasmadiagnostics lab. Helmut Koch, Robert Bickel, Bradley Butler, Christian Arnold, Julian Beyer and Ricky Green, thank you all for your support and friendship. A special thank you goes to Helmut Koch for helping me on experimental setups and sharing your scientific ideas, and most importantly, thank you for getting me into beer and bourbon!

Lastly, I would like to thank my parents and fiancée for your continued support and love.

TABLE OF CONTENTS

LIST OF TABLES

LIST OF FIGURES

NOMENCLATURE

Constants

c	speed of light in vacuum	2.99792×10^{8}	$m.s^{-1}$
c_2	second radiant constant	1.43878×10^{-2}	m.K
h	Planck's constant	6.62620×10^{-34}	J.s
k	Boltzmann's constant	1.38062×10^{-23}	$J.K^{-1}$
σ	Stefan-Boltzmann's constant	5.67036×10^{-8}	$W.m^{-2}.K^{-4}$

Greek letters

α	absorptance	-
χ	particle size parameter	-
ε	emissivity	-
ε	emission coefficient	$W.m^{-3}.sr^{-1}$
ϕ	fuel-air equivalence ratio	-
η	frequency	Hz
κ	absorption coefficient	m^{-1}
λ	wavelength	nm
ν	wavenumber	cm^{-1}
ρ	reflectance	-
τ	transmittance	-

Latin letters

A	Einstein coefficient	s^{-1}
a	particle diameter	m
B	spectral radiance of a blackbody	$W.m^{-2}.sr^{-1}.m^{-1}$
d	blaze spacing	m
E	spectral radiance	$W.m^{-2}.m^{-1}$
E	excited energy	cm^{-1}
e	volumetric line intensity	$W.m^{-3}.sr^{-1}$

Fr	Froude number	-
g	multiplicity	-
I	radiative intensity of a real surface	$W.m^{-2}.sr^{-1}.m^{-1}$
m	order	-
Ma	Mach number	-
n	particle density	m^{-3}
N_L	Loschmidts number	$molecule.m^{-3}.atm^{-1}$
p	pitch size	mm
Q	partition function	-
Re	Reynolds number	-
S	HITRAN line intensity	$cm^{-1}/(molecule.cm^{-2})$
T	temperature	K
x	length of line of sight	m

List of abbreviations

bb	blackbody
CCD	charged coupled device
CARS	coherent anti-Stokes Raman spectroscopy
CMOS	complementary metal-oxide-semiconductor
$corr_\lambda$	correction factor
CT	computed tomography
DSLR	digital single-lens reflex camera
EDX	energy dispersed X-ray
FI-CT	filtered imaging for computed tomography
FTIR	Fourier-transform infrared spectroscopy
FWHM	full width at half maximum
LIF	laser-induced fluorescence
NIR	near-infrared
OES	optical emission spectroscopy
PIV	particle image velocimetry
SEM	scanning electron microscope

TC	thermal couple
VIS	visible
XPS	X-ray photon spectroscopy
XRD	X-ray diffractometer

Indices

’	upper state
”	lower state
i	lower state
k	upper state
ex	electronic excited state
*	excited state

INTRODUCTION

1.1 Background and Motivation

1.1.1 Flame synthesis

Flame synthesis is a growing field of research aiming at forming functional materials, catalysts, and coatings by seeding reactants into the high temperature reactive field of flames [1-9]. For catalysis, it is important not only to synthesize molecular structures, but also to achieve specific aggregate sizes and structures, requiring precise control of synthesis conditions and sampling processes. Various techniques like electrically assisted synthesis [3] and thermophoresis sampling [4] have been applied, and the governing processes of flame synthesis have been investigated [5, 6]. Flame synthesis has been shown to effectively synthesize nano-particles and nano-tubes [10-13] Hydrogen, methane and ethylene are the major fuels used in flame synthesis with air or oxygen being oxidants. Swihart et al. used titania, fumed silica and carbon blacks to synthesize nanoparticles [14]. Li et al. synthesized carbon nanotubes on Ni-alloy and Si-substrates using counter-flow methane-air diffusion flames [15]. As illustrated in Figure 1.1, a typical flame synthesis system has a precursor unit, a burner unit and a particle collection unit. A comprehensive review on flame synthesis can be found in [16].

Flame synthesis techniques requires high temperatures in a short time period as compared to other methods like furnace heating and chemical vapor deposition (CVD) [17, 18]. However, the attainable range of temperatures during flame synthesis is small compared to the range available with furnaces and CVD, and temperatures are not independently controlled from the reactions that occur in the flame [16, 19-21].

Two different types of flames, premixed and diffusion flames, have been used to synthesize materials [16, 19-22]. For both flames, synthesis temperature and species concentrations are the two major parameters to control the synthesis process. For

premixed flames, dilution of fuel is typically the main temperature control parameter which, however, can also change oxidizer concentrations and reaction process especially for oxidizing metals. For industrial applications, however, where safety is a major concern, diffusion flames are preferred over premixed flames. While a single co-flow diffusion flame is the simplest type of diffusion flame, its capability to control temperature may not be the most ideal without significantly changing species concentrations and flow profiles, which are not easily attained due to complex chemical reactions taking place in the flame. Therefore, it is deemed necessary to explore what kind of flames and burners can achieve the range of flame temperatures needed for advanced flame synthesis.

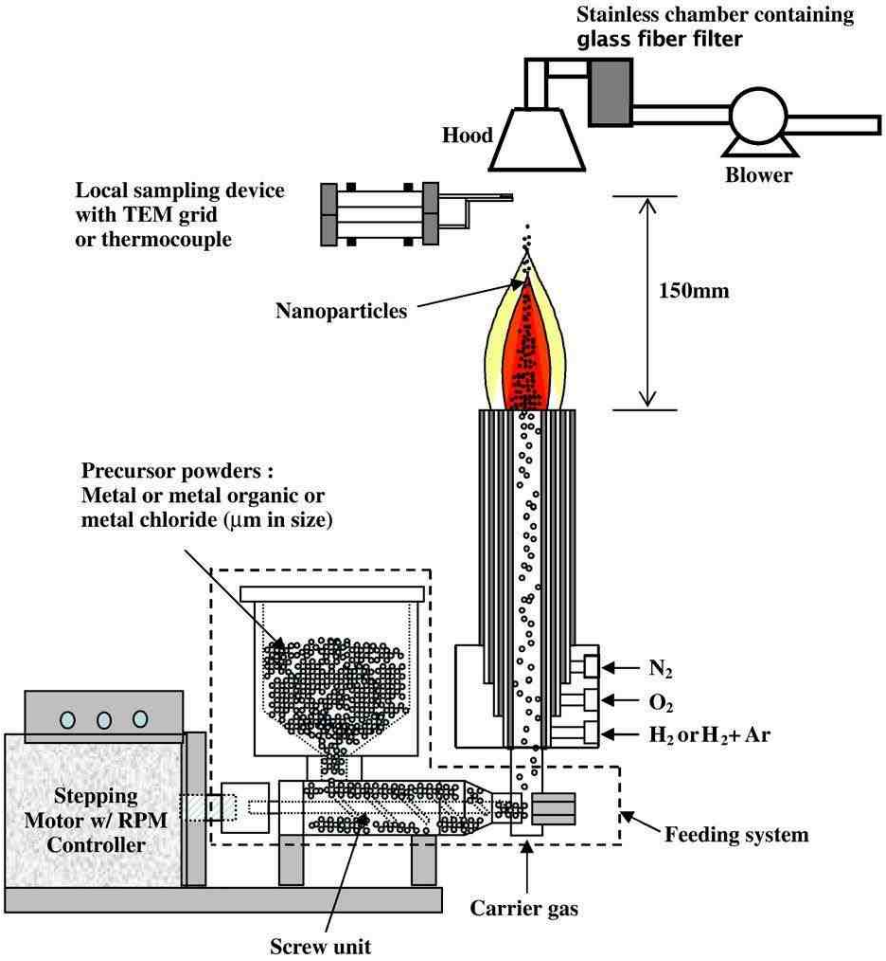

Figure 1.1 Typical flame synthesis system adopted from [23].

1.1.2 Why co-flow flame

The Co-flow laminar diffusion flame has been well investigated by researchers due to its essentially two dimensional axisymmetric configuration and relatively simple burner system [24-28]. This flame is typical of most practical combustion devices, and provides an easily accessible setup for experimental and numerical studies in a multi-dimensional structure to understand combustion processes. Walsh et al. generated profiles of the temperature, and major and minor species, and discussed issues related to the computation and measurement of CH, CH^*, and OH^* in an unconfined laminar flame [26]. Giassi et al. analyzed CH^* concentration and flame heat release rate in laminar co-flow diffusion flames under microgravity and normal gravity based on the use of DSLR camera [28]. In this study, the optical diagnostics technique was developed and first applied to the standard co-flow burner designed and developed by Yale University (called the Yale co-flow burner).

1.1.3 Why microflames

Small laminar diffusion flames having lateral dimensions on the order of a few millimeters behave differently from candle-like flames because buoyancy effects are negligible as a result of their small size [29]. Since the pioneer work on micro burner flames by Ban et al. [29] indicating that micro flames are momentum-diffusion (*Re* number) controlled, where gravity and adiabatic compression forces are secondary compared to the inertial and diffusion forces, further studies have been conducted on single micro flame [29-31], interaction between two identical microflames [32], six diffusion microflames [33-35], and 54 micro burner flames [36]. These studies revealed unique features of microflames which are different from normal centimeter-size diffusion flames where buoyancy effects are dominant.

Three pi-numbers (*Re*, *Fr*, and *Ma* number) for scale modeling analysis are considered in relation to these micro scale flames. Emori, Saito and Sekimoto provide comprehensive scale modeling theory and applications in their textbook

[37]. The Reynolds number *Re* is the ratio of inertial forces to viscous forces, the Froude number *Fr* is the ratio of inertial forces to gravity forces, and the Mach number *Ma* is the ratio of flow velocity to local speed of sound [38]. Microflames are controlled by the inertial force of incoming fuel flow which interacts with viscous forces of air when the fuel jets interact with air. Buoyancy force and compression force are minor with Frounde numbers [*Fr*: (inertia force)/(buoyancy force)] on the order of 10^3 and low Mach numbers [*Ma*: (compression force)/(inertial force)] on the order of 10^{-2} [29]. However, for certain pitch sizes and fuel/air flow rates, the buoyancy effect is not negligible due to the interactions between microflames. Hirasawa et al. [32] have reported that two different scales need to be considered on the transport process in the microflames; one being the fuel-jet scale and the other one the buoyance scale.

Although good progress has been made on studies on micro flames, it was pointed out by Hirasawa et al. [32, 33] that the behavior of clustered microflames is still required to be investigated in further detail such as obtaining thermodynamic states data on the clustered microflames, which will give us the gas phase temperature structure of the microflames. The interactions among these microflames were found to extend the extinction limit due to a significant change in species concentration [39]. The change of total heat release rate created by merging two identical micro-slot flames [40] suggested the shape of microflames can significantly influence the overall heat generation. The above findings associated with microflames' wide range in heat transfer and chemical reaction capability may help designing an environmentally friendly high energy efficient combustion system. The flame-merging effect is unique to micro scale flames and differs significantly from normal centimeter-size-flames, where the *Fr* number dominates. The suggested *Re* number for micro flames can be tested under micro gravity condition (space experiment) using centimeter-scale normal flames.

In the present study, flame temperatures and reaction-zone densities were controlled by creating selective flame structures using clustered microflames

burners [29, 32, 39]. That is because the clustered microflames provide very stable and steady flame condition with a relatively long residence time compared to counter-flow diffusion flames [20] and have a relatively small quenching region at the flame base compared to regular centimeter size co-flow diffusion flames [19]. The clustered microflames were also found to be capable of changing the reaction-zone distributions and densities by merging and bundling the individual microflames [32, 39]. Therefore, the clustered microflames can suit well to achieve the objectives for flame synthesis due to their wide range of controllable temperatures and the extended heating duration range. In addition, an air-jet seeding nozzle was added at the center of the microflames to better control reaction-zone structure. Its unique 3-D non-sooting flame structure is expected to enhance the performance of flame synthesis and micro heat exchangers [41].

1.1.4 Gas temperature

The emission spectra of the laminar non-sooting methane-air diffusion microflames were dominated by molecular spectra of OH, C_2, CH, CO_2, and water [34]. The emission from the primary reaction zone in the visible wavelength range is often much stronger than that from the burnt gases above because radicals like CH and C_2 are only present in the reaction zone [42]. The C_2 Swan band emissions, for example, are present in many flames [43-45] and also in plasma research of carbon composite thermal protection systems [46, 47]. The diatomic spectra originating from electronically excited states (CH^*, C_2^* and OH^*, where * denotes the excited state), however, have excitation energies which are too high to be populated through thermal excitation of ground state molecules in the flames under investigation. Therefore, the population of the electronic states likely occurs as a by-product of the chemical reactions during combustion, whose resulting emission process is called chemiluminescence [44, 48]. An interesting and important point here is that, since the population of these excited states is produced through the chemical reactions in combustion, the emitted radiation signals inherently contain

information about the combustion process itself, as can be seen in a pioneer study by Nori et al. [43] on modeling reaction kinetics of the chemiluminescence effects. In plasma applications, collisional radiative modeling has been proven useful for interpreting measured emission spectra, providing a way to validate numerical simulation, even under non-equilibrium conditions [49]. Similarly, the emission spectroscopy measurement data of chemiluminescence products may be used to validate numerical modeling of combustion processes. Indeed, several studies [50-52] provide empirical relations to interpret the ratio of the emission from electronically excited states of different molecules in terms of equivalence ratio, therefore providing a new database for interpreting basic combustion processes.

For the gas temperature of the flame, the chemiluminescence was used to determine molecular spectra obtained from electronically excited CH radicals within the methane-air flames. The CH^* chemiluminescence is frequently used in flame diagnostics to predict heat release rates [43, 53] and identify the location of reaction zones [44, 48]. Three systems of CH are observed in flames, the 431.5 nm system due to the CH $A^2\Delta$-$X^2\Pi$ transition [44] being the strongest one. Here, the spectral shape of these molecular bands in high spectral resolution was used to determine rotational and vibrational temperatures of this molecule, the former one representing the flame temperature.

1.1.5 Temperature measurement methods

Accurate measurement of temperature, one of the most important parameters in the flame synthesis and also in combustion research, requires a minimum disturbance of the sensitive area where an active synthesis takes place [19-21]. To achieve that goal, non-intrusive measurements are preferred over intrusive measurements.

It is important to provide the current status of the most typical baseline intrusive temperature measurement, thermocouples. It uses thermo-electrical effect to generate potential or electric current between the well regulated referenced point

temperature and the measurement temperature. However, the thermocouple temperature measurement technique contains errors associated with radiation loss from the heated thermocouple bead, and heat conduction loss through the thermocouple wire when it experiences temperature variation along the wire. It may be possible to estimate these errors to obtain absolute temperature [54]. However, and most importantly, the thermocouple technique is not suitable for measuring non-equilibrium gas temperature, unsteady and unstable flames such as pulsating flames and rapidly expanding flames, and flames which has steep temperature gradient, due to the limitations of thermocouple's time constant, spatial resolution, and radiation and conduction errors mentioned in the above. However, due to the recent progress in combustion and energy research, the above type of data and information are more than ever required to improve the efficiency of power generation systems.

To meet these challenges, researchers have made efforts to develop reliable and accurate non-intrusive temperature measurement techniques, for example, Raman spectroscopy, CARS, [4, 55-57] and FTIR [4, 5], but as of today none has satisfied a highly accurate, reliable and easy to use standard requirement. Therefore, there is the strong need to develop such a non-intrusive temperature measurement technique that can satisfy the above criteria.

1.1.6 CT methods

In combustion, computed tomography (CT) has been widely used in thermometry [58, 59]. Ishino et al [35] have applied CT to chemiluminescence for 3D observation of high speed turbulent flames, by using a multi-directional quantitative schlieren system with flash light source. The line-of-sight character of emission spectroscopy, which normally prevents achieving spatial resolution along the line-of-sight, was compensated through upfront knowledge of the flame structure from the filtered imaging experiments [35, 60]. Spectrally integrated intensities similar to filtered imaging data from the emission spectroscopy measurement data were extracted to

show the similarity of the flame structure observed from the CH^* and C_2^* emission. The combination of emission spectroscopy and tomography techniques applied to filtered imaging measurements is a potentially powerful tool to access both structure and thermodynamic properties of flames with rather basic diagnostic techniques [60].

1.1.7 Three major assumptions for determining particle temperature

In this work, the surface temperature of small particles seeded into the flame surrounded by hot combustion gas is of the primary interest. In the infrared region, researches on soot [61] and carbon particles [62] through FTIR techniques were reported. In this work, however, attention was paid to a spectroscopic approach in the visible to near infrared wavelength region. Saito et al. showed that soot particles in the yellow zone of small laminar diffusion flames are hotter than the surrounding gas temperature [20]. Therefore, it is necessary to independently measure the surface temperature of the particles and gas temperature. To satisfy the need for particle surface temperature determination, a passive spectroscopic temperature measurement technique was successfully explored, which was based on spectral shape of the emission between 600 and 1,000 nm from the TaN particles along the centerline of the clustered microflames.

The application of measuring the temperature of a particle stream through fitting a Planck spectrum requires the careful assessment of several assumptions. In particular, spectral surface emissivity as a function of surface temperature, the quantification of the influence of scattering, and potential changes of the surface properties when the particles pass through the flame such as oxidation of the original surface material.

Initially experiments with Al_2O_3 were conducted but it was found that, due to the low emissivity of Al_2O_3 in the targeted wavelength range, the thermal emission was too weak for detection with a sufficient signal to noise ratio. TiO_2 also suffers from a low emissivity problem. To overcome these problems, finally TaN particles were

found to be able to withstand high temperatures while showing high and known spectral emissivities which are available from literature and are crucial information for the subsequent analysis. Therefore, TaN particles were chosen for these experiments. Although these particles were not intended as a target for flame synthesis, they were used for characterization of achievable particle temperatures.

The influence of scattering was assessed through theoretical considerations based on the measured particle size distribution, and confirmed through transmission measurements. The spectral shape of the thermal emission was used to determine the particle temperature instead of the absolute intensities since the results become widely independent from particle size and density. Temperature dependent spectral emissivities of TaN based on literature data were taken into account during the fitting process.

Potential influences of surface oxidation were taken into account by adapting reported oxide transmission values to thin oxidation layers and including their influence on the spectral shape into the spectral fitting procedure as well. The average oxide layer thickness was obtained for all investigated locations in the particle stream by this unique process of estimating an oxidation layer thickness from the spectral shape of the emitted thermal radiation.

1.2 Objectives of Research

For the design of suitable flame synthesis and micro heat exchanger processes, a thorough characterization of the microflames in terms of flame geometry, type of flame (either diffusion or premixed), temperature, and species concentration is needed. Researchers [34, 50, 51, 53, 63] showed that molecular emission spectra, gathered with non-intrusive optical emission spectroscopy (OES) techniques, can be used to diagnose structures of combustion and plasma systems.

In this work, several hypotheses were made: First, it is hypothesized the optical emission spectroscopy is an applicable optical diagnostics tool for flame and seeding

particle temperature measurements. The rotational symmetric co-flow diffusion flame provides an essentially accessible setup for assessing the developed optical diagnostics for radiation measurements and application of the simulation of molecular emission. Fundamental physics, *e.g.* blackbody radiation and molecular emission, lays the basics for determining radiation intensity and temperature. Also, it is hypothesized that the clustered microflames burner is a good candidate for flame synthesis applications. These clustered microflames show a significant change of the flame structure due to the flames merging, which then yields a wide range of heating capacity.

Therefore, the objectives of this work were: to develop a reliable optical diagnostic method to measure the temperatures of micron-size particles with known emissivity in flames, to determine the flame temperature by measuring the spectral and spatial distribution of the chemiluminescence of CH^* and C_2^* radicals, by determining the rotational/vibrational temperatures of these two radicals through emission spectroscopy techniques, and to investigate the thermal structure and temperature range of clustered microflames for future application to flame synthesis. The latter point involved to further characterize the current 3-D flame structure generated by the six clustered microflames under variation of burner pitch (*i.e.* the distance between the individual nozzles) at different airflow conditions by analyzing the ratio of CH^* and C_2^* emission to give information about the flame type through the local equivalence ratio.

In parallel to this study, independent investigation of the six clustered microflames through computed tomography and particle image velocimetry (PIV) methods was also carried out in Japan. Kato et al [60] measured the axial velocity distribution of the particle stream with PIV techniques. To investigate the complex three dimensional flame shape, a computed tomography (CT) method developed by Ishino based on filtered imaging of the CH^* emission was also applied [60].

The following chapters describe the experimental methods which are followed by experimental results and discussions to achieve these objectives.

1.3 Outline of Dissertation

The structure of this dissertation is in the following manner.

Chapter 2 reviews the background theory used in this study including brief discussion of combustion, thermal radiation and molecular spectroscopy, and application of HITRAN simulation.

Chapter 3 reviews the experimental methods including optical techniques and data process procedures.

Chapter 4 reviews the characterization of a Yale co-flow methane-air diffusion non-sooting flame through reconstructed local spectrally resolved CH^* and C_2^* chemiluminescence emission intensity.

Chapter 5 reviews the characterization of six clustered methane-air diffusion non-sooting microflames through spectrally resolved CH^* and C_2^* chemiluminescence.

Chapter 6 reviews the characterization of six clustered methane-air diffusion non-sooting microflames through TaN seed particle.

Chapter 7 summarizes the results from current work and suggestions for future directions.

BACKGROUND THEORY

2.1 Combustion Mechanism

Combustion is exothermic chemical reactions in flow with heat and mass transfer [64, 65]. Combustion processes are often categorized as premixed or non-premixed (diffusion). A premixed flame is flame that the fuel and oxidizer are well mixed initially before they reach the flame front. Premixed flame has ability to propagate perpendicular to itself with a burning velocity that depends on the thermal and chemical conditions of the unburned premixed gas for instance convection-diffusion-reaction balance. Bunsen burner is a classical device to generate laminar and stationary premixed flame [66]. A diffusion flame is a flame that the fuel and oxidizer are supplied from different origins [67]. In diffusion flame, combustion occurs at the flame surface only where the fuel meets oxidizer in an appropriate concentration. The flame speed is limited by the rate of diffusion since the fuel and oxidizer are mixed by diffusion. Also, diffusion flame tends to produce more soot than premixed flame due to the fact that there may not be sufficient oxidizer for the complete combustion.

Stoichiometric combustion is the ideal combustion process such that fuel is combusted completely, *i.e*, species react in exact proportions. To determine the excess air or excess fuel for a combustion gas mixture, the fuel-air equivalence ratio is introduced as:

$$\phi = \frac{\left(n_{\text{fuel}} / n_{\text{air}}\right)_{\text{actual}}}{\left(n_{\text{fuel}} / n_{\text{air}}\right)_{\text{stoi}}} \tag{2.1}$$

where n is the number of moles, and *stoi* is the stoichiometry with $\phi < 1$ being fuel-lean (or lean) combustion, $\phi = 1$ being stoichiometric combustion, and $\phi > 1$ being fuel-rich combustion.

2.2 Thermal Radiation

Thermal radiation is often called blackbody radiation where a blackbody is an idealized physical body that absorbs all the incident light. The spectrum and intensity of the blackbody radiation depends solely on the blackbody temperature [68]. The spectral radiance of a blackbody at a given temperature T as a function of wavelength λ, wavenumber ν, and frequency η are described by Planck's law [68]:

$$B_{\lambda}(\lambda,T)=\frac{2hc^{2}}{\lambda^{5}}\frac{1}{\exp\left(\frac{hc}{\lambda kT}\right)-1} \qquad \left[\frac{\mathrm{W}}{\mathrm{m^{2}.sr.m}}\right] \tag{2.2}$$

$$B_{\nu}(\nu,T)=2hc^{2}\nu^{3}\frac{1}{\exp\left(\frac{hc\nu}{kT}\right)-1} \qquad \left[\frac{\mathrm{W}}{\mathrm{m^{2}.sr.m^{-1}}}\right] \tag{2.3}$$

$$B_{\eta}(\eta,T)=\frac{2h\eta^{3}}{c^{2}}\frac{1}{\exp\left(\frac{h\eta}{kT}\right)-1} \qquad \left[\frac{\mathrm{W}}{\mathrm{m^{2}.sr.Hz}}\right] \tag{2.4}$$

where h, c, k are Planck's constant 6.626 x 10^{-34} [J.s], the speed of light 2.998 x 10^{8} [m/s] and the Boltzmann constant 1.3807 x 10^{-23} [J/K], respectively.

By multiplying the total solid angle of a sphere of 4π [Steradian], the spectral irradiance is written as:

$$E_{b\lambda}(\lambda,T)=\frac{8\pi hc^{2}}{\lambda^{5}}\frac{1}{\exp\left(\frac{hc}{\lambda kT}\right)-1} \qquad \left[\frac{\mathrm{W}}{\mathrm{m^{2}.m}}\right] \tag{2.5}$$

$$E_{b\nu}(\nu,T)=8\pi c^{2}\nu^{3}\frac{1}{\exp\left(\frac{hc\nu}{kT}\right)-1} \qquad \left[\frac{\mathrm{W}}{\mathrm{m^{2}.m^{-1}}}\right] \tag{2.6}$$

$$E_{b\eta}(\eta,T)=\frac{8\pi h\eta^3}{c^2}\frac{1}{\exp\left(\frac{h\eta}{kT}\right)-1}\qquad\left[\frac{\mathrm{W}}{\mathrm{m}^2.\mathrm{Hz}}\right]\tag{2.7}$$

Regardless of different spectral irradiance expressions, the total emissive power shall be the same. Therefore, the total blackbody emissive power can be determined by integrating one of above spectral irradiance formula over corresponding spectral variables from zero to infinity:

$$E_b(T)=\int_0^\infty E_{b\lambda}d\lambda=\int_0^\infty E_{b\nu}d\nu=\int_0^\infty E_{b\eta}d\eta\qquad\left[\frac{\mathrm{W}}{\mathrm{m}^2}\right]\tag{2.8}$$

$$E_b(T)=\frac{2\pi^5k^4}{15h^3c^2}T^4\qquad\left[\frac{\mathrm{W}}{\mathrm{m}^2}\right]\tag{2.9}$$

The total blackbody emissive power is proportional to the fourth power of the temperature. This integral constant is known as the Stefan-Boltzmann constant:

$$\sigma=\frac{2\pi^5k^4}{15h^3c^2}=5.670\times10^{-8}\qquad\left[\frac{\mathrm{W}}{\mathrm{m}^2.\mathrm{K}^4}\right]\tag{2.10}$$

To find the maximum spectral irradiance, the first derivative of equation (2.5) is built to be zero as:

$$\frac{d}{d\lambda}\left(\frac{8\pi hc^2}{\lambda^5}\frac{1}{\exp\left(\frac{hc}{\lambda kT}\right)-1}\right)=0\tag{2.11}$$

Numerical analysis leads to

$$\lambda_{max} \cdot T = 2898 \qquad [\mu m.K] \tag{2.12}$$

which is known as Wien's displacement law that dictates the shift of the peaks of the blackbody radiation spectra.

Figure 2.1 shows a typical blackbody emissive power spectrum. The peak of solar emission spectrum is observed at about 0.5 μm. The spectra at different temperatures never overlap. The red dashed line represents the Wien's displacement law.

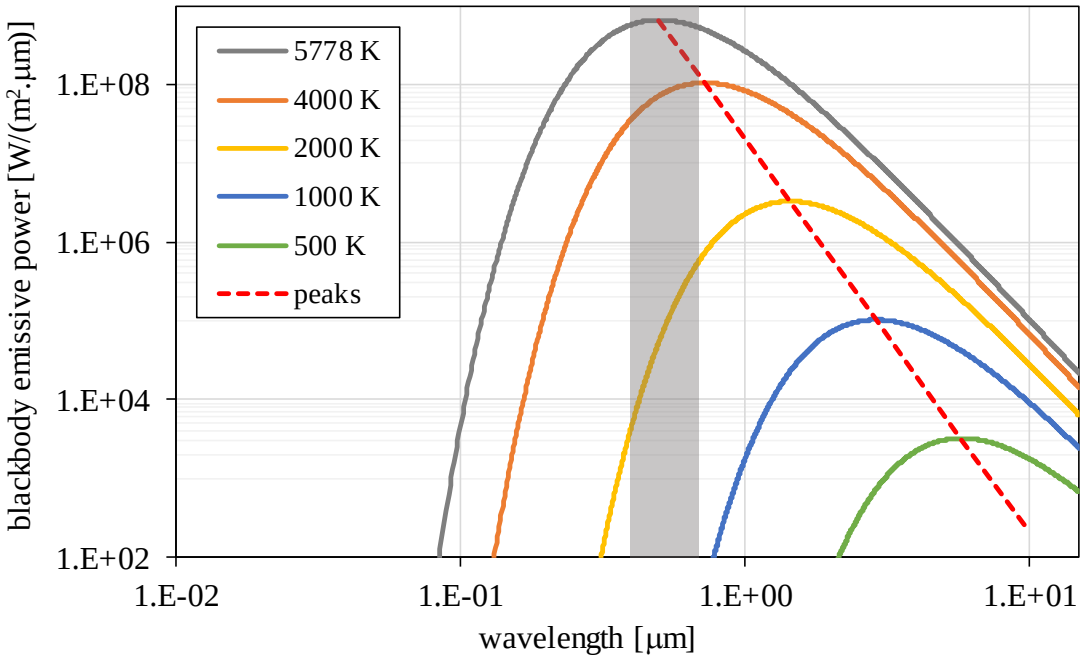

Figure 2.1 Blackbody emissive power spectrum.

Some additional fundamental radiation properties used for analysis in this work are summarized as [68]:

$$\text{Reflectance,} \qquad \rho = \frac{\text{energy reflected}}{\text{incoming energy}} \tag{2.13}$$

$$\text{Absorptance,} \qquad \alpha = \frac{\text{energy absorbed}}{\text{incoming energy}} \tag{2.14}$$

$$\text{Transmittance,} \qquad \tau = \frac{\text{energy transmitted}}{\text{incoming energy}} \tag{2.15}$$

where the ratio values are from 0 to 1.

Another important non-dimensional number is emissivity which measures how efficient the surface of a material is able to emit radiation energy compare to energy emitted from a blackbody surface at the same temperature:

$$\varepsilon = \frac{\text{energy emitted from a surface}}{\text{energy emitted from a blackbody surface}} \tag{2.16}$$

In thermal equilibrium, blackbody is an ideal emitter that defines the upper limit of energy emitted from a surface. Therefore, the ratio value is from 0 to 1. And the spectral hemispherical emissivity is defined as [68]:

$$\varepsilon_\lambda(\lambda, T) = \frac{I_\lambda(\lambda, T)}{B_\lambda(\lambda, T)} \tag{2.17}$$

where I_λ and B_λ are the radiative intensity of a real surface and a blackbody surface, respectively.

For a gaseous/opaque medium, the incident radiation is attenuated by absorption is described by Beer-Lambert law:

$$\tau_\lambda = e^{-\kappa_\lambda \cdot x} \tag{2.18}$$

where x is the thickness of the layer and κ_λ is the spectral absorption coefficient.

Therefore, the spectral intensity along the path x attenuated by absorption and augmented by emission is written as [69]:

$$I_\lambda(x) = I_\lambda(0)e^{-\kappa_\lambda \cdot x} + B_\lambda\left(1 - e^{-\kappa_\lambda \cdot x}\right) \quad \left[\frac{\mathrm{W}}{\mathrm{m^2.sr.m}}\right] \tag{2.19}$$

When electromagnetic wave travels in a medium with small particles, the radiation intensity may be altered by scattering due to three separate phenomena: (1) diffraction, (2) reflection and (3) refraction as shown in Figure 2.2 [70].

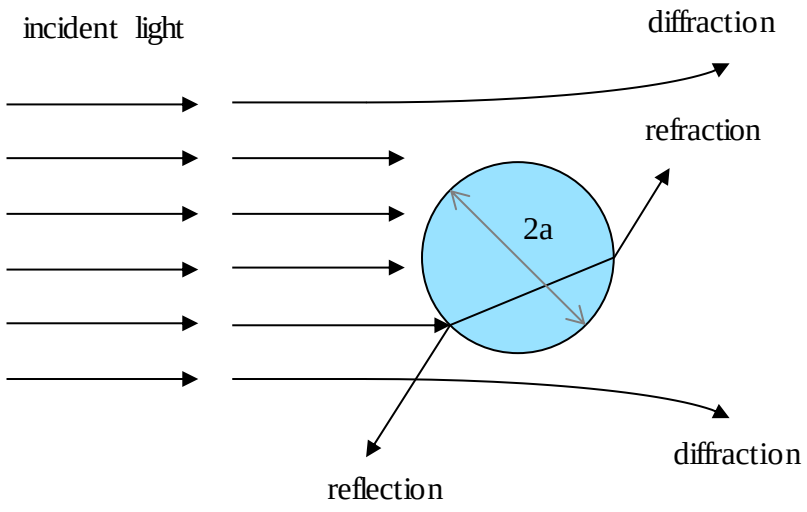

Figure 2.2 Interaction between electromagnetic wave and spherical particles adopted from [70].

The nature of the scattering is controlled by the relative size of the particles compared to the wavelength of the radiation, which can be characterized by the

particle size parameter χ defined by the effective projected area of the particle and the wavelength of light potentially to be scattered [68, 71-73]. Following the definition in [74], χ can be calculated as:

$$\chi = \frac{2\pi a}{\lambda} \tag{2.20}$$

where a is the effective particle radius and λ is the wavelength of the light. For very small particles ($\chi << 1$), Rayleigh scattering is dominant [75], *e.g.*, blue skies, res sunsets and rainbow are attributed the sun light scattered by the atmosphere. With soot particles, χ is often on the order of 1 and the major scattering mechanism is given by Mie scattering [76]. For large particles ($\chi >> 1$), the major influence on transmitted radiation is absorption as the light encounters the particles.

2.3 Spectroscopy

Electrons rotate on certain orbits around a nucleus according to defined energy levels. The radiation is emitted or absorbed when they transit from one level to another. The energy emitted or absorbed by a photon is:

$$\Delta E = h\eta \quad [\mathrm{J}] \tag{2.21}$$

where h and η are Planck's constant 6.626 x 10^{-34} [J.s] and photon's frequency [s^{-1}].

The emission coefficient is calculated as:

$$\varepsilon = \frac{h\eta}{4\pi} A_{ki} n_k \quad [\frac{\mathrm{W}}{\mathrm{m}^3.\mathrm{sr}}] \tag{2.22}$$

where 4π is the solid angle into full space of the unity sphere [sr], A_{ki} is the Einstein probability for spontaneous emission from upper state k to lower state i [s^{-1}] and n_k

is the particles density at state k [m^{-3}]. By multiplying emission coefficient with its depth (length of the line of sight), the radiative intensity is obtained.

The total particles density n_k at state k is related to total density of species under consideration n_o by the Boltzmann distribution:

$$n_k = \frac{g_k}{\sum_i g_i \exp\left(-\frac{E_i}{kT_{ex}}\right)} n_o \exp\left(-\frac{E_k}{kT_{ex}}\right) \qquad [m^{-3}] \tag{2.23}$$

where g_k and g_i are the degeneracy of the state k and i, E_k and E_i are the excitation energy of the state k and i, T_{ex} is the electronic excitation temperature, k is the Boltzmann constant. For molecular radiation, the energy change is caused by the electronic level, the vibrational level, and the rotational level of excitation simultaneously.

Chemiluminescence is the emission of light from a chemical reaction which produces the electronic excited state products. Chemiluminescence is a powerful tool for combustion diagnostics [43]. For instance, in a methane-air diffusion flame, CH^* is produced form the chemical reaction of the ethynyl radical with monoatomic and diatomic oxygen [26]:

$$C_2H + O_2 \leftrightarrow CH^* + CO_2 \tag{2.24}$$

$$C_2H + O \leftrightarrow CH^* + CO \tag{2.25}$$

Then the emission of light is from destruction reaction:

$$CH^* \rightarrow CH + h\nu(\text{light}) \tag{2.26}$$

Most of the studies have shown that the formation of the C_2^* is from the following reactions [77]:

$$CH_2 + C \rightarrow H_2 + C_2^* \quad (2.27)$$

$$CH + C \rightarrow H + C_2^* \quad (2.28)$$

Emission and absorption lines can be broadened through different processes with the following being three major processes [78]: natural line broadening, collision broadening, and Doppler broadening. Natural line broadening is attributed to Heisenberg uncertainty principle such that the energy of emitted photons from spontaneous emission varies slightly causing the spectral lines broadened since the transition energy cannot be the same. Collision broadening is also referred as pressure broadening due to the frequency of collisions among gas molecules. Both natural line broadening and collision broadening line shapes can be described by Lorentzian line profile. Doppler broadening is also referred as thermal broadening due to varied thermal motions of emitters causing Doppler effect in the direction of observer. Doppler broadening line shapes can be described by Gaussian line profile. When these broadening effects happen simultaneously, a Voigt profile needs to be introduced which is a combination of Gaussian line profile and Lorentzian line profile.

However, due to the dominance of instrument broadening in the measurement, a simplified line broadening was adopted in this work. The instrument line broadening factor is calculated in a way to match measured narrow Hg and Ar lines emitted by the wavelength calibration lamp as shown in Figure 2.3 and Figure 2.4. Three lines were picked from measurement of wavelength calibration and pixel values were examined. The average of ratios from three selected lines is the calculated instrument line broadening factor.

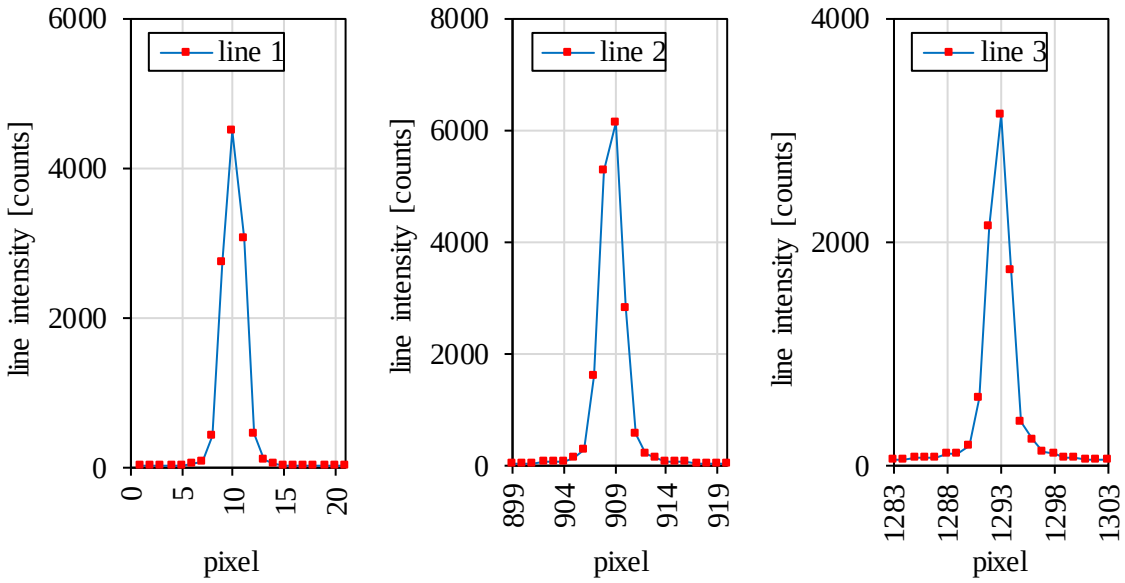

Figure 2.3 Line selection for determining instrument line broadening.

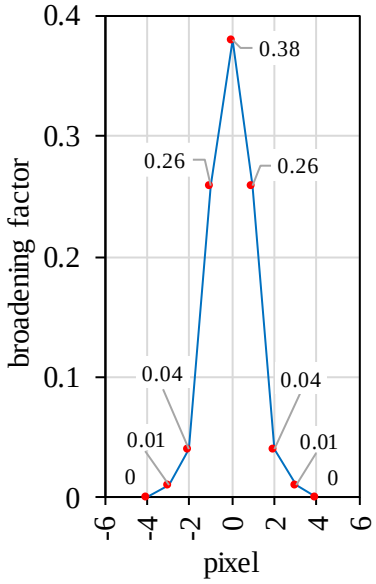

Figure 2.4 Calculated instrument line broadening factor.

2.4 HITRAN Simulation

2.4.1 Introduction

HITRAN which is the abbreviation for high-resolution transmission molecular absorption database is a compilation of spectroscopic parameters that can predict and simulate the emission and transmission of light [79]. The database compilation is available on the HITRAN web site [79]. It has been widely used by many researchers in different applications [80] such as terrestrial and planetary atmospheric remote sensing, and fundamental laboratory spectroscopic studies.

In this dissertation, HITRAN database is used to predict the water emission and absorption from non-sooting methane-air diffusion flames. The calculation and application of the HITRAN database towards are described in the following.

2.4.2 Calculation of HITRAN database

The workflow chart for the calculation of HITRAN Database is illustrated in Figure 2.5. With user's choice of selected wavenumber range and isotopologues, the format of database downloaded from HITRAN online web site needs first to be converted in JavaHAWKS software package to have the output file as comma-separated values file which can be opened with a program that delimits the file based on comma separators, *e.g.* Microsoft Excel [79]. The partition functions at different temperatures for selected molecules are also available from HITRAN online web site [79].

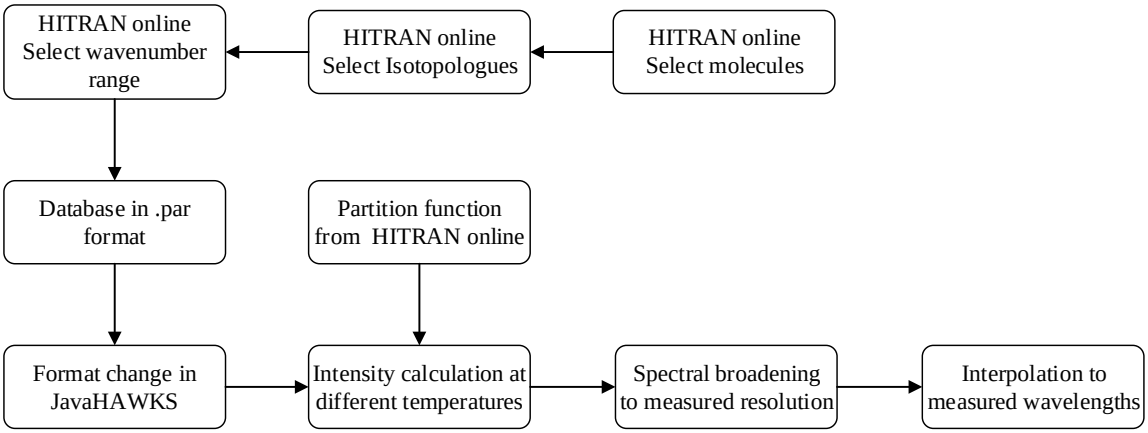

Figure 2.5 HITRAN simulation workflow.

The spectral line intensity in database defined for a single molecule, per unit volume with the transition between two ro-vibronic states is given as:

$$S_{ij}(T) = I_a \frac{A_{ij}}{8\pi c \nu_{ij}^2} \frac{\left(\exp\left(\frac{c_2 \nu_{ij}}{T}\right) - 1\right)}{\exp\left(\frac{c_2 \nu_{ij}}{T}\right)} \frac{g' \exp\left(\frac{-c_2 E''}{T}\right)}{Q(T)} \qquad (2.29)$$

where I_a is the isotopic abundance, A_{ij} is the Einstein coefficient for spontaneous emission [s^{-1}], the speed of light 2.998 x 10^8 [m/s], g' is the upper state statistical weight, T is the gas temperature [K], $Q(T)$ is the total internal function at temperature T which is tabulated on HITRAN website, c_2 is the second radiation constant [cm.K], E'' is the lower state energy [cm^{-1}], and ν_{ij} is the transition wavenumber [cm^{-1}].

The spectral line intensity at different temperature T can be calculated from the one at reference temperature which is given as T_{ref} of 296 K in HITRAN database by the following equation [79]:

$$S_{ij}(T) = S_{ij}(T_{\text{ref}}) \frac{Q(T_{\text{ref}})}{Q(T)} \frac{\exp\left(\frac{-c_2 E''}{T}\right)}{\exp\left(\frac{-c_2 E''}{T_{\text{ref}}}\right)} \frac{1-\exp\left(\frac{-c_2 \nu_{ij}}{T}\right)}{1-\exp\left(\frac{-c_2 \nu_{ij}}{T_{\text{ref}}}\right)} \tag{2.30}$$

where $S_{ij}(T_{\text{ref}})$ is the spectral line intensity [$\text{cm}^{-1}/(\text{molecule.cm}^{-2})$] at reference temperature T_{ref} of 296 K, $Q(T_{\text{ref}})$ is the total internal function at reference temperature, $Q(T)$ is the total internal function at temperature T which is tabulated on HITRAN website, c_2 is the second radiation constant [cm.K], T_{ref} is the reference temperature 296 K, T is the gas temperature [K], E'' is the lower state energy [cm^{-1}], and ν_{ij} is the transition wavenumber [cm^{-1}].

The Loschmidts number N_{L} at a given temperature T can be calculated by:

$$N_{\text{L}}(T) = N_{\text{L}}(T_{\text{ref}}) \frac{T_{\text{ref}}}{T} \qquad \left[\frac{\text{molecule}}{\text{m}^3.\text{atm}}\right] \tag{2.31}$$

where $N_{\text{L}}(T_{\text{ref}})$ is the Loschmidts number, 2.479 x 10^{25} [$\text{molecule.m}^{-3}.\text{atm}^{-1}$] at the reference temperature 296 K.

Since transition wavenumber instead of wavelength is given in HITRAN database, equation (2.3) is used to calculate the blackbody emissive intensity B_ν [$\text{W}/(\text{m}^2.\text{sr}.\text{m}^{-1})$]. Finally, the simulated volumetric line intensity [$\text{W}/(\text{m}^3.\text{sr})$] is calculated as:

$$e_{ij} = B_\nu(T) \cdot S_{ij}(T) \cdot N_{\text{L}}(T) \qquad \left[\frac{\text{W}}{\text{m}^3.\text{sr}}\right] \tag{2.32}$$

The Lorentzian half width at half maximum (HWHM), $\gamma_\nu(p,T)$ for a gas at pressure p [atm], temperature T [k] and partial pressure p_{self} [atm]:

$$\gamma_\nu(p,T)=\left(\frac{T_{\text{ref}}}{T}\right)^{n_{\text{air}}}\left(\gamma_{\text{air}}(p_{\text{ref}},T_{\text{ref}})\cdot(p-p_{\text{ref}})+\gamma_{\text{sefl}}(p_{\text{ref}},T_{\text{ref}})\cdot p_{\text{ref}}\right) \quad [\text{cm}^{-1}] \tag{2.33}$$

where γ_{air} is the air-broadened HWHM [cm^{-1}/atm] at T_{ref} = 296 K and p_{ref} =1 atm, γ_{self} is the air-broadened HWHM [cm^{-1}/atm] at T_{ref} = 296 K and p_{ref} =1 atm, and the n_{air} is the coefficient of the temperature dependence of the air-broadened half width. These values are tabulated in HITRAN base. In this study which is under normal atmosphere pressure, pressure broadening of spectral lines dominates and the Lorentz profile is calculate as:

$$f_L(\nu,\nu_{ij},p,T)=\frac{1}{\pi}\frac{\gamma_\nu(p,T)}{\gamma_\nu(p,T)^2+(\nu-\nu_{ij})^2} \quad [\text{cm}] \tag{2.34}$$

2.5 Uncertainty Analysis

Uncertainty analysis (error analysis) is a method to assess the uncertainty of a result because all measurements have some degree of uncertainty [81]. The errors are normally divided into precision errors (how accurately a result can be determined) and accuracy errors (how close a measured can be situating to a "true" value). Systematic errors in experimental observations typically result from the instruments used, whereas random errors result from unknown and unpredictable changes in the experiment. Errors in a measurement can not be avoided and they should be evaluated and estimated. The propagation of errors of the derived quantity needs to be addressed by the experimental uncertainty analysis and can be described by linearized approximation with total differentials [82]:

$$dz=\frac{\partial z}{\partial x_1}dx_1+\frac{\partial z}{\partial x_2}dx_2+\cdots=\sum_{i=1}^{n}\frac{\partial z}{\partial x_i}dx_i \tag{2.35}$$

where z is the function of several (n) variables. In general, the result of any measurement of a quantity z is reported as

$$\text{measured value of } z = z_{\text{best}} \pm dz \tag{2.36}$$

where z_{best} is the best quantity estimate, and dz is the uncentainty. Conventionally, dz is defined to be a positive value, thus $z_{best} + dz$ is the largest possible value of the measured quantity and $z_{best} - dz$ is the smallest [82].

However, in this work, the uncertainty errors can not be derived from this mathematical point of view since the temperature determininaton is mainly based on spectra fitting. In addition, errors may also result from various sources. The instrument used in the tests could cause a random uncertainty which can be reduced through a number of repeated measurements. For instance, multiple spectra could be taken for the same test case to minimize the possible flickering of the flame to account for the errors of spatial information resulting from the long exposure time. The accuracy of the simulated spectral data base could be improved by selecting finer temperature steps. Systematic errors in form of background emission are consistently observed in the same manner and may be corrected in the post-data analysis. Calibration errors are another type of the systematic uncertainty since factory calibration values may deviate from the actual values due to the lamp aging, in this work examined by comparison to blackbody source.

EXPERIMENTAL METHODS

3.1 Optical Technique

3.1.1 Spectrometer setup

The Andor Shamrock 500i spectrometer used in this study has a focal length of 500 mm as shown in Figure 3.1. Three interchangeable diffraction gratings, 80 l/mm, 300 l/mm and 1,200 l/mm offer wavelength resolutions of 0.5 nm, 0.13 nm and 0.02 nm respectively. The direct output is coupled with a Princeton Instruments eXcelon charged coupled device (CCD) camera (Pixis: 400), whereas the side output is coupled with an alignment laser which is necessary for the alignment of the imaging system consisting of a series of optical mirrors. The selection of the output port is achieved by turning a re-directing mirror inside the spectrometer. With a height of 8 mm and widths ranging from 10 μm to 2.5 mm, the side input slit is imaged on the CCD camera.

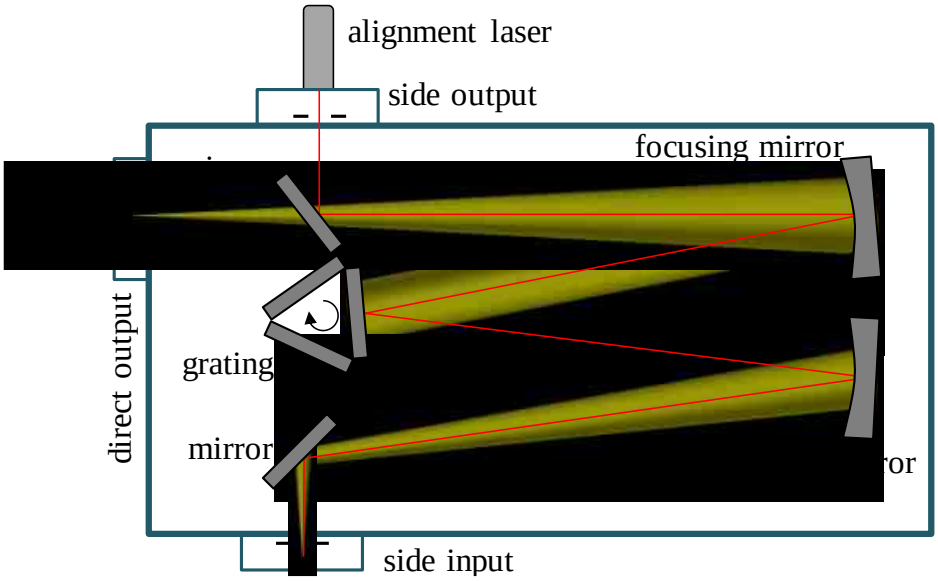

Figure 3.1 Configuration of Andor Shamrock 500i spectrometer system.

The diffraction grating is a dispersive optical component consisting of equally spaced parallel grooves with reflective coatings which can separate polychromatic light beam into light at different wavelength to form a spectrum [83]. The dispersion of the grating is based on grating equation:

$$m\lambda = d\left(\sin\theta_i + \sin\theta_r\right) \tag{3.1}$$

where m is the order of diffraction ($m = \pm 0, 1, 2, \ldots, k$), λ is the diffracted wavelength, d is the grating constant (*i.e.* blaze spacing), and θ_i and θ_d are the angles of incident light and diffracted light measured from the normal.

The size of measurement object imaged on the side input slit is determined by the external optical imaging system according to the lens equations [84]:

$$\frac{1}{\text{focal length}} = \frac{1}{\text{object distance}} + \frac{1}{\text{image distance}} \tag{3.2}$$

$$\frac{\text{image size}}{\text{object size}} = \frac{\text{image distance}}{\text{object distance}} \tag{3.3}$$

The Princeton Instruments CCD camera has a 1,340 x 400-pixel detector with a pixel size of 20 μm x 20 μm yielding a sensitive area of 26.8 mm x 8 mm and is used to acquire the VIS-NIR light to convert it to electrical signals. Figure 3.2 shows a typical image of extracted spectra and the axes of CCD. The vertical and horizontal pixels represent the spatial and wavelength domain respectively. The orange bar (enlarged for illustration purpose) represents the measurement region of the flame. It should be noted that the image was rotated by 90° through a periscope to measure the horizontal profile of flame. The wavelength resolution is determined by pixel width and also the given grating.

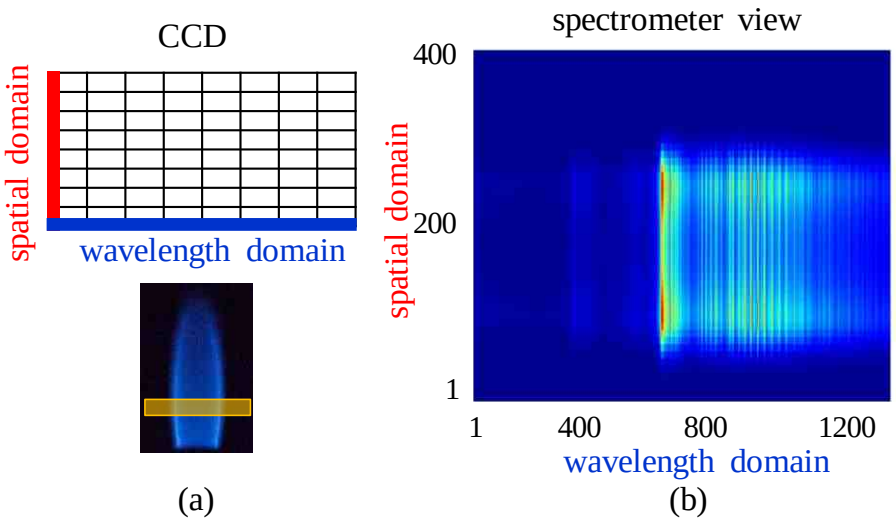

Figure 3.2 (a) Detailed view of the observed region above the nozzles, and (b) a typical image of extracted spectra.

For alignment purposes, the side input slit was opened to its maximum of 2.5 mm while the spectrometer was operated in 0^{th} diffraction order to produce a mere image of the observed region as shown in Figure 3.3. An image of scale was used to check the magnification based on optical imaging system and then to determine the actual size of measurement region.

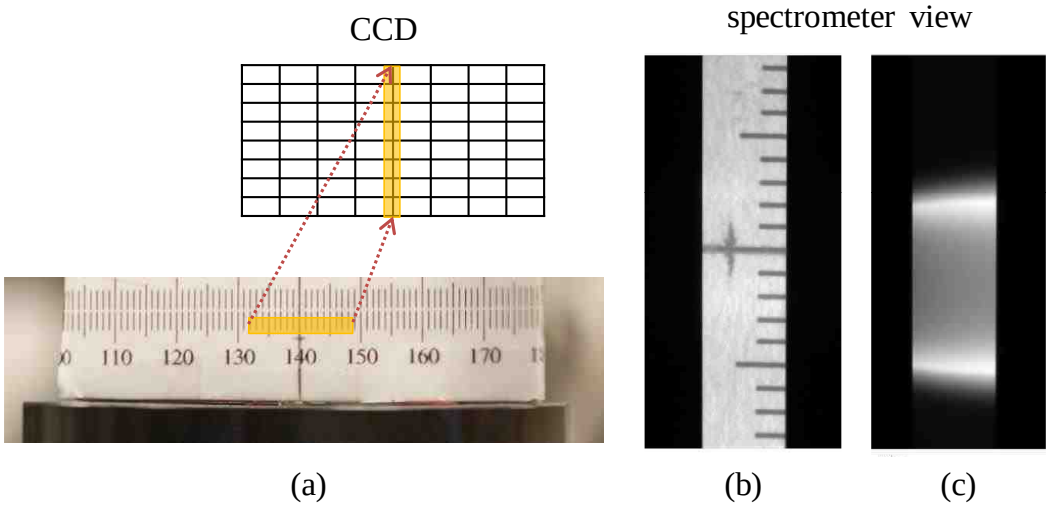

Figure 3.3 (a) Detailed view of the observed region, and (b) (c) views through the spectrometer in imaging mode to show the alignment procedure.

3.1.2 Wavelength calibration

As aforementioned, horizontal pixels of CCD camera represent the wavelength domain, however, the measured intensity information is stored in each pixel and the pixel number needs to be converted into wavelength for further spectra analysis. Also, since the pixel/wavelength correction of the spectrometer will drift slightly with working conditions and grating settings, the wavelength calibration needs to be conducted for every center wavelength and grating used. The following equation shows the relation between pixel number and wavelength [85].

$$\lambda_n = C_1 \cdot n^2 + C_2 \cdot n + C_3 \tag{3.4}$$

where is n is the pixel number, λ_n is the wavelength of pixel n, C_1, C_2 and C_3 are the constants of the binomial equation. For a CCD camera, typically at least three lines need to be identified to solve for the constants for binomial equations. A SL2 Mercury Argon Light Source from StellarNet Inc. is used to produce narrow emission lines at known wavelengths ranging from 253.65 to 1013.98 nm. In addition to three selected know lines, other known lines can be used to double-check the calibration.

The higher order spectra can overlap with zero order spectrum and cause confusion when the light is dispersed on a grating. The sorting filters should be used to block second and higher order spectra. This fact can be used to identify higher order mercury emission line for wavelength calibration. As shown in Figure 3.4, the grating and spectrometer settings for this calibration were with 80 l/mm grating and 750 nm center wavelength which should cover wavelength range approximately between 400 and 1050 nm. Thus, there were two sorting filters used: a common transparent plastic served to cut off lines under 300 nm, and a OG-550 filter had a cut-off position at 550 nm. The emission lines, 507.304 nm, 760.956 nm and 1014.608 nm only appeared when no filter was applied so that these line are the

second, third and fourth order lines of the strong mercury emission line at 253.65 nm respectively. After converting pixel number to wavelength, the calibrated spectrum may be checked with mercury/argon emission lines from NIST database [86].

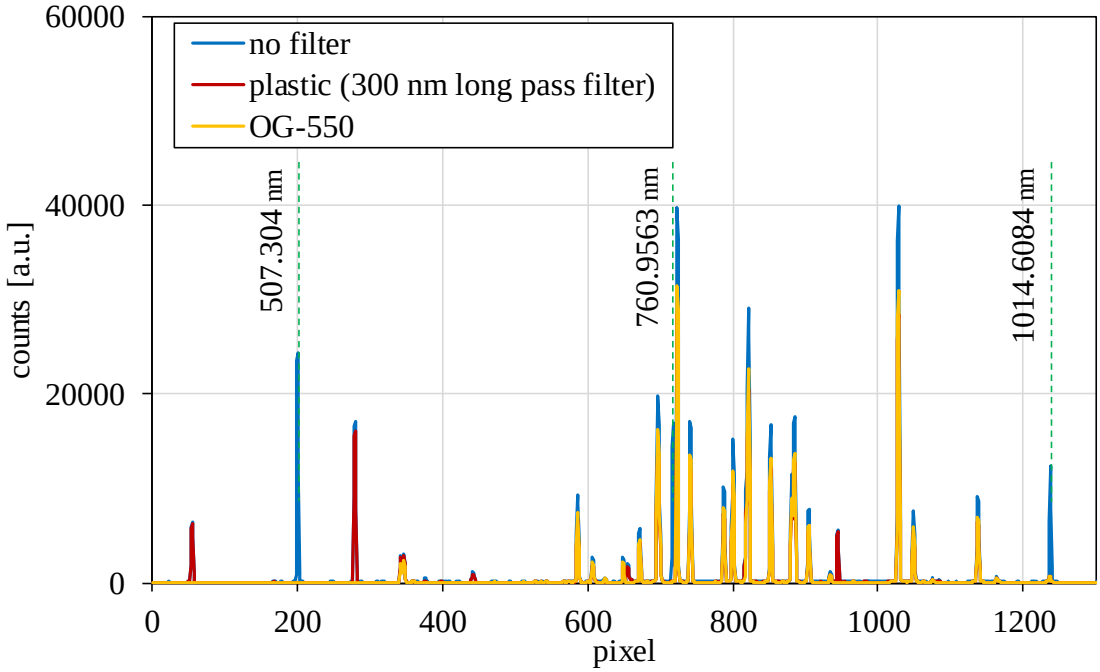

Figure 3.4 Example of a spectrum for wavelength calibration.

3.1.3 Intensity calibration

The measured intensity signals on each pixel are stored as 16-bit binary values (counts) which needs to be calibrated to spectral radiance in units of mW/(m².sr.nm). An integrating sphere light source (ISS-5P) from Gigahertz-Optik was used as the spectral radiance calibration standard which is capable of providing calibrated emission in the measurement range from 380 to 1,100 nm. It should be noted that the calibration lamp has to be placed at the location of measured flame and the lamp area must be larger than the measurement spot. If the lamp area is

small than the measurement spot, then the lamp needs to be moved and measured at different locations to cover the entire measurement area.

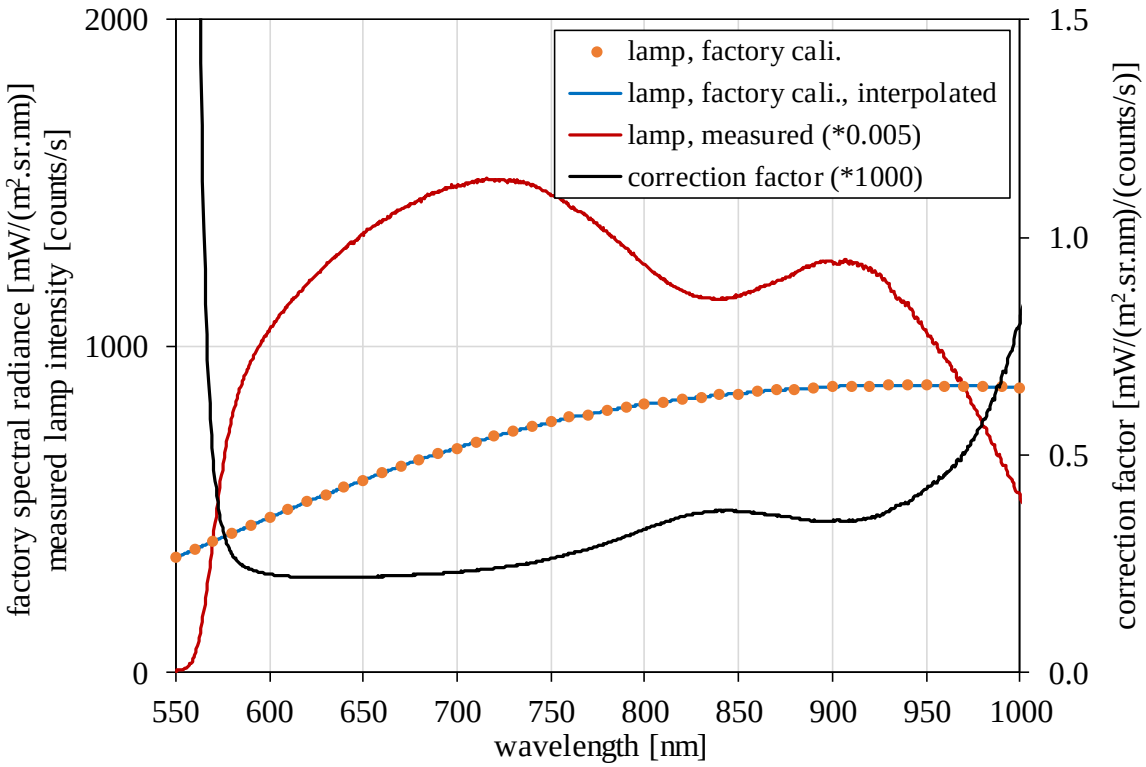

Figure 3.5 Example of intensity calibration.

Figure 3.5 shows example spectra used for intensity calibration. The orange dots are the factory calibration values of lamp which are then interpolated to values over measurement wavelength displayed as blue curve. The correction factor (black curve) is defined as the ratio of factory calibration value (blue curve) to measured values of the calibration lamp (red curve):

$$\mathrm{corr}_{\lambda} = \frac{I_{\lambda,\mathrm{lamp,factory}}}{I_{\lambda,\mathrm{lamp,measured}}} \tag{3.5}$$

The correction factor is inversely sensitive to the measured spectrometer response.

Before applying the correction factor, the measured flame emission data needs to be corrected for background and acquisition time:

$$I_{\lambda,\text{flame,BG Time calibrated}} = \frac{I_{\lambda,\text{flame,measured}} - I_{\lambda,\text{BG,measured}}}{t_{\text{acquisition}}} \tag{3.6}$$

where $I_{\lambda,\text{flame,measured}}$ is the measured flame intensity in counts, $I_{\lambda,\text{BG,measured}}$ is the measured background intensity in counts with the same acquisition time as $I_{\lambda,\text{flame,measured}}$, and $t_{\text{acquisition}}$ is the measurement acquisition time in second. Subsequently, the calibrated measurement spectral radiance is calculated with following equation [85]:

$$I_{\lambda,\text{flame,calibrated}} = I_{\lambda,\text{flame,BG Time calibrated}} \cdot \text{corr}_{\lambda} \tag{3.7}$$

The vertical pixel rows may need to be binned which is a summation process during the Analog-Digital conversion in the electronics (hardware binning) to increase sensitivity (signal-to-noise ratio) if the measured emission is too weak. For instance, by binning a successive 10 rows, a total of 40 strips (400 pixels/10 pixels/strip) will be saved by CCD control software, and the measured intensities will be higher by a factor of 10 for the same integration time. However, this binning process will decrease the spatial resolution by a factor of 10. The compromise between signal-to-noise ratio and spatial resolution is determined by the measurement spot size, for instance, the desired flame sheet thickness to be resolved.

In case that factory calibration values deviate from actual values due to the possible aging of calibration lamp, the factory calibration values were further examined by an ambient air joule heating blackbody source setup as shown in Figure 3.6 which was similar to the one used in [87]. The Magna-Power XR16-250/208 power supply is capable of generating 4000 W power with a maximum current of 250 A. Three type K Inconel sheath mineral insulated thermocouples connected to a NI-cDAQ -

9178 unit with an NI 9213 16 channel thermocouple module were used for temperature measurement which were controlled by LabView 2011. Two cavities served as blackbodies. Through interpolation of the temperatures obtained from adjacent thermal couples, the temperature of each blackbody can be determined. Figure 3.7 shows the calibrated lamp intensity values in comparison to the factory calibration values. The large difference in lower wavelength region is due to OG550 filter used and the large difference in upper wavelength region is due to fact that the CCD sensor becomes not sensitive in that region. However, these two curves overlap well from 600 to 900 nm wavelength region, indicating that the lamp factory calibration values are still reliable.

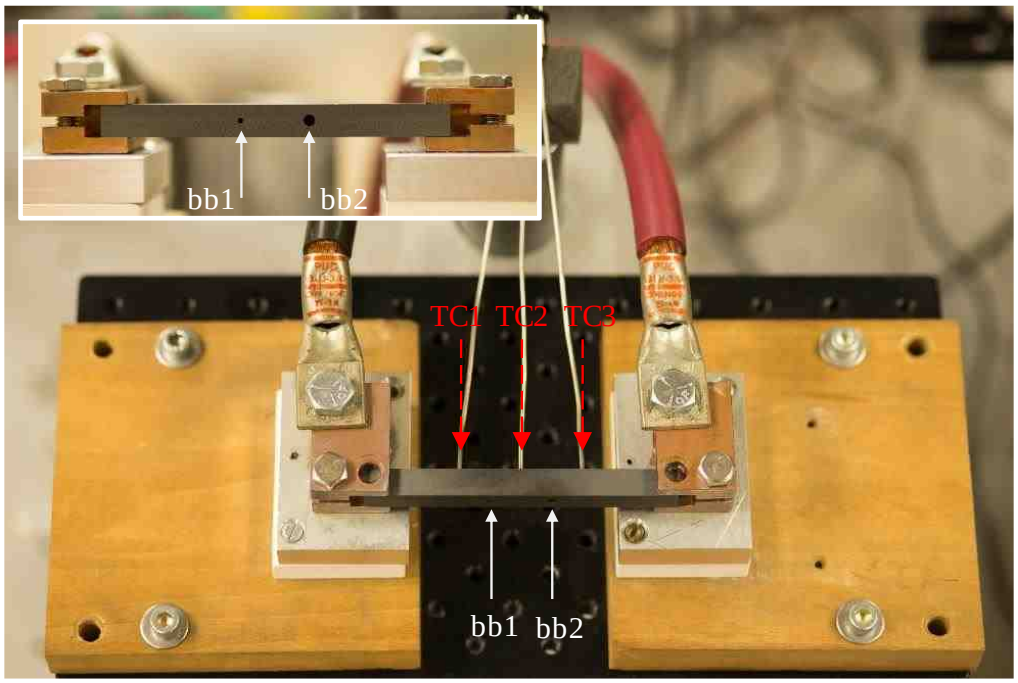

Figure 3.6 Ambient air joule heating blackbody source setup.

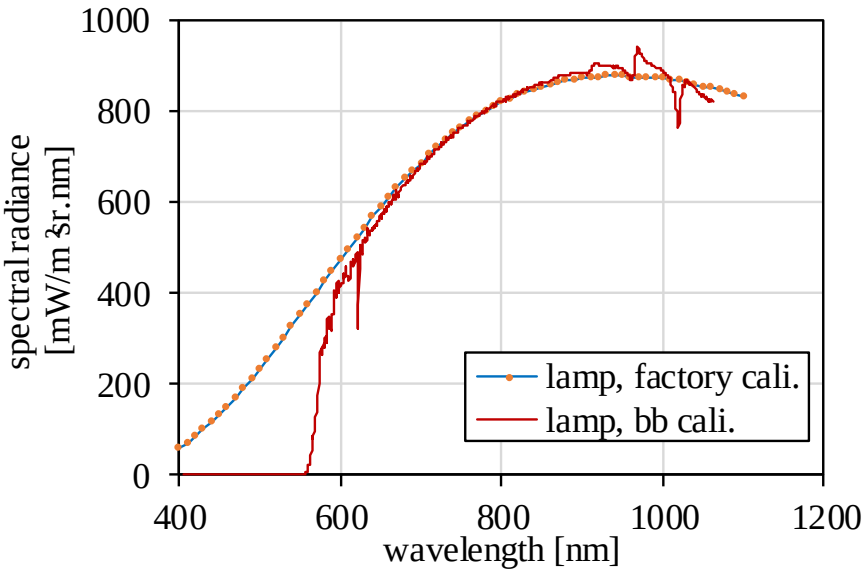

Figure 3.7 Calibrated lamp intensity values using a blackbody light source in comparison to the factory calibration values.

3.2 Data Processing

3.2.1 Angle tilting correction procedure

Due to an internal mis-alignment in the spectrometer, the spatial coordinates of measured spectra were titled as shown in Figure 3.8. For measurement at location of row y_o, in Figure 3.8(top figure), two ends of one spectrum shifted to different spatial rows in Figure 3.8(middle figure). The mis-placed spectral signals need to be corrected for accurate spectroscopy analysis in Figure 3.8(bottom figure).

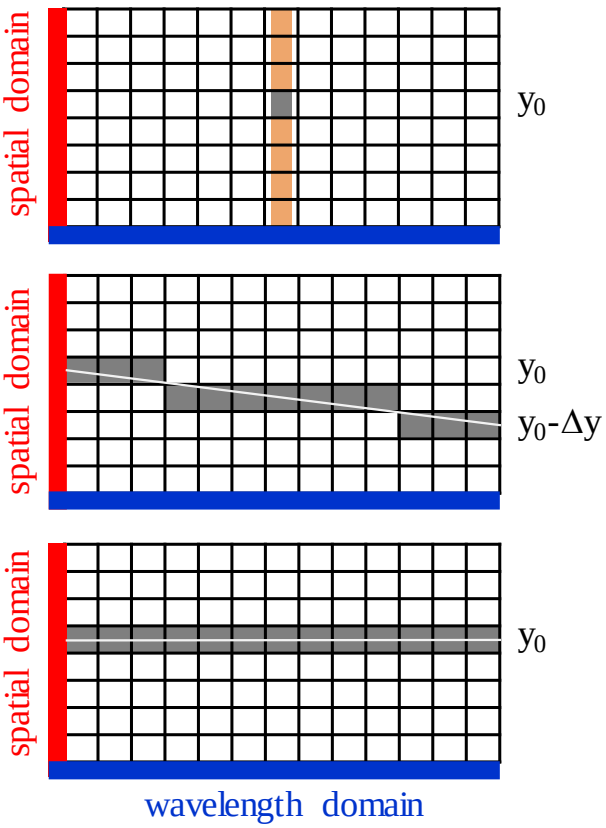

Figure 3.8 Illustration of spectral deformation and tilting correction procedure.

An angle tilting correction algorithm was developed to correct the spectra. The 40 strips values were first interpolated back to values over 400 rows/strips. As shown in Figure 3.9(b) and (c), by lifting one side on the image while maintaining the other side, 18 more strips were added the spectra image with the white regions being artifacts with "not-a-number" values. After cutting off 9 rows from both top and bottom region, 400 effective strips were created from the truncation of 418 tilting correction strips. Last, a successive 10 strips were binned to recover 40 strips as the same dimension of the measured data to maintain the actual spatial resolution as shown in Figure 3.9(d).

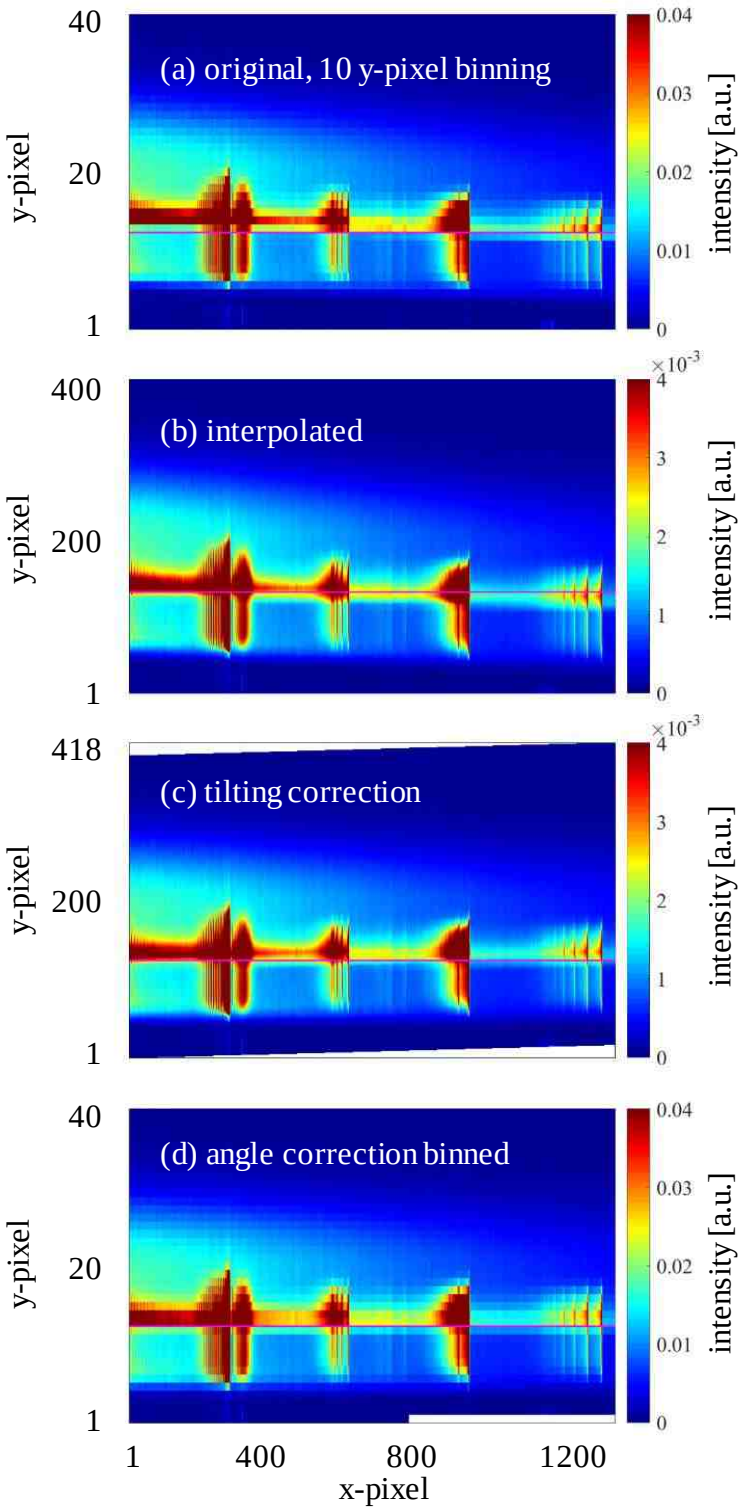

Figure 3.9 Example spectra of angle correction procedure.

3.2.2 Reconstruction of local intensity

Emission spectroscopy integrates signals along the line of sight so that only integrated values are obtained without spatial information in the direction along the line of sight. To reconstruct local intensity, an Abel inversion needs to be applied to the measured integrated values [88]. The relation between the measured integrated intensity along the line of sight $I(z)$ and the local intensity $\varepsilon(r)$ is described by Abel's equation [89]:

$$I(z) = 2\int_{r=z}^{R} \frac{r}{\sqrt{r^2 - z^2}} \varepsilon(r)\, dr \tag{3.8}$$

$$\varepsilon(r) = -\frac{1}{\pi}\int_{z=r}^{\infty} \frac{(dI/dz)}{\sqrt{r^2 - z^2}}\, dz \tag{3.9}$$

where R is the outer radius of the calculating regime, z is the off-set distance, and r is the local profile radius as shown in Figure 3.10. Since the view angle of the spectrometer is very small, the simplified geometry is used in this dissertation. This method is also referred to as Onion-Peeling [90].

As illustrated in Figure 3.10, by assuming rotational symmetry profile and optically thin medium, an example radiating volume with four profiles can be calculated by the following equations:

$$\begin{aligned}
I_{3,\text{int}}(z_3) &= \varepsilon(r_3)\cdot L_3(r_3) \\
I_{2,\text{int}}(z_2) &= \varepsilon(r_3)\cdot L_2(r_3) + \varepsilon(r_2)\cdot L_2(r_2) \\
I_{1,\text{int}}(z_1) &= \varepsilon(r_3)\cdot L_1(r_3) + \varepsilon(r_2)\cdot L_1(r_2) + \varepsilon(r_1)\cdot L_1(r_1) \\
I_{0,\text{int}}(z_0) &= \varepsilon(r_3)\cdot L_0(r_3) + \varepsilon(r_2)\cdot L_0(r_2) + \varepsilon(r_1)\cdot L_0(r_1) + \varepsilon(r_0)\cdot L_0(r_0)
\end{aligned} \tag{3.10}$$

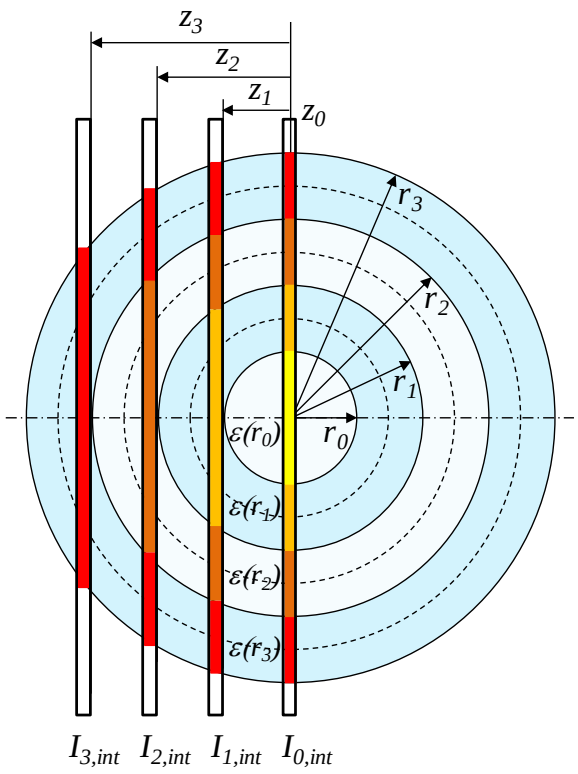

Figure 3.10 Illustration of the geometry for four lines of sight in a rotational symmetrical radiation field recreated from [91].

A constant spatial radial emission creates an elliptic integrated profile. Therefore, the applied Abel inversion can be checked by whether a elliptic profile can be obtained as shown in Figure 3.11. For a large sets of off-set profiles, to avoid cumbersome recursive calculation for solving $L_n(r_n)$ from the outer ring profile (first equation in (3.10)) to the inner ring profile (last equation in (3.10)), a matrix inversion is applied to calculate local intensity (r_n):

$$\begin{bmatrix} L_n(r_n) & \cdots & 0 \\ \vdots & \ddots & \vdots \\ L_n(r_n) & \cdots & L_o(r_o) \end{bmatrix} \cdot \begin{bmatrix} \varepsilon(r_n) \\ \vdots \\ \varepsilon(r_o) \end{bmatrix} = \begin{bmatrix} I_{n,\mathrm{int}}(z_n) \\ \vdots \\ I_{o,\mathrm{int}}(z_o) \end{bmatrix} \tag{3.11}$$

$$\begin{bmatrix} \varepsilon(r_n) \\ \vdots \\ \varepsilon(r_o) \end{bmatrix} = \begin{bmatrix} L_n(r_n) & \cdots & o \\ \vdots & \ddots & \vdots \\ L_n(r_n) & \cdots & L_o(r_o) \end{bmatrix}^{-1} \cdot \begin{bmatrix} I_{n,\mathrm{int}}(z_n) \\ \vdots \\ I_{o,\mathrm{int}}(z_o) \end{bmatrix} \tag{3.12}$$

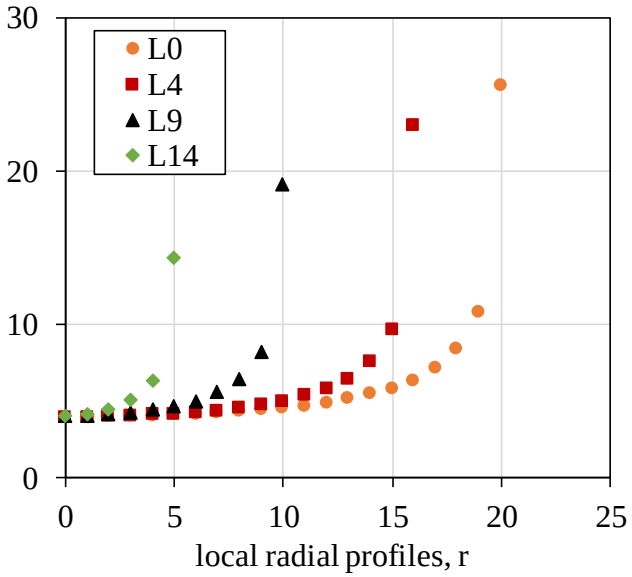

Figure 3.11 Check profiles.

3.2.3 *Extraction of DSLR RAW images in MATLAB*

A number of consumer Digital single-lens reflex cameras have been shown to be a low cost and powerful tool as an optical detector due to the improved resolution, sensitivity and dynamic range features [28, 92-95]. Kuhn et al. used an open-source imaging process software OMA [96] to capture, store and decode Nikon D70 and D90 raw data ("NEF" format). Giassi et al. spectrally characterized the Nikon D300s camera to acquire a nitrogen-diluted laminar diffusion methane-air co-flow flame images filtered by the blue channel which is considered representative of the CH^* emission of the $A^2\Delta$-$X^2\Pi$ transition centered around 431 nm [28]. Guo et al. used a Nikon D700 camera to measure soot temperature and soot volume [93].

The internal built-in image processing algorithm, which is good for "JPEG" format (typically an 8-bit image) export, might not truly reflect the light of scene. The "RAW" format data is a format that contains the unprocessed image with pixel values and meta-information [97]. It is obtained straight from the sensor without any compression or internal image processing/retouching. A simplified DLSR RAW image processing procedure in MATLAB based on Sumner [97] and Eddins [98] is shown in Figure 3.12. A detailed step-by-step code is discussed in [97] to read the DNG format image into MATLAB array.

Figure 3.12 Workflow for extraction of DSLR RAW images.

The Nikon camera raw "NEF" format is a proprietary format and needs to be converted to the open DNG (Digital Negative) format image using Adobe DNG Converter [99]. It should be noted that Adobe DNG Converter needs to be configured in a way that the "Uncompressed" box is checked and "Linear demosaiced" box is unchecked before converting to DNG format. However, the intermediate steps Linearization or White balance correction proposed by Sumner [97] should be skipped in this study because we don't want to include the linearization and white balance correction due to the pre-setting of white balance values in camera. After de-mosiacing, the MATLAB array containing 3-layer RGB image information can be further analyzed benefitted from 14-bit lossless raw data file (Nikon D610).

CHEMILUMINESCENCE MEASUREMENT IN CO-FLOW FLAME

4.1 Experimental Setup

4.1.1 Co-flow burner and filtered image measurement setup

Figure 4.1 shows the schematic of the "Yale" co-flow burner. The burner had a central fuel nozzle (4 mm in diameter) surrounded by a co-flow air (74 mm in diameter). The fuel composed of 30% research grade methane diluted with 70% nitrogen by volume was controlled by a mass flow controller. The gas exit speed was set to be 35 cm/s which is a suggested testing parameter from [100]. A Nikon full frame DSLR camera D610 coupled with a Nikkor 105 mm f/2.8 macro lens was used to capture visible flame images. With a 35.9 x 24.0 mm CMOS sensor (Nikon FX format) of 6014 x 4016 pixels, the Nikon D610 was able to store 14-bit lossless raw data file ("NEF" format). An interference filter (430 nm center wavelength, 10 nm FWHM) from the Ealing Corporation was placed right in front of camera lens to isolate and collect CH^* peak chemiluminescence. The 430 nm filter was characterized with the spectrometer and the calibration lamp. and the transmissivity and FWHM are as shown in Figure 4.2.

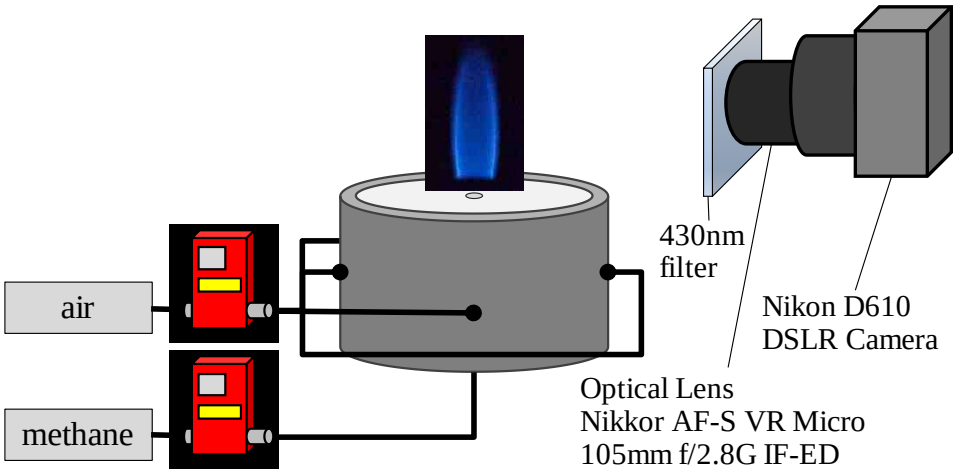

Figure 4.1 Schematic of the "Yale" co-flow burner.

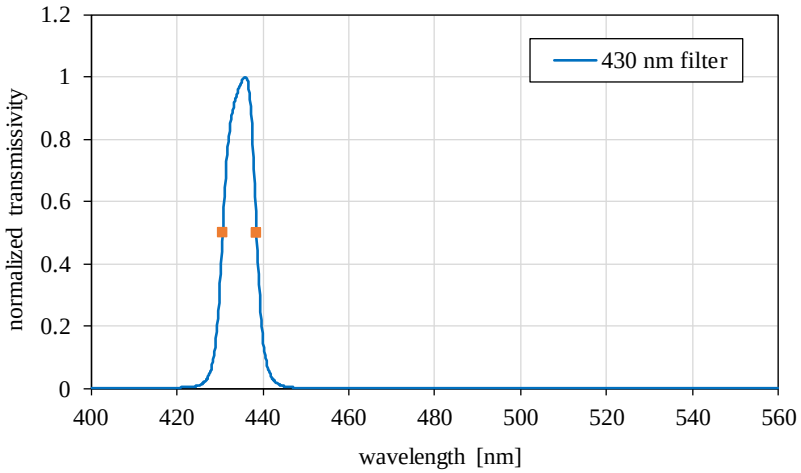

Figure 4.2 The normalized (to its maximum) spectral transmissivity of a narrow band 430 nm interference filter.

The ISO, F-stop and metering mode were set to ISO-100, f/8 and Pattern. Since the optimum camera shutter speed was not known, a series of flame and calibration lamp images were taken with varying shutter speed. There are three basic components (the mirror box, the bottom door, and the top door) in the DSLR camera controlling the shutter release system. When one looks through a DSLR camera optical viewfinder, essentially the object is seen through a series of mirrors which direct lights collected from the lens. When the shutter button is released, mirrors flip upwards to allow light to pass, then the bottom door moves to bottom to expose the sensor behind it. After that the top door moves down from top to finish exposure by covering the entire sensor. The time of this process depends on shutter speed setting. As shown in Figure 4.3, for shutter speeds faster than 0.01 s, the peak intensities obtained from both flame and lamp seem to be a constant about 600 counts. This phenomenon may be attributed to this shutter mechanical system such that sometimes a shutter speed can be so fast that the sensor won't be properly exposed.

As shown in Figure 4.4, For the flame measurement, the measured intensity is linear with respect to shutter speed from 0.4 to 2 s. For the lamp measurement, the

measured intensity is linear with respect to shutter speed from 0.04 to 0.45 s and the lamp intensity is very strong so that the CMOS is saturated at the shutter speed of 0.5 s. Thus, the useful shutter speeds for emission measurement with DSLR camera are the result of the combined effect of the emission intensity of object and DSLR camera mechanical shutter speed setting. In this following analysis, the shutter speed of 2 s was used for flame measurement analysis.

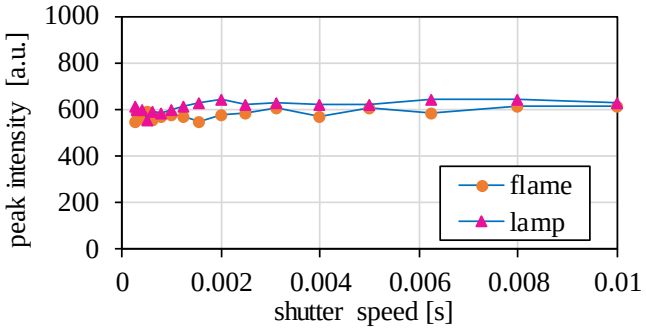

Figure 4.3 Correlation between the measured peak intensity and DSLR camera shutter speed for shutter speed faster than 0.1 s.

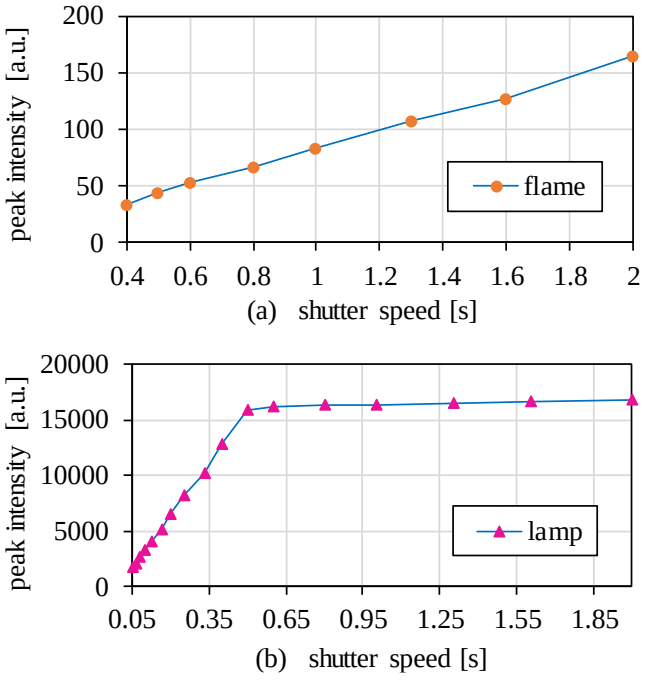

Figure 4.4 Correlation between the measured peak intensity of (a) flame, (b) lamp and DSLR camera shutter speed.

4.1.2 Spectrometer setup

Through a 445 mm focal length parabolic mirror, the radial profile of co-flow flame was imaged onto the spectrometer side input slit, therefore providing a simultaneous detection of radial positions across the whole flame. With the chosen optical imaging system, a region of ~17 mm was imaged onto the CCD as shown in Figure 4.5. A periscope was used to rotate the measured region by 90° to image the radial profile. To increase the sensitivity while maintaining the spatial resolution, successive clusters of 8 rows in *y*-direction on the CCD were binned, yielding a total of 50 spectra per image, each one representing a spatial average over 0.34 mm horizontal width in the flame. A vertical (*z*) translation stage was used to move the burner platform and enabled measurements at different vertical locations within the co-flow flame. As illustrated in Figure 4.6, an image of the observed region was acquired to check alignment while the spectrometer was operated in 0th diffraction order with a maximum input slit size of 2.5 mm. The white line indicates the measurement region when the input slit is closed to 50 μm for spectrum measurement.

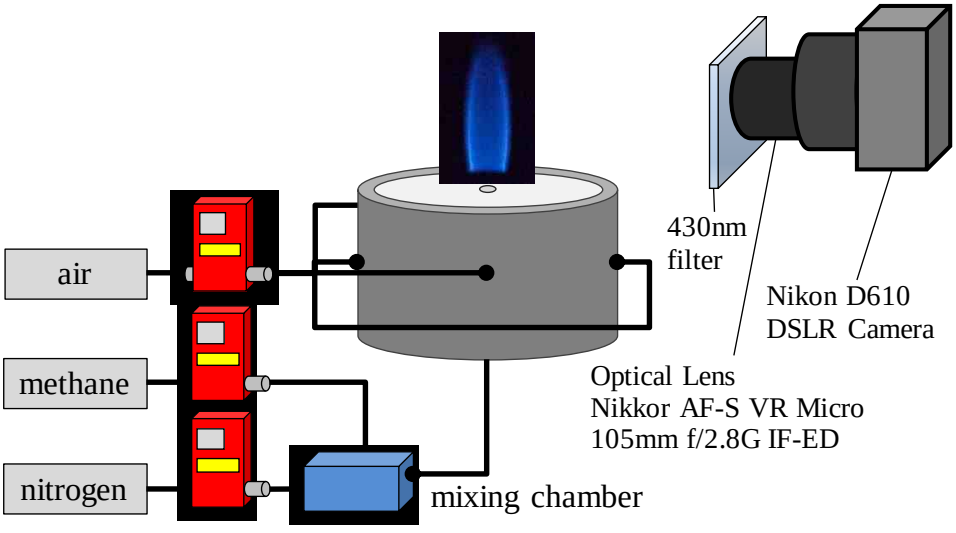

Figure 4.5 Schematic of the optical setup for spectroscopic measurement of the methane-air co-flow diffusion non-sooting flame.

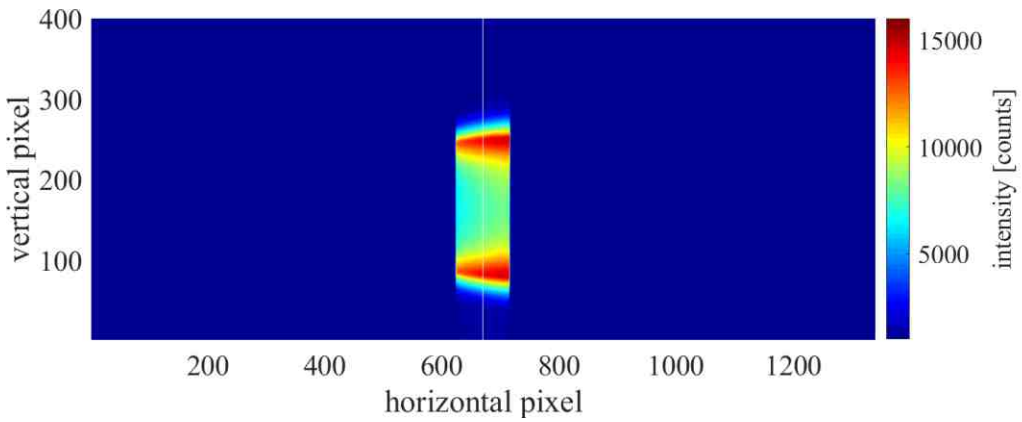

Figure 4.6 Example spectrometer view of co-flow methane-air diffusion flame with the input slit (measurement) center at z = 17 mm for alignment procedure.

4.2 Results and Discussion

4.2.1 Two-dimensional chemiluminescence and water emission

To observe the emission of the CH $A^2\Delta$-$X^2\Pi$ system for the Δv = 0 bands, C_2 $A^3\Pi$-$X^3\Pi$ system (Swan) for the Δv = +1, 0 and -1 bands and water emission with one of the strongest bands at 928 nm, the input slit was opened at 50 μm, and the spectrometer was set to the 300 lines/mm grating, yielding a useable wavelength range of 172.6 nm with a pixel resolution of 0.13 nm. To obtain sufficient spectral signals, for CH^* and C_2^* chemiluminescence measurements, the center was set to 480 nm with an acquisition time of 30 sec; for water emission measurements, the center was set to 935 nm with an acquisition time of 60 sec. Figure 4.7 and Figure 4.8 show examples of the measured spectra.

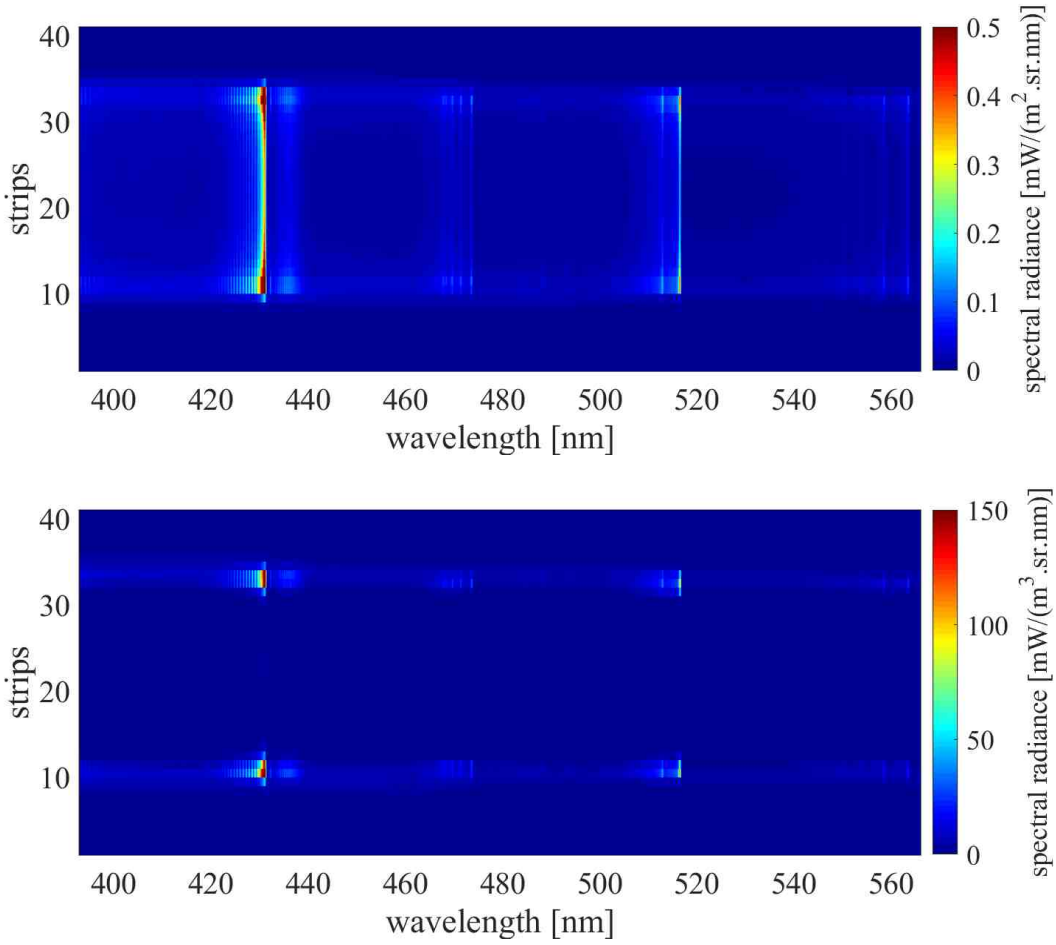

Figure 4.7 Example of emission spectra of CH^* and C_2^* obtained for co-flow methane-air diffusion flame with the slit (measurement) center at z = 17 mm: original (top), Abel inverted (bottom).

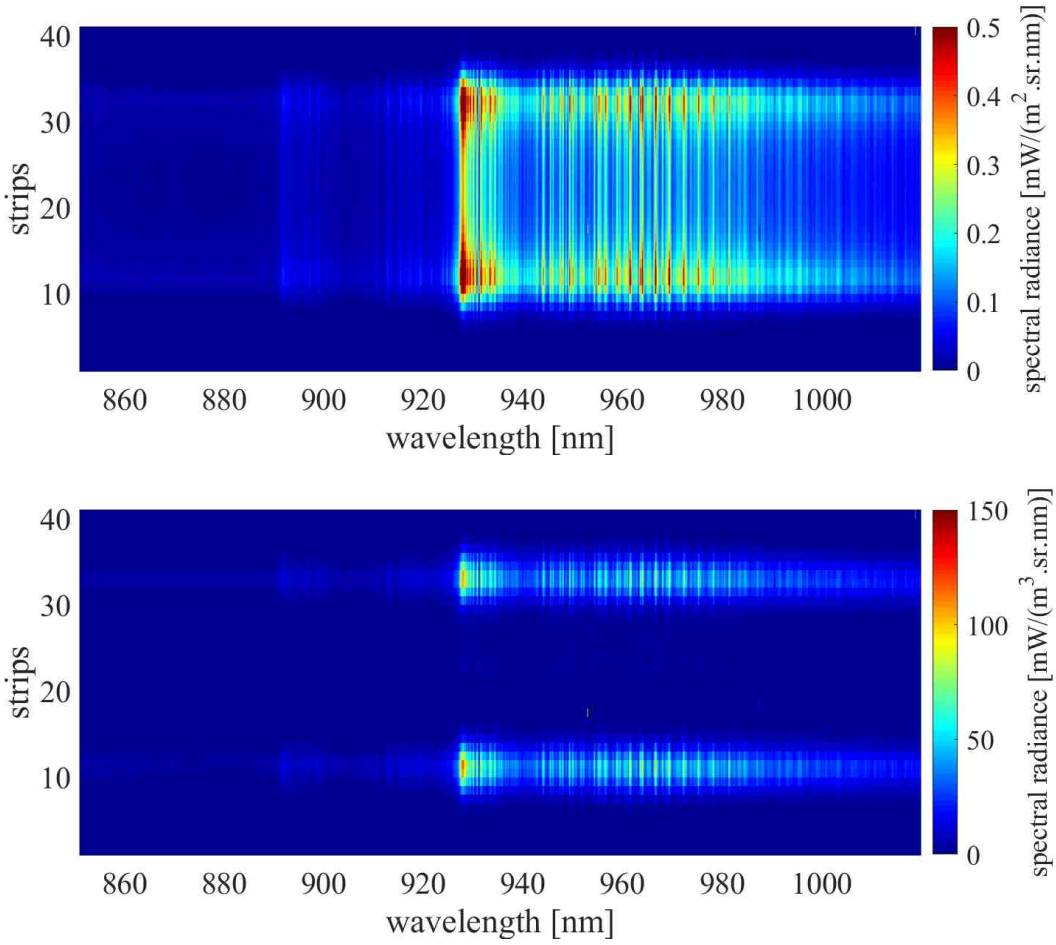

Figure 4.8 Example of emission spectra of H_2O obtained for co-flow methane-air diffusion flame with the slit (measurement) center at z = 17 mm: original (top), Abel inverted (bottom).

Due to the axisymmetric flame structure, it was possible to apply the Abel inversion to the line-of-sight chemiluminescence to obtain the two-dimensional intensity profiles from both filtered images acquired by DSLR camera and spectrally resolved spectrometer measurements where the intensity calibration was also performed. Figure 4.9 shows an example of the Abel inverted filtered CH^* image of a non-sooting co-flow methane-air diffusion flame compare with the original line of sight integrated image from DSLR camera filtered image measurement. The noise spots in center line are due to nature of Abel inversion resulting singularities. The

intensity values in counts were normalized to its own maximum. The thickness of flame sheet (CH^* emission region) is estimated to be of 0.25 mm.

From comparison between Figure 4.9 and Figure 4.10, reasonably good agreement is illustrated between flame shape from filtered CH^* images and flame shape from reconstructed images from light-of-sight measurement of spectrally resolved CH^* emission. The C_2^* emission shows the same origin of CH^* emission as shown in Figure 4.11. The signals of CH^* and C_2^* emission measurements become too weak at about z = 30 mm, while the signals of water emission decrease slower and become too weak at about z = 42 mm. Also, the water emission seems to have a larger thickness in the lower part of the flame (5 - 25 mm), and to accumulate as a volume at about 25 - 30 mm above the nozzle. This is due to water as one of the combustion product being diffused to inner part of the flame.

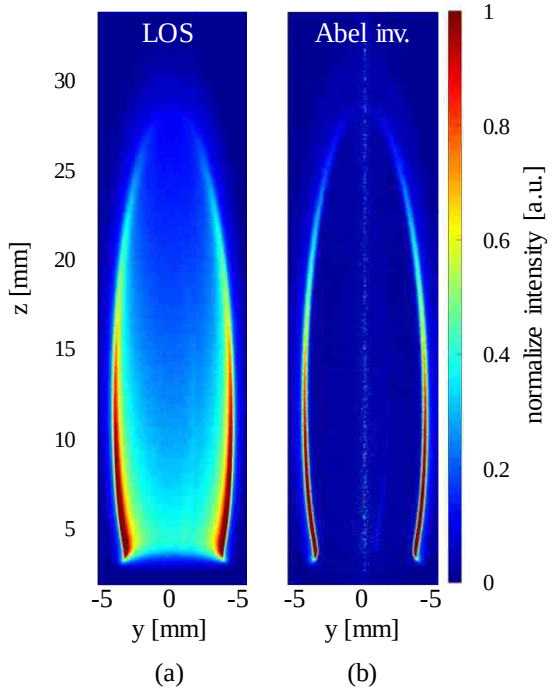

Figure 4.9 Filtered CH^* image measured by DSLR camera of a co-flow methane-air diffusion flame with values normalized to its maximum: (a) LOS image, and (b) Abel inverted image.

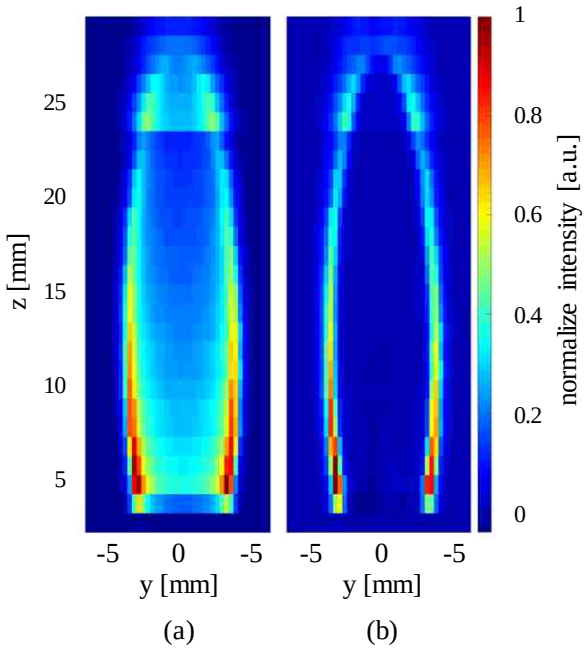

Figure 4.10 Reconstructed flame shape from light-of-sight measurement of spectrally resolved CH^* chemiluminescence: (a) original and (b) Abel inverted.

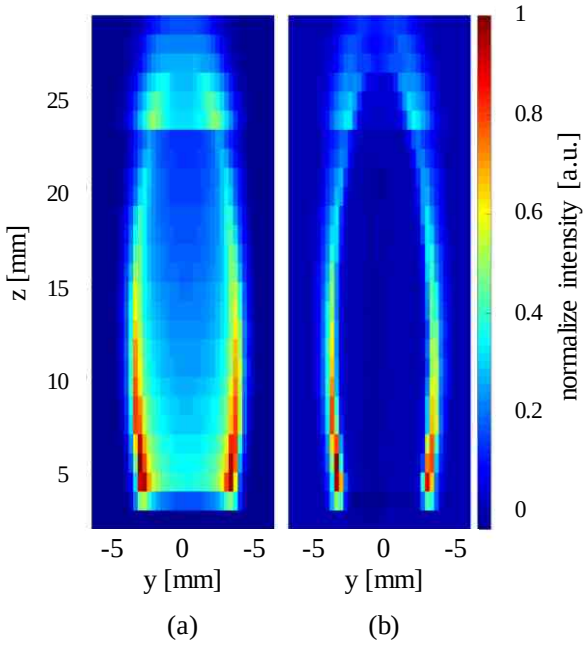

Figure 4.11 Reconstructed flame shape from light-of-sight measurement of spectrally resolved C_2^* chemiluminescence: (a) original and (b) Abel inverted.

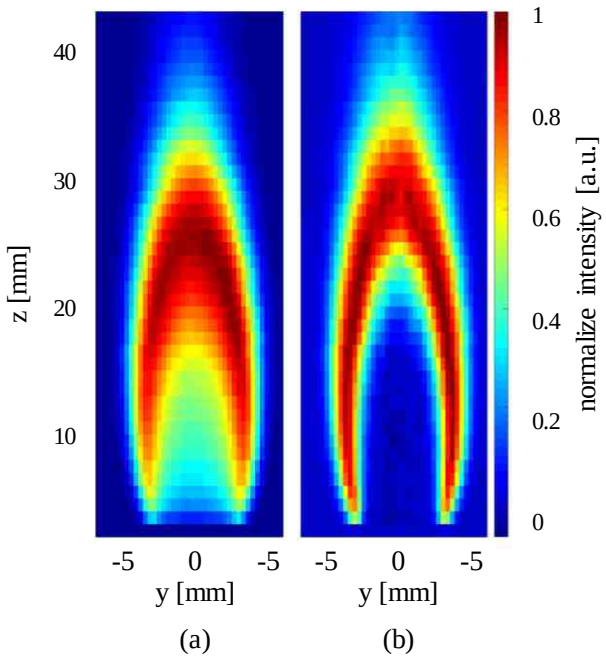

Figure 4.12 Reconstructed flame shape from light-of-sight measurement of spectrally resolved water emission: (a) original and (b) Abel inverted.

4.2.2 Determination of water emission from HITRAN simulation

To effectively compare measured spectra to simulation spectra, the above simulated line intensity needs to be broadened and interpolated to the measured wavelength range and resolution. For an emission line with original intensity e_o [W/(m^3.sr)], centered at ν_o [cm^{-1}] with Lorentzian HWHM, γ_ν [cm^{-1}] which is calculated from equation (2.33), the conversions to center wavelength λ_o [nm] and HWHM γ_λ [nm] are:

$$\lambda_o = \frac{1}{\nu_o} \times 10^7 \qquad [\text{nm}] \tag{4.1}$$

$$\gamma_\lambda = \frac{1}{2} \times \left(\frac{1}{\nu_o - \gamma_\nu} - \frac{1}{\nu_o + \gamma_\nu} \right) \times 10^7 \qquad [\text{nm}] \tag{4.2}$$

With a chosen spectral resolution λ_{res} and wavelength range $\Delta\lambda$, each line broadening is included for $\pm \Delta\lambda/2$ (*i.e.* $\Delta\lambda/\lambda_{res}$ wavelength intervals). The broadened wavelength λ_n for one line is calculated as:

$$\lambda_n = \lambda_o + \left(n - \frac{\Delta\lambda}{\lambda_{res}} \right) \cdot \lambda_{res} \qquad [\text{nm}] \tag{4.3}$$

The broadening is then normalized to the sum of all broadening factors (*i.e.* the sum over all considered broadening factors is 1 because of conservation of the line intensity), the broadened intensity is written as:

$$e_{broadened,\lambda} = \frac{f_L(\nu, \nu_{ij}, p, T)}{\sum f_L(\nu, \nu_{ij}, p, T)} \cdot e_o \qquad \left[\frac{\text{W}}{\text{m}^3.\text{sr}} \right] \tag{4.4}$$

where the broadening profile f_L is assumed to be described by Lorentzian profile given from equation (2.34). Attention has to be paid to conversion between wavelength [nm] and wavenumber [cm^{-1}] in calculation. An example of line broadening is illustrated in Figure 4.13. For the $\Delta\lambda$ = 1 nm used with a spectral resolution of 0.002 nm, each line broadening was included for ± 0.5 nm, and the total of 500 wavelength intervals were obtained.

For methane-air diffusion flames, the stoichiometry combustion is:

$$CH_4 + 2(O_2 + 3.76\,N_2) \rightarrow CO_2 + 2H_2O + 7.52\,N_2 \tag{4.5}$$

The maximum possible water content by volume is ~20%, thus, one assumption has to be made such that the actual number of water molecules is the Loschmidt's number multiplied by 20% for HITRAN calculation. However, this does not

necessarily represent a measurement of water concentrations since HITRAN assumes thermal excitation but water is created through a chemical reaction and might be created in already excited states.

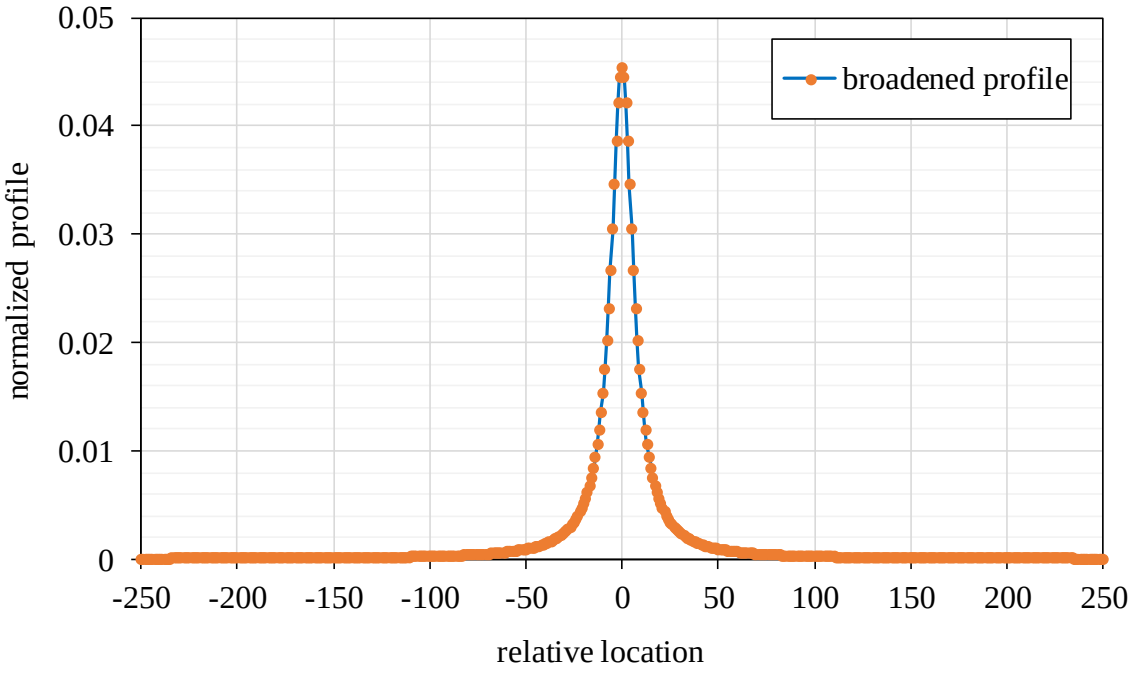

Figure 4.13 Example of line broadening profile.

The intensities of all broadened lines were summed up on the wavelength grid and the absorption coefficients were determined from these broadened intensities by dividing by the local Planck emission. By examining the Abel inverted water emission intensity profile as shown in Figure 4.12, the length of line of sight for simulation was assumed to be approximately 4 mm. The examples of spectra for 1500 K are shown in Figure 4.14. The effect of possible absorption in room temperature air was estimated by calculating absorption coefficients for a temperature of 300 K. The length of the line-of-sight for absorption in room air of 1.5 m was corrected by multiplying a factor of ~0.004 to make the simulated intensity with absorption comparable with the measured intensity. The results indicate that

neither self-absorption nor absorption in room temperature air seem to influence the spectral shape in a way which gets the simulation in better agreement with the measurement.

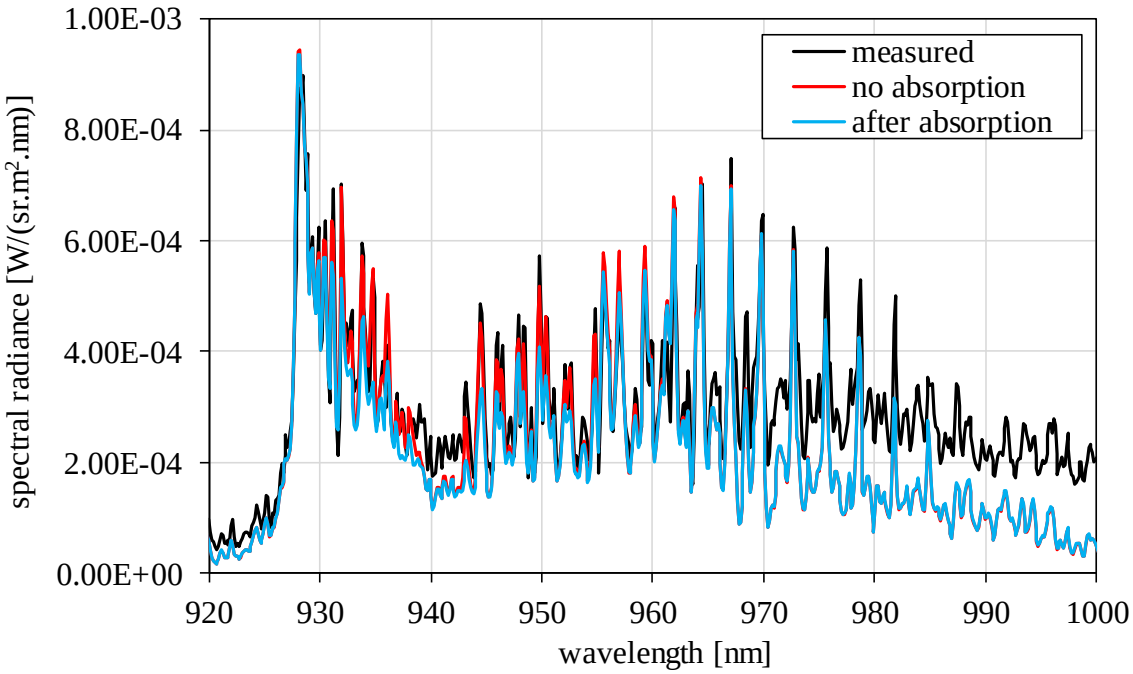

Figure 4.14 Example spectral radiance spectra for simulated water emission with absorption.

Therefore, to reduce HITRAN simulation calculation efforts, self-absorption was excluded in the following analysis. In this study the emission from CO_2 was also calculated with HITRAN CO_2 database and it was found that the CO_2 emission spectra in the NIR region were negligible compared to those of H_2O which was also pointed out by study from Nakaya et al [101].

Figure 4.15 shows an example spectra of the normalized measured intensity of the co-flow flame at z = 15 mm compared to simulated H_2O emission at selected temperatures to illustrate how the spectra shape (*i.e.* peak ratio features) is sensitive to temperature change. The intensity values were normalized to its peak at 928 nm.

Within this temperature range, spectral peak ratios seem only sensitive to temperature for wavelengths of 928 -980 nm. Also, the normalized measurement spectrum always has an offset to the simulation indicating an underlying emission was present (potentially continuum emission from soot or background) which is already visible around 940 nm and becomes dominant at wavelengths greater than 980 nm.

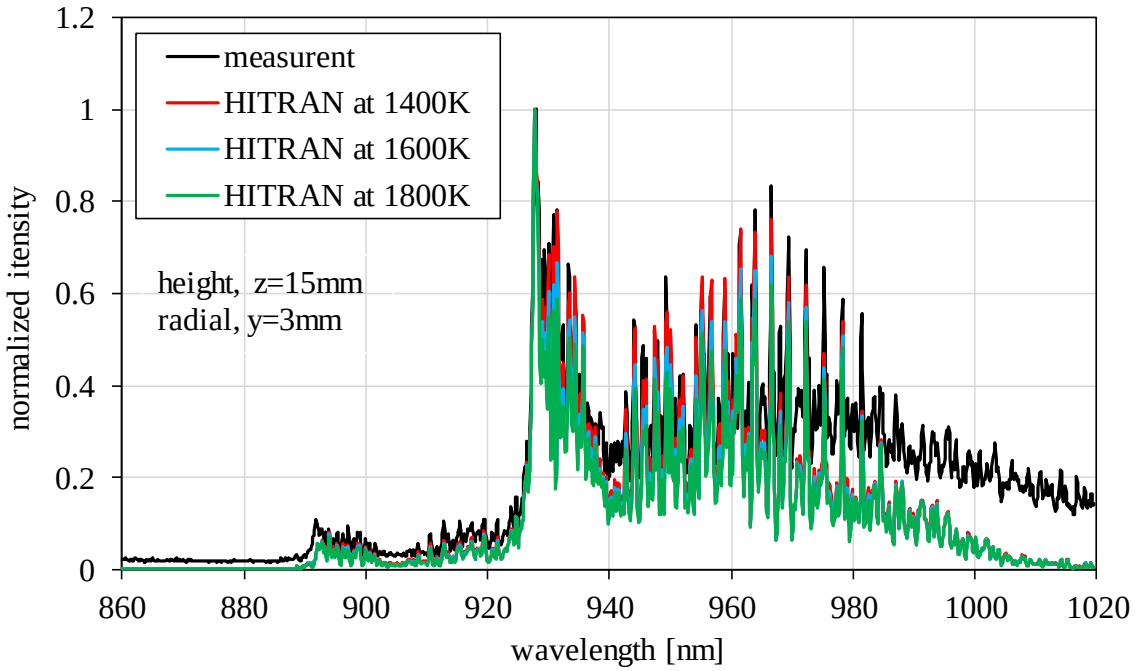

Figure 4.15 Normalized measured intensity of co-flow flame at z = 15 mm compared to simulated H_2O emission at selected temperatures.

An attempt to determining H_2O temperature for the co-flow flame at a height of 15 mm, radial location of 3 mm from axis was made. As illustrated in Figure 4.16, the background emission (orange line), which was essentially a polynomial curve, was subtracted from the original normalized measured water emission. The three coefficients to determine the polynomial curve were based upon the minimum intensity values in different wavelength regions (lower, middle and upper

wavelength region). The resulting emission spectrum was the modified measurement spectrum as shown in blue color.

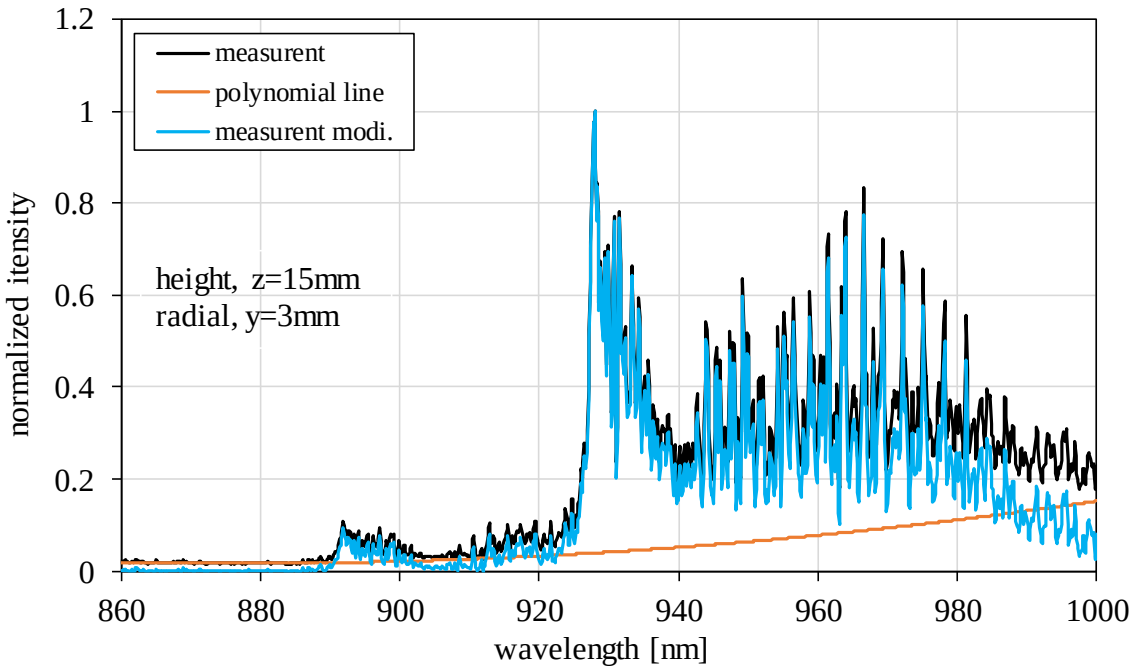

Figure 4.16 Example of underlying background emission subtraction.

Figure 4.17 shows the modified measured spectrum in comparison to best fitting simulation. Since the spectral peaks seems only sensitive to temperature for wavelengths of 928 - 980 nm within the temperature range of interest, only the 920 - 980 nm wavelength region was displayed. The temperature was estimated to be approximately 1,620 K at a flame height of 15 mm. The uncertainty of the determined temperature was influenced by the background emission subtraction and the accuracy was estimated to be no better than ±200 K. In future studies, the origin of this background emission should be investigated in more detail.

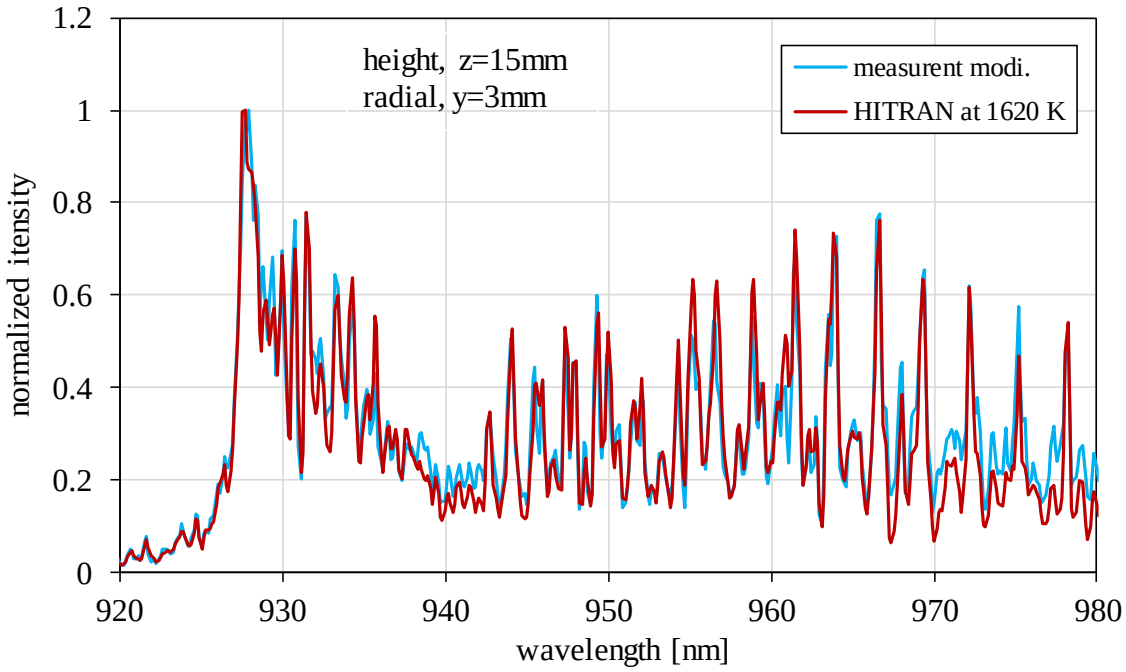

Figure 4.17 Modified measured spectrum of the water emission in comparison to the best fitting simulation.

Figure 4.18 summarized the radial distribution of integrated water emission intensity over measured wavelength region and water temperatures at different flame heights. A reconstructed flame shape from Abel inverted water emission was also illustrated here indicating the location. The flame heights of 5 mm, 15 mm, 25 mm, and 35 mm were selected for analysis due to their distinct flame shape characteristics. The blue curve represented the integrated line-of-sight water emission intensity over measured wavelength and the black dashed curve represented the Abel inverted intensity. The temperatures of water were determined from HITRAN simulation were displayed as orange dots. Generally, the temperature distribution follows the trend of the Abel inverted intensity distribution.

At flame height of 5 mm, the water emission was mainly originated from chemical reaction zone and the peak temperature was found to be 1,600 K. The temperature

decreased quickly as the emission intensity went down with radial location. The emission intensity was barely detected in the inner part of the flame indicating not much water located in this region. Similar phenomenon was found at flame height of 15 mm except that the peak temperature was, slightly higher, 1,640 K, and that the width of water emission became larger due to the diffusion of combustion reactants and products. At flame height of 25 mm, in the inner part of flame, significant water emission was detected and the temperatures were almost a constant of 1,640 K within 3 mm radius region. At flame height of 35 mm, the peak water emission and temperature were found in the center of flame.

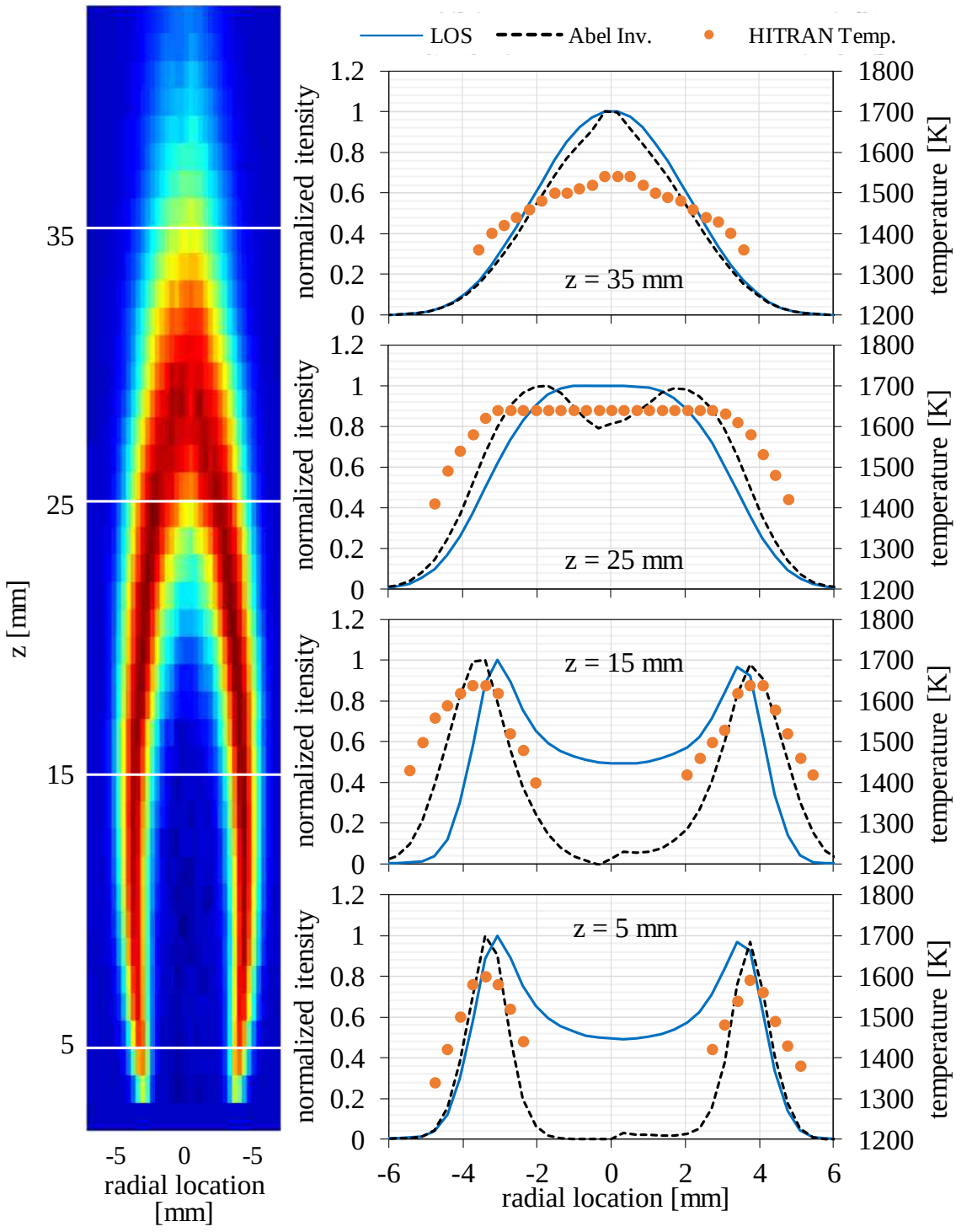

Figure 4.18 Radial distribution of integrated water emission intensity over measured wavelength region and water temperatures at different flame heights.

5.1 Experimental Setup

5.1.1 Microflames burner setup

Figure 5.1 shows a schematic of the clustered microflames burner setup which was designed by Hirasawa from Chubu University, Japan [60, 102]. The burner had one central air nozzle with a diameter of 0.7 mm and six 0.23 mm diameter fuel nozzles around the air nozzle spaced evenly. Three pitch sizes were studied in which the six fuel nozzles were placed at 2.0 mm, 2.5 mm, and 3.0 mm distance to the air nozzle in the *x*-*y* plane. Six fuel nozzles extended 3 mm above the base of the burner with the upper edge of the fuel nozzles 1.5 mm above the upper edge of the air nozzle. Research grade methane was used as fuel, with the flow rates of methane and air being controlled by two different mass flow controllers. Visual images of the flames were recorded through a Nikon DSLR camera.

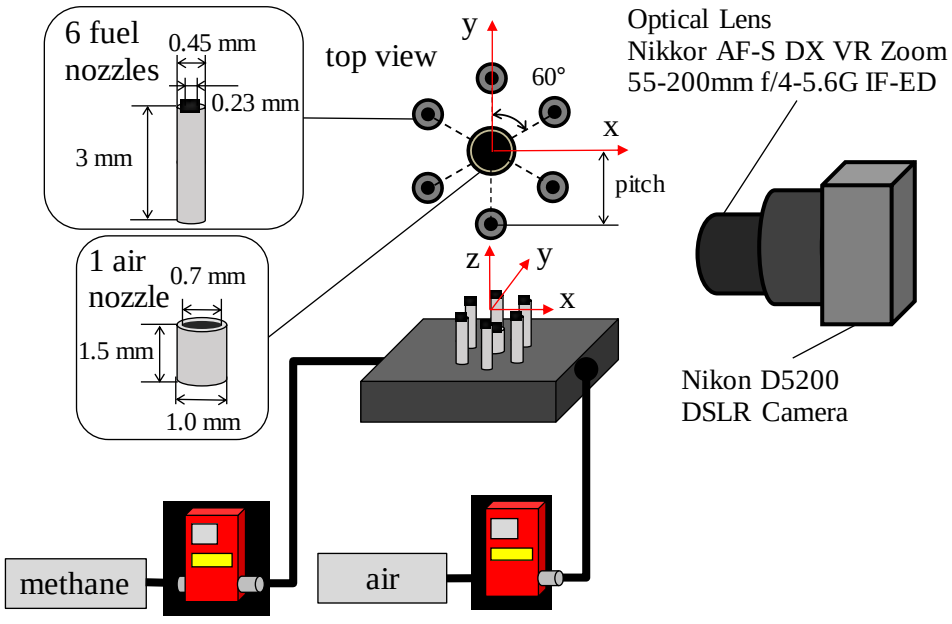

Figure 5.1 Schematic of the six clustered microflames burner with Nikon camera.

5.1.2 *Spectrometer setup*

Figure 5.2 shows a schematic of the optical setup for emission spectroscopy. Molecular emission from 400 to 450 nm is of main interest for the analysis of CH^* emission. A horizontal motion (y) translation stage was used to move the burner platform and enabled measurements of vertical lines of species emission at different horizontal locations within the microflames. Through a 445 mm focal length parabolic mirror, with the chosen de-magnification of ~2, a region of about 12 mm above the nozzles was imaged by the CCD camera. Successive clusters of 10 rows on the CCD were binned, which then provided a total of 40 spectra per image, each one representing a spatial average over a 0.375 mm vertical distance.

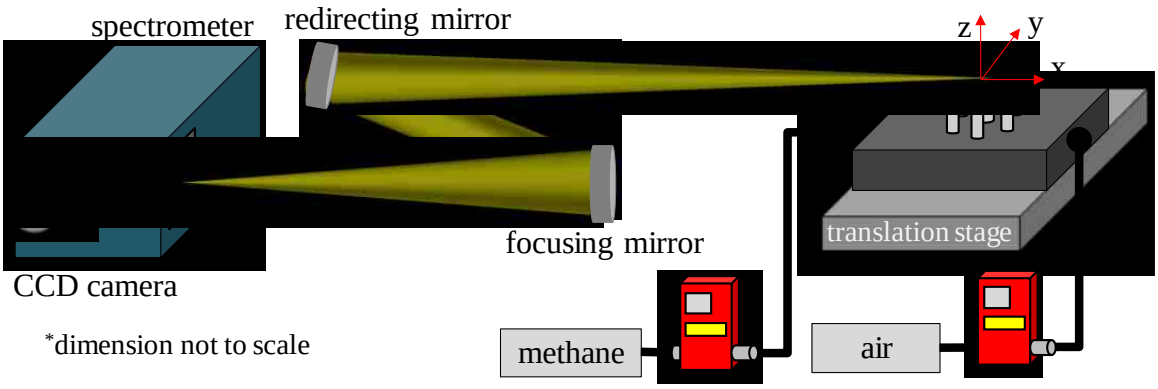

Figure 5.2 Schematic of the optical setup for CH^* and C_2^* chemiluminescence measurements.

5.2 Results and Discussion

5.2.1 *Photographically measured microflames structures*

The clustered microflames shapes for different pitch size burners at selected fuel and air exit flow rates are shown in Figure 5.3. The flame structure changes with the pitch size of the burner and the fuel and air flowrates.

In general, the microflames heights were larger when using a 2.0 mm pitch burner in comparison to when using a 3.0 mm pitch burner with equal fuel and air flowrates. The largest flame height was 2.4 mm for the 2.0 mm pitch burner when CH_4/air flowrates are 50/40 cm^3/min, whereas the flame height remained constant at 1.8 mm with the 3.0 mm pitch burner at all flowrates. A flame sheet was always established above the air nozzle on the center of 2.0 mm pitch burner because of the rather short distance between air and fuel nozzles.

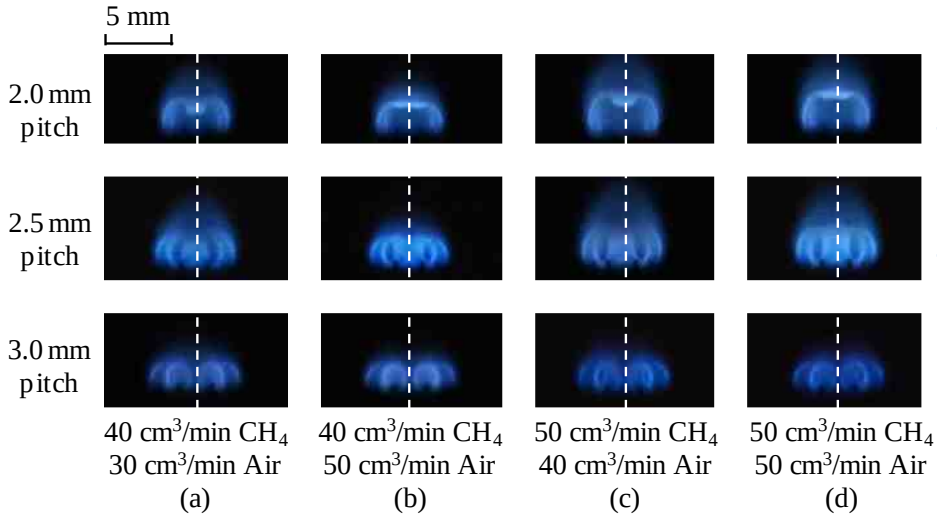

Figure 5.3 Comparison of photographically measured visible flame sheets of different pitch size burners at selected CH_4/Air flowrates.

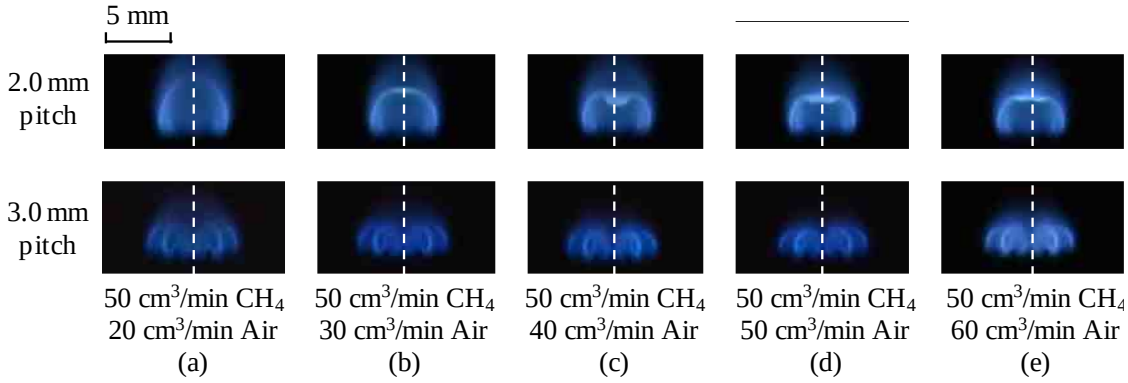

Figure 5.4 Comparison of photographically measured visible flame sheets of 2.0 mm and 3.0 mm pitch size burners at 50 cm^3/min CH_4 and varied air flowrate.

A comparison of the flame sheets for a constant methane flowrate of 50 cm^3/min and varied air flowrate is shown in Figure 5.4 for the 2.0 mm and 3.0 mm pitch burners. For the 2.0 mm pitch, the structure of the microflames changed significantly as the air flowrate was varied. When the air flowrate was low, the six microflames appeared as one single microflame. As the air flowrate was increased, a flame sheet appeared on the top of the flame structure, the top of which garnered a 'hat-like' structure when the air flowrate was greater than 40 cm^3/min. In contrast, no change in the structure of microflames was found when the 3.0 mm pitch burner was used with the same fuel flowrate. This behavior is explained by the larger distance between the air and fuel nozzles for the 3.0 mm pitch burner, which prevents the center nozzle airflow from influencing the methane flow from the fuel nozzles. Consequently, each fuel nozzle tended to establish its own individual microflame.

5.2.2 Extraction of the flame shape from the molecular spectra

To understand the effect of burner pitch size and the airflow rate on the shape of the merged flame, the experimental conditions were set as shown in Table 5-1 with the methane flow rate kept constant.

The spectrometer was set to the 300 lines/mm grating, yielding a useable wavelength range of 172.6 nm with a pixel resolution of 0.13 nm. This configuration enabled a simultaneous detection of different vertical positions (z, defined as the height above the fuel nozzle) across the whole flame with a region of about 15 mm was imaged onto the CCD. Successive clusters of 10 rows on the CCD were binned, yielding a total of 40 spectra per image, each one representing a spatial average over 0.375 mm vertical distance in the flame.

A translation stage was used to move the burner platform horizontally in steps of 0.635 mm to enable scans of vertical lines at different horizontal locations within the microflames, thus mapping the whole flame. Each individual measurement took an exposure time of 60 seconds to obtain sufficient spectral signals.

Table 5-1 Test matrix for Optical Emission Spectroscopy (OES).

No.	burner pitch (mm)	Methane flow rate (cm^3/min)	Airflow rate (cm^3/min)	Applied diagnostics
1	2.0	50	0	OES
2	2.0	50	40	OES
3	2.5	50	0	OES
4	2.5	50	40	OES

Measurements with a spectral resolution of 0.13 nm and a spectral range of 172.6 nm were conducted to observe the emission of the CH $A^2\Delta$-$X^2\Pi$ system for the Δv = 0 bands and C_2 $A^3\Pi$-$X^3\Pi$ system (Swan) for the Δv = +1, 0 and -1 bands. Each scan measured a vertical line of ~15 mm as illustrated in Figure 5.5. At heights above about z = 6 mm, the CH^* signals vanished quickly and no useful information could be extracted. A typical emission spectrum observed is shown in Figure 5.6 in which Δv = -1, 0, and 1 band systems of C_2 Swan system around 470 nm, 510 nm, and 560 nm, respectively, are simultaneously observed in each spectrum. All band systems are used for temperature determination but only the strong Δv = 0 bands, located in the wavelength region between 501 and 517 nm with the (0,0) band being the strongest at 516.5 nm, are used for the investigation of the integrated emission.

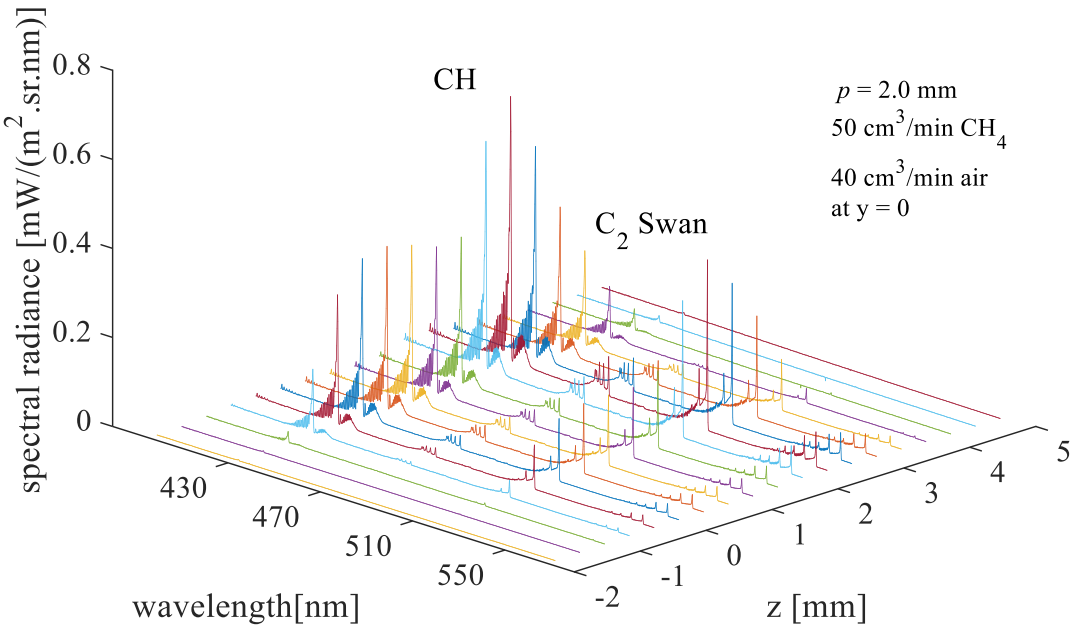

Figure 5.5 Example of observed emission spectra at y = 0.

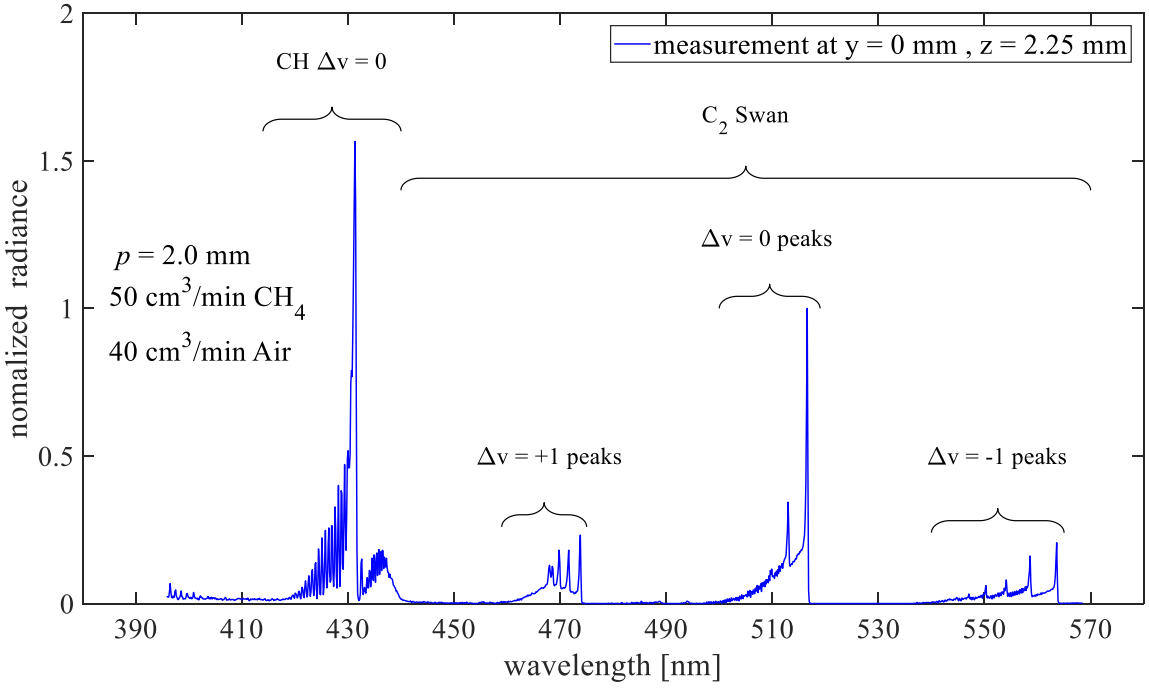

Figure 5.6 Example of measured emission spectrum containing molecular emission of the CH Δv = 0 and the C_2^* Δv = -1, 0, and 1 molecular bands.

The parallel investigation of the complex three dimensional flame shape was done by our collaborators Hirasawa and Ishino. A spatially resolved three dimensional mapping of the active flame zone was achieved by analyzing the filtered imaging measurements of CH^* with computed tomography methods developed by Ishino [60]. Their results confirmed thin flame sheets as anticipated for the combination of inverted and regular diffusion flames but also showed the merging of the individual microflames for the smaller pitch geometry. Thus, tomographically analyzed filtered imaging of the CH^* emission allowed for assigning the measured temperatures to the thin flame sheets.

To obtain flame shape information, images, similar to filtered imaging applications, were reconstructed by integrating the emission of the $\Delta v = 0$ molecular bands of CH^* and C_2^* over the individual band widths. Starting from centerline of the air nozzle as $y = 0$ mm, a total of 15 scans of vertical lines measurements were conducted with a step distance of 0.635 mm in each (±) y direction, to cover the entire flame.

Direct DSLR photographs and flame structures reconstructed from the spectrally resolved measurements of CH^* and C_2^* as shown in Figure 5.7 were used to obtain an overall flame shape. When no air was supplied to the center nozzle, as shown in Figure 5.7(a) and (c), there were little interactions among the microflames. When a 40 cm^3/min airflow was applied to the center nozzle of the 2.0 mm pitch burner, operated with methane flow rates of 50 cm^3/min, an additional 'hat-like' flame sheet appeared on the top of the flame structure at a distance of about 3 mm to the fuel nozzle exit, as shown in Figure 5.7(b).

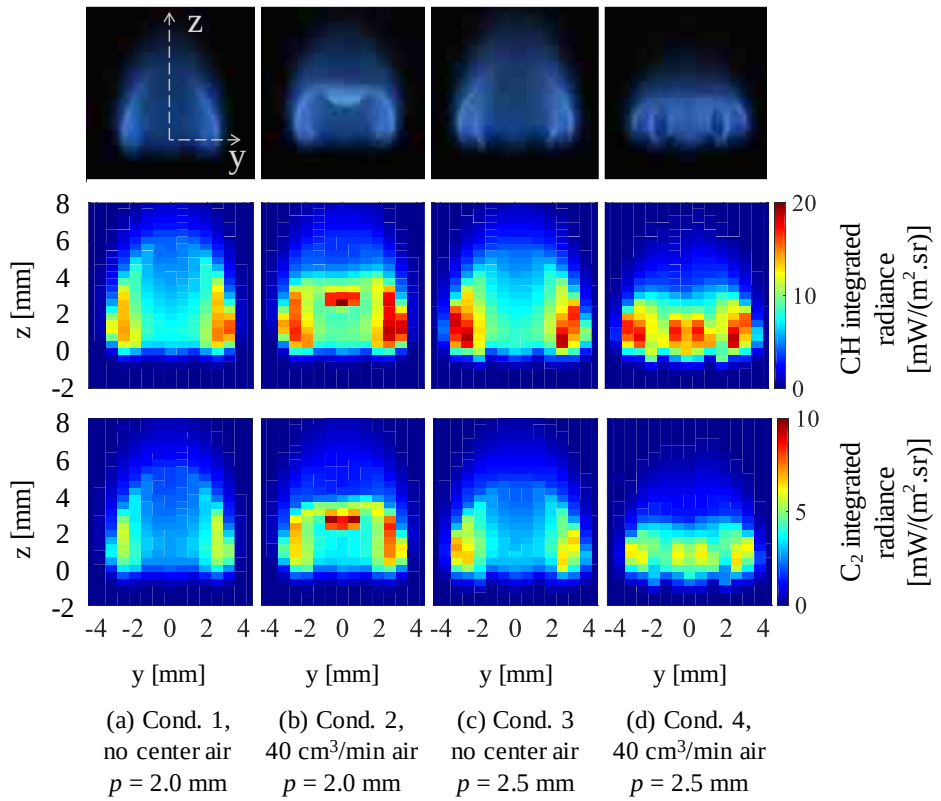

Figure 5.7 Photographs of the flame, measured CH^* and C_2^* Δv = 0 band intensities.

For premixed methane-air flames, Kojima et al. derived empirical correlations between the C_2^*/CH^* emission ratio and the equivalence ratio [50] as shown in Figure 5.8. A fit to this correlation data was used to determine the local equivalence ratios in Figure 5.9 from the C_2^*/CH^* ratios measured in the microflames structure.

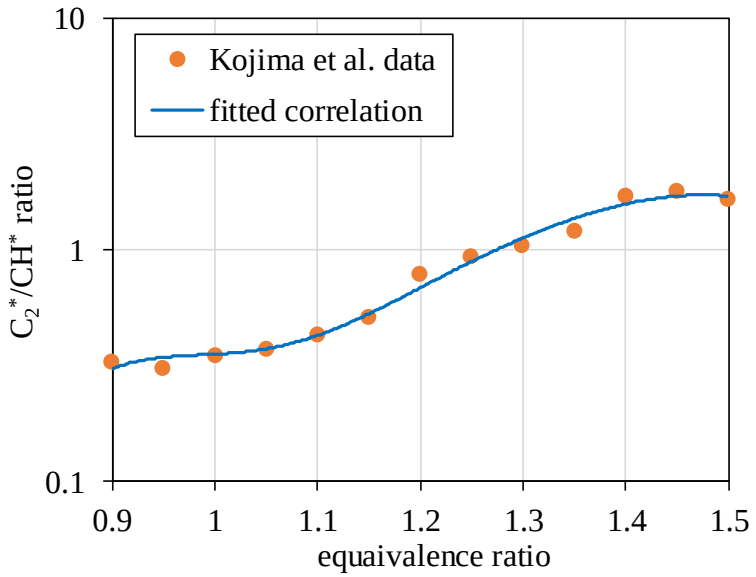

Figure 5.8 Fitted correlation between C_2^*/CH^* emission ratios and local equivalence ratio derived from Kojima et al. data measured in premixed methane-air flames [50].

Figure 5.9 shows the C_2^*/CH^* intensity ratios in a color coded scale. As can be seen, the C_2^*/CH^* intensity ratio is almost the same throughout the flame except for a burner pitch size of 2.0 mm and a center airflow of 40 cm^3/min, shown in Figure 5.9(b) where the C_2^*/CH^* intensity ratios are closer to the value at 'hat-like' region.

Despite the fact that these correlations were measured for premixed flames, the resulting equivalence ratios of one did indeed confirm the expected diffusion flame structure for test conditions 1, 3, and 4. The unique result, however, was obtained in test 2 shown in Figure 5.9(b), which showed equivalence ratios clearly larger than one in the upper part of flame structure. This result suggests that a fuel rich premixed flame zone was established in the "hat-like" concave flame structure seen in Figure 5.9(b) where the individual microflames merge to a new single flame structure.

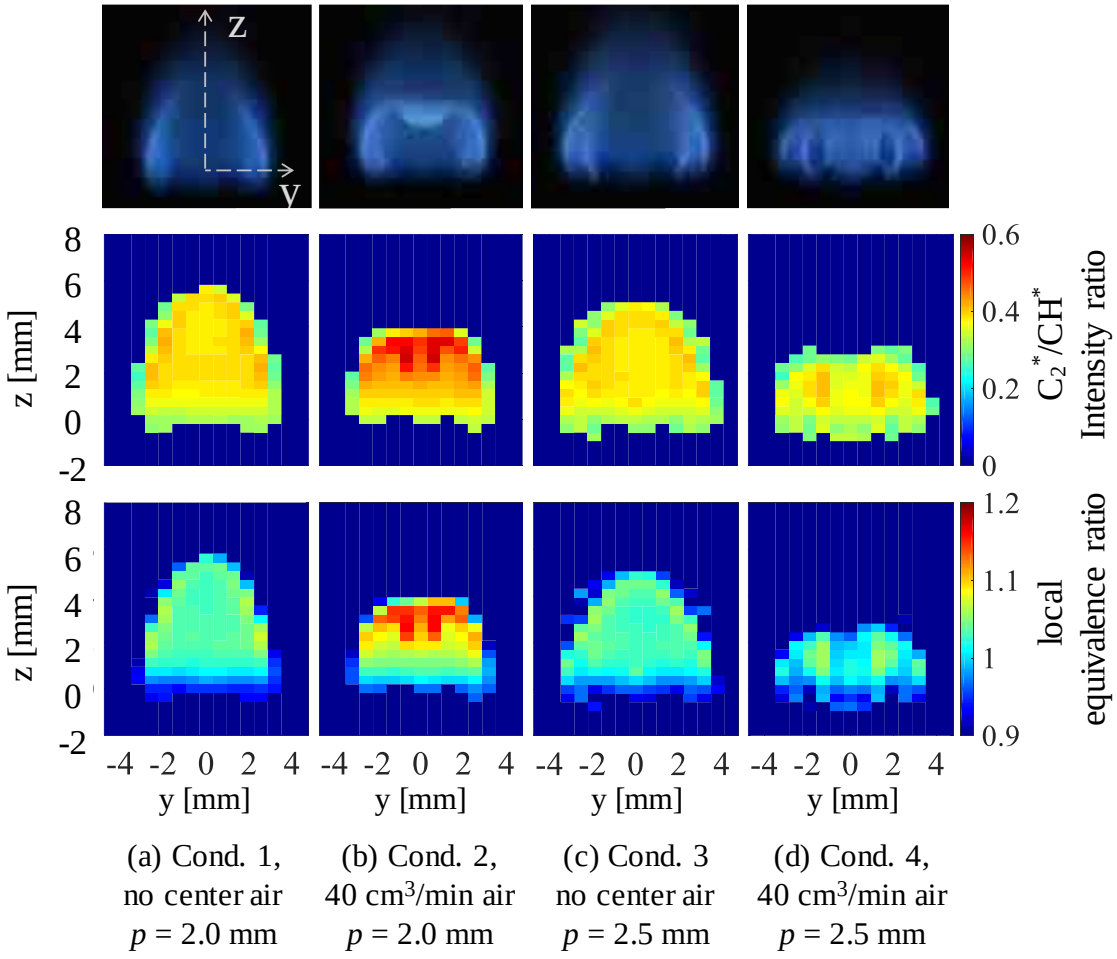

(a) Cond. 1, no center air p = 2.0 mm

(b) Cond. 2, 40 cm^3/min air p = 2.0 mm

(c) Cond. 3 no center air p = 2.5 mm

(d) Cond. 4, 40 cm^3/min air p = 2.5 mm

Figure 5.9 Ratios for the test cases 1 through 4 (Table 5-1).

5.2.3 *Temperature determination from CH* chemiluminescence*

Measurements at high spectral resolution with $\Delta\lambda$ = 0.02 nm were performed between 415 and 445 nm to monitor the emission of the $A^2\Delta$-$X^2\Pi$ transition of electronically excited CH to determine rotational and vibrational temperatures of this species. Electronically excited CH is a by-product of the combustion chemistry and, therefore, the chemiluminescent intensity from the CH* excited radicals can be used to identify the location of the combustion reaction zone [48, 103, 104]. In the present measurements, the spatial distribution of the CH* emission agreed well with the observed blue methane flame.

The spectra are caused by transitions due to electronic, rotational, and vibrational excitations [105] with a superposition of spectra from vibrational upper states 0 to 3 of the CH $A^2\Delta$ electronically excited state. The rotational excitation is known to take only a few collisions to equilibrate with the translational or gas dynamic temperature, vibrational levels on the other hand take longer to equilibrate [105]. In addition, excitation through chemical processes will most likely create a non-thermal distribution of excited states, both in electronic and vibrational excitation [105].

To determine rotational and vibrational temperatures, the measured spectra were compared with theoretical CH^* spectral simulations using LIFBASE [106]. Simulated spectra are displayed in Figure 5.10 where emission from the higher vibrational quantum numbers was arbitrarily scaled up to show their spectral structure. In the present measurements, the emission from $v = 3$ was already too weak to have significant influence on the spectra.

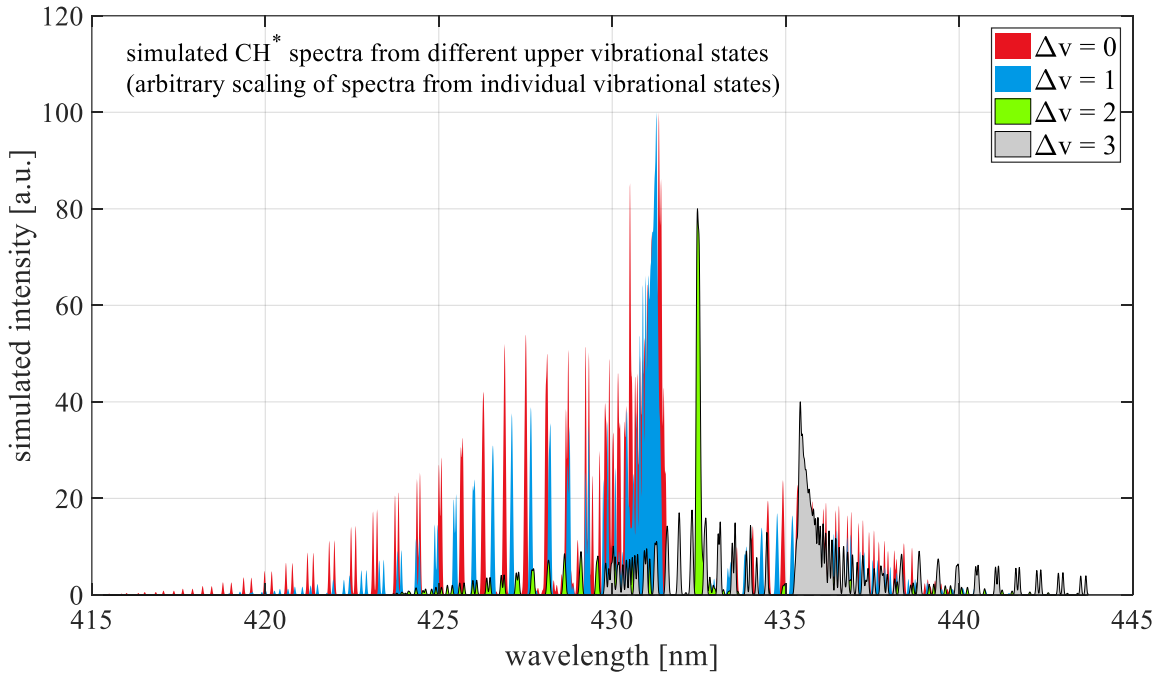

Figure 5.10 Theoretical spectra of the CH $A^2\Delta$-$X^2\Pi$ electronic system for individual upper vibrational levels (arbitrarily scaled), simulated with Lifbase [106].

A typical best fit between measured spectra and simulated ones is shown in Figure 5.11 for a distance of 0.75 mm to the fuel nozzle exit. Due to a different spatial smearing left (blue) and right (red) to the band head at 431 nm, different temperatures were needed to fit the spectra between 418 and 430 nm and between 430 and 440 nm. The resulting rotational temperatures were considered upper and lower bounds for the reported temperature which is the average of these two extremes.

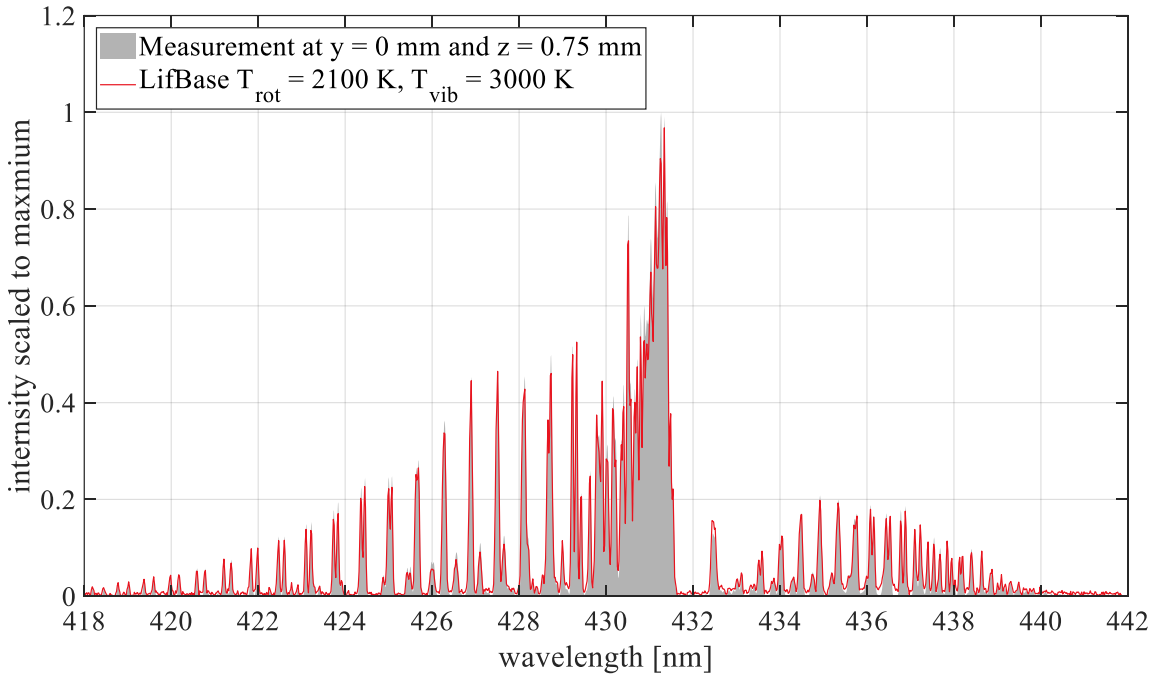

Figure 5.11 The measured spectrum of the $\Delta v = 0$ transitions of the CH $A^2\Delta$-$X^2\Pi$ electronic system in comparison to the best fitting simulation.

The rotational temperature showed peak values close to and slightly above the adiabatic flame temperature for methane air combustion. Two different equivalent vibrational temperatures were found by fitting the ratio between the dominant lines from the 0-0 transition and the features from $v = 1$ on the blue side of the spectrum (weak ro-vibrational lines between 425 and 428 nm) and the main feature of the 2-

2 transition at 432.5 nm on the red side of the spectrum. These temperatures were clearly above the rotational temperatures. They reflect the population of the vibrational levels 1 and 2 relative to the level 0 and indicate a non-thermal vibrational population of CH^* which is assigned to be populated through chemical reactions.

Figure 5.12 shows the vertical distributions of CH^* rotational and vibrational temperatures for the 2.5 mm pitch size burner at flowrates of 40 cm^3/min CH_4 and 50 cm^3/min air. A maximum of 7 out of the 40 measured vertical positions contained data which were suitable for temperature analysis. The vertical profiles at each x position were obtained by moving the burner platform on a translation stage. At heights of about 1.5 mm above the fuel nozzles, the CH^* emission was already rather weak yielding high uncertainties in the temperatures. The rotational temperature increased as the distance became closer to the flame tip, with values of about 1,500 K at about 0.75 mm below the fuel nozzle exit (z = - 0.75 mm) to peak values of about 2,450 K at the flame tip at z = 1.5 mm. The vibrational temperatures were clearly higher than the rotational ones (and higher than the adiabatic flame temperature for methane-air combustion) and showed only slight variation with distance to the nozzle. They are not likely linked to the flame temperature, though, since the primary population of the excited states is anticipated through non-thermal excitation (*i.e.* chemiluminescence). The minimum uncertainty is certainly the temperature step in the simulated spectral data base. The uncertainty of the stated temperature values contains uncertainties in fitting the spectra (i.e., if two simulated spectra fit the measured one in a very similar way) and in uncertainties of the measured signal due to the factors mentioned in chapter 3.2.1). Also, two temperatures were obtained from those two regions of the wavelength, which gave the upper and lower limit of determined temperatures and the accuracy was estimated to be no better than $\pm$200 K. One reason is that the left and right of the band peak are dominated by transitions coming from different upper vibrational levels. Therefore, this indeed characterizes some uncertainty.

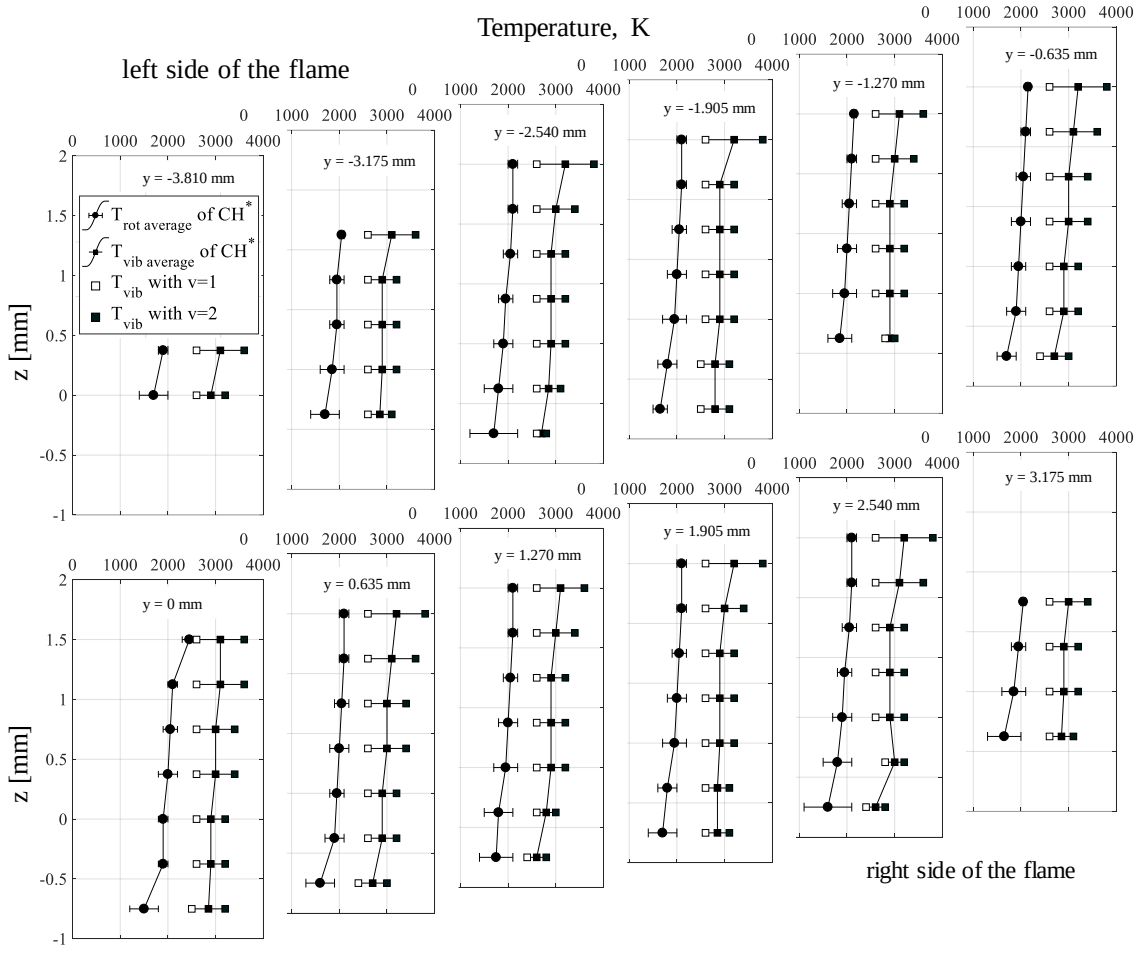

Figure 5.12 Vertical distributions of CH^* rotational and vibrational temperatures for the 2.5 mm pitch burner at flowrates of 40 cm^3/min CH_4 and 50 cm^3/min air.

In the present measurements, the spatial distribution of rotational temperature across the microflames as shown in Figure 5.13(c) were obtained by mapping the 2-D distributions of CH^* rotational temperature. The 2-D intensity distribution of CH^* emission was obtained from the spectra integration over the CH^* band system (basically the gray area under red curve in Figure 5.11) as shown in Figure 5.13(a). The spatial distribution of the CH^* emission agreed well will the blue color of the methane-air flame seen in photographic images Figure 5.13(b).

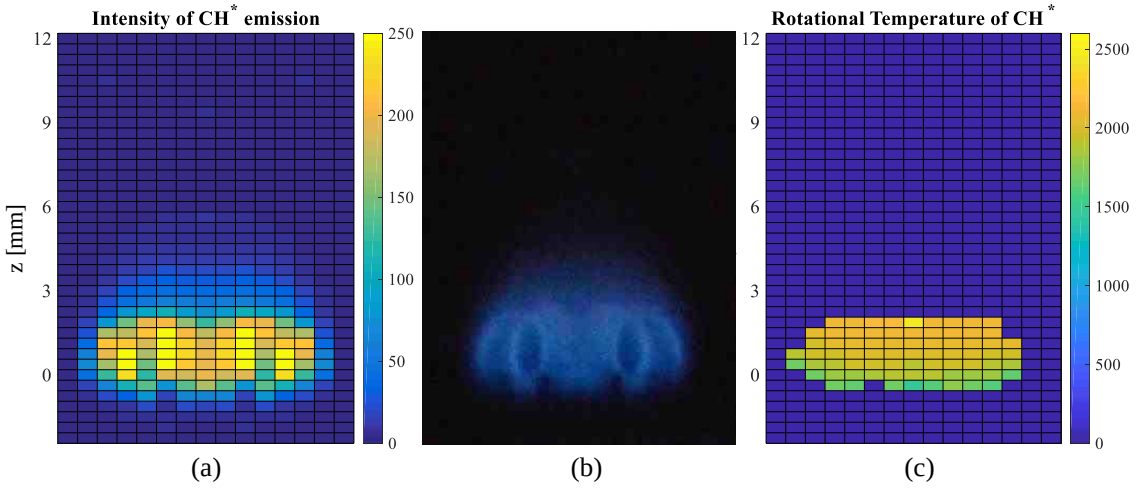

Figure 5.13 Intensity distribution of CH^* emission (a), photographic image (b) and rotational temperature distribution of CH^* (c) for 2.5 mm pitch size burner at flowrates of 40 cm^3/min CH_4 and 50 cm^3/min air.

Again, each measurement is an integration over the line of sight. However, CH^* is produced and radiates in the flame front which is relatively thin in diffusion flames. Therefore, the observed CH^* emission is actually the sum of the flame fronts at the measured vertical and horizontal position. The temperature does not correlate directly with the intensity but rather is a function of distance to the fuel nozzles exit (z) as shown in Figure 5.13(a) and (c).

5.2.4 Temperature determination from C_2 Swan system

The advantage of spectrally resolved measurements of the molecular emission from the flame sheets over filtered emission of the same chemiluminescence is that the spectral shape of the molecular bands contains information about the gas temperature. While vibrational excitation is mainly generated through the chemical reaction generating the chemiluminescence, the rotational temperature of diatomic molecules, however, equilibrates usually rather quickly with the translational temperature and is considered a good representation of the gas-dynamic temperature of the flame.

Spatial resolution is assigned to the spectroscopic measurements through a comparison with tomographically analyzed images of the CH^* chemiluminescence from an earlier study [60] showing thin flame sheets as the sole origin of the CH^* emission. From the results presented in Figure 5.14, very similar structures are seen in the emission of CH^* and C_2^* which strongly indicates that the emission of the two radicals is generated in the same location in the flame structure.

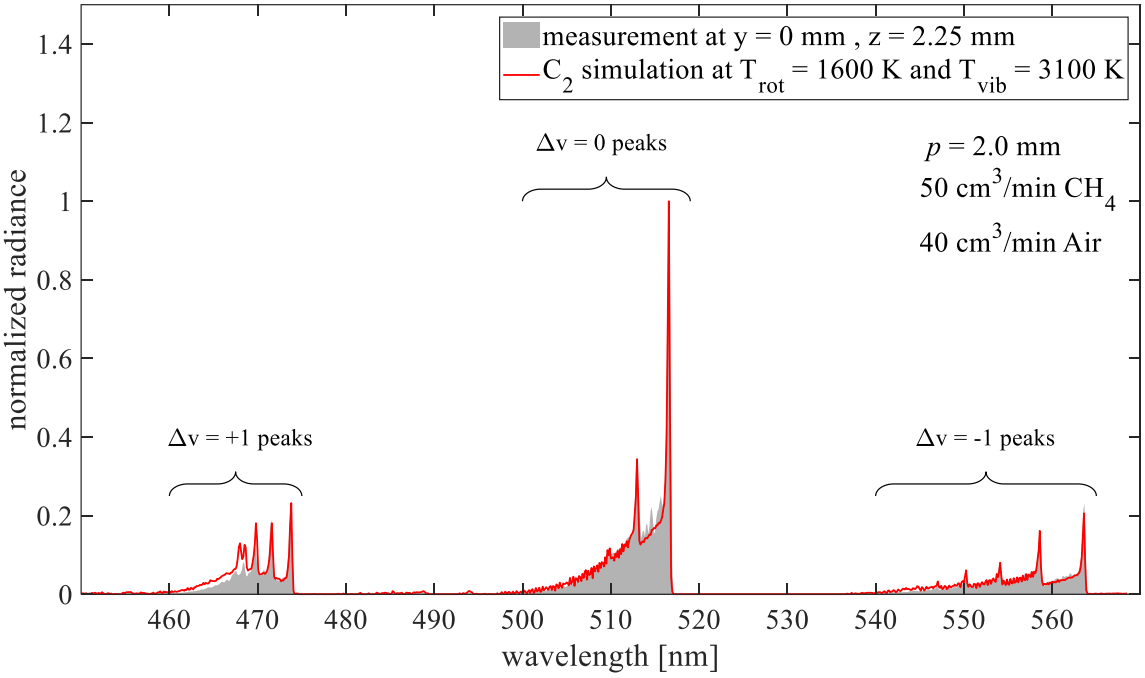

Figure 5.14 Comparison of a measured spectrum with a simulated spectrum calculated using NEQAIR.

Theoretically simulated C_2^* spectra were calculated using the NASA Nonequilibrium Air Radiation code NEQAIR [107] under separate variation of the rotational and vibrational temperature for rotational temperatures ranging from 1,000 to 3,000 K with an increment of 100 K, and for vibrational temperatures between 1,500 to 4,000 K with an increment of 200 K. All spectra were normalized to the (0,0) peak of C_2 Swan band.

The rotational and vibrational temperatures of C_2^* were determined through comparing the spectral shapes of measured and simulated emission of the Δv = +1, 0 and -1 bands to find the best fitting simulation as shown in Figure 5.14. Excellent agreement was obtained between measurements and simulations with the exception of two peaks around 468 nm which were systematically under predicted by the simulation. It is not clear yet whether these discrepancies resulted from inaccurate constants in the simulation or potential inaccuracies in the experimental procedure.

The observed C_2^* emission consists of an integration over the line-of-sight (along x) at the measured vertical and horizontal position and therefore does not provide any spatial information by itself. However, C_2^* and CH^* emission are generated at the same locations in the flame, as concluded from the very similar flame structures seen in Figure 5.7. They are only generated in the active combustion zone, which in these diffusion flames is a thin flame sheet as demonstrated by Kato et al. [60] through tomography of filtered imaging of the CH^* emission. Therefore, only these narrow regions contribute to the line-of-sight integrated emission, and the measured temperatures can be assigned to discrete flame locations through comparison with the tomographically analyzed filtered emission measurements.

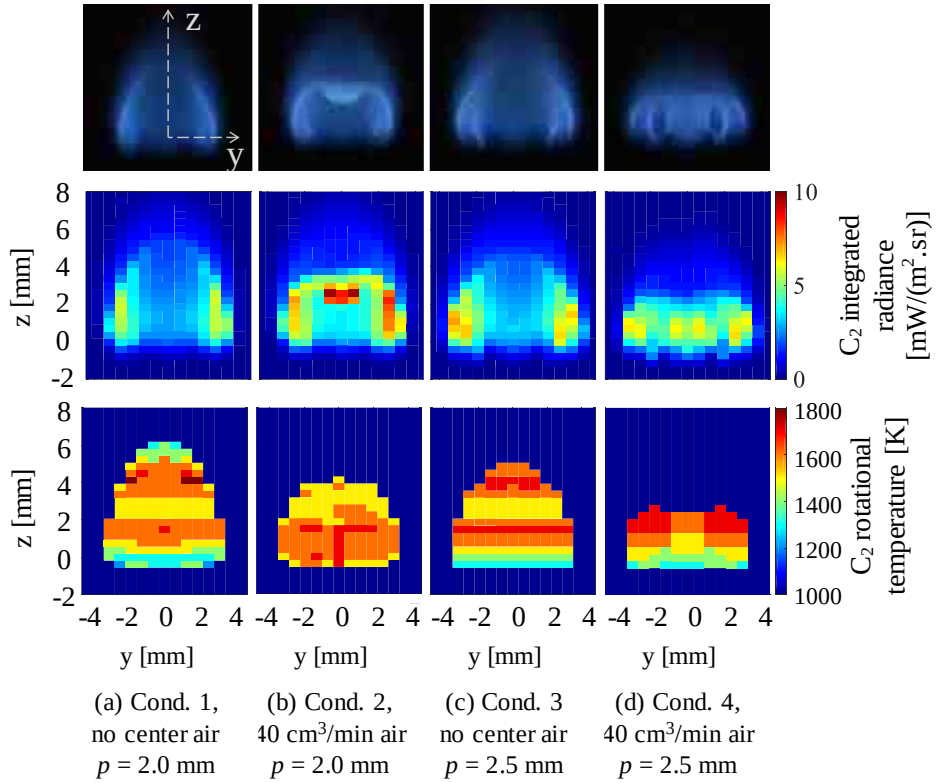

Figure 5.15 Rotational temperature distributions for (a) condition 1, (b) condition 2, (c) condition 3, and (d) condition 4.

The rotational temperature distributions for different flow rates and pitch size burners are illustrated in Figure 5.15. The rotational temperatures range from 1,200 K to 1,800 K. Similar to the analysis of CH^*, the accuracy was estimated to be no better than ±200 K. Different from the emission intensities, the temperatures do not show significant profiles in the horizontal direction but are mainly a function of height above the fuel nozzles, which was also seen in earlier temperature measurements from the CH^* emission [102]. The only exception is seen in Figure 5.7(d) where a reduced merging of the flames occurs due to the larger pitch size. The vibrational temperatures are found to be 3,100±200 K and show almost no variation across the flame This is assigned to the non-thermal nature of vibrational excitation which is predominantly governed by the combustion reactions.

PARTICLE EMISSION MEASUREMENT IN MICROFLAMES

6.1 Experimental Setup

6.1.1 Microflames burner setup

Figure 6.1 shows a schematic of the modified clustered microflames burner setups [34]. The burner had one central air nozzle with a diameter of 0.7 mm and six 0.23 mm diameter fuel nozzles around the air nozzle spaced evenly at a distance of 2.5 mm. The fuel nozzles were longer than the air nozzle by 1.5 mm. The seed particles were mixed into the air flow by a particle feeder and fed through the central air nozzle. Under current setup, the feeding rate of amount of particles was not controlled.

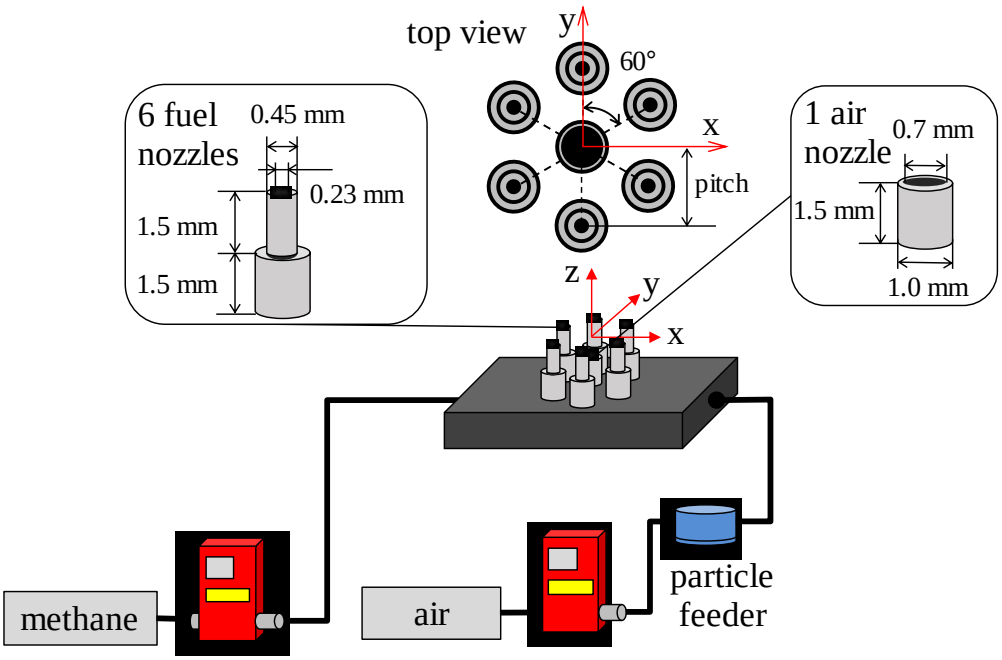

Figure 6.1 Schematic of the clustered microflames burner and particle feed system.

Research grade methane was used, with the flow rates of methane and air being controlled by two different mass flow controllers. The testing demonstrated that the fuel and air nozzle arrangement at different air and fuel flow rates influenced the flame structure. At low fuel rates, six distinct diffusion microflames were established around the center nozzle. As a consequence, the seed/air stream from the center nozzle flowed in between the microflames that were centered above each respective fuel nozzle and did not cross into the flame fronts. This seed/flame structure is referred to as the "separated open" structure shown in Figure 6.2(a). At intermediate fuel flow rates, the seed/air stream also did not cross into the methane flame front, similar to case (a), but the microflames were merged into one contiguous ring-shaped flame; this structure is referred to as the "merged open" structure and is shown in Figure 6.2(b). Then, with ever increasing fuel flow rates and even at low air flow rates, the six independent microflames merged into one large flame and the seed/air flow was injected into this merged flame. This structure, where the center flow established an inverted diffusion flame in the merged flame, is referred to as the "merged closed" structure and is shown in Figure 6.2(c). As expected, these various flame structures affected the particle seed temperature distributions, as discussed in the following section.

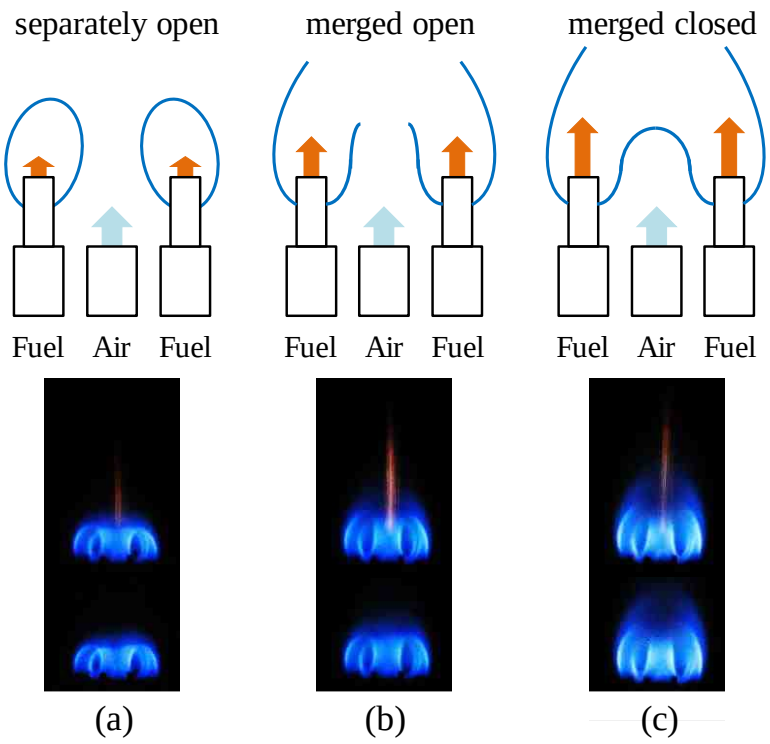

Figure 6.2 Illustration of the flame structure evolution with increasing fuel rate yielding (a) separated open, (b) merged open and (c) merged closed structures.

Table 6-1 displays the methane and air flow rates that were used during these tests. At the 20 cm^3/min methane and 30 cm^3/min air condition, marked with a symbol "×" in Table 6-1, soot was generated and obscured the collection of flame temperature data due to strong emission from the soot; hence, this flow rate data point is not discussed in the following. With 50 cm^3/min of both methane and air (case ×× in Table 6-1), the high air flow rate diluted the concentration of methane and decreased the flame temperature to an extent that particle emission intensities were too low to be detected with the current setup. TaN particles with a high melting temperature and relatively high emissivity in the spectral range between 600 and 1,000 nm were used to characterize the seed flow. Table 6-2 summarizes properties of the TaN seed particles.

Table 6-1 Test matrix on methane and air flow rates.

CH_4 \ Air	30 cm³/min	40 cm³/min	50 cm³/min
20 cm³/min	×	√	√
30 cm³/min	√	√	√
40 cm³/min	√	√	√
50 cm³/min	√	√	××

Table 6-2 Properties of TaN particles used.

Property	Value
Density (kg/m³)	1,340
Melting Point (K)	3,360
Diameter (m)	~5

6.1.2 Spectrometer setup

Figure 6.3 shows a schematic of the optical setup for emission spectroscopy. Through a 445 mm focal length parabolic mirror, the vertical center line of flame and seed particle flow was imaged onto the spectrometer side input slit, therefore providing a simultaneous detection of vertical positions across the whole particle flow. With the chosen optical imaging system, a region of ~15 mm was imaged onto the CCD as shown in Figure 6.4. To increase the sensitivity, successive clusters of 20 rows on the CCD were binned, yielding a total of 20 spectra per image, each one representing a spatial average over 0.75 mm distance in the flame. The OG-550 filter was used to eliminate higher order lines. Figure 6.4 shows view of microflames with particle beam through the spectrometer in imaging mode to show the alignment

procedure. When the slit was set to 25 μm for spectral mode, the center of slit was the same with the one at imaging mode.

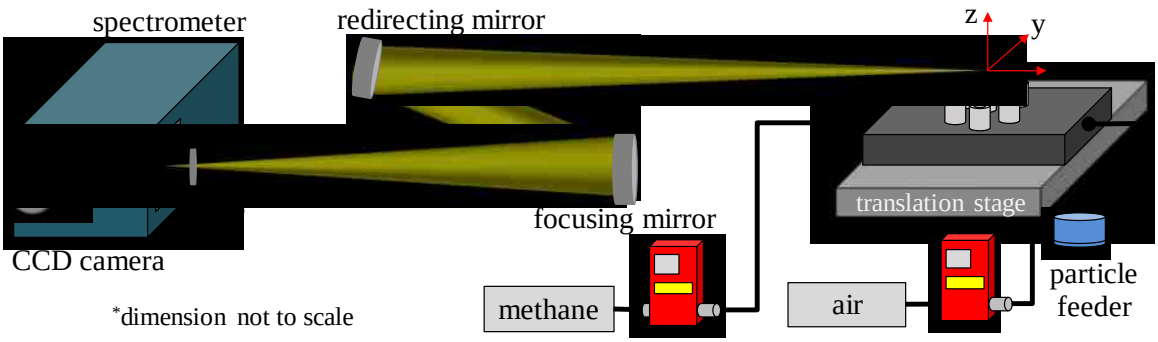

Figure 6.3 Schematic of the optical setup for optical emission spectroscopy measurements on microflames burner.

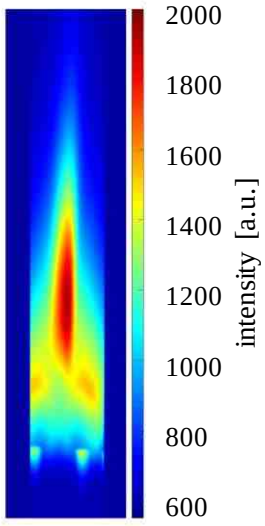

Figure 6.4 Spectrometer view of microflames with particle beam injection for alignment procedure.

6.2 Results and Discussions

6.2.1 Determination of particle temperatures from continuum emission

At a spectral resolution with $\Delta\lambda$ = 0.49 nm, the broad continuum emission of the glowing seed particles and molecular emission from water (H_2O) were monitored between 600 and 1,000 nm. The continuum emission was analyzed with respect to particle temperatures. Spectra were acquired from emissions of non-sooting (blue) flames with and without seed particles at the same flow rates. The spectra were dominated by H_2O emission and an underlying continuum which was assigned to thermal radiation from the glowing particles. Hence, the difference between the spectra with and without particle flow was used to provide the particle emission, as shown in Figure 6.5. It should be noted that the strong lines at 766.5 nm and 769.9 nm are attributed to atomic emission from potassium contamination in air.

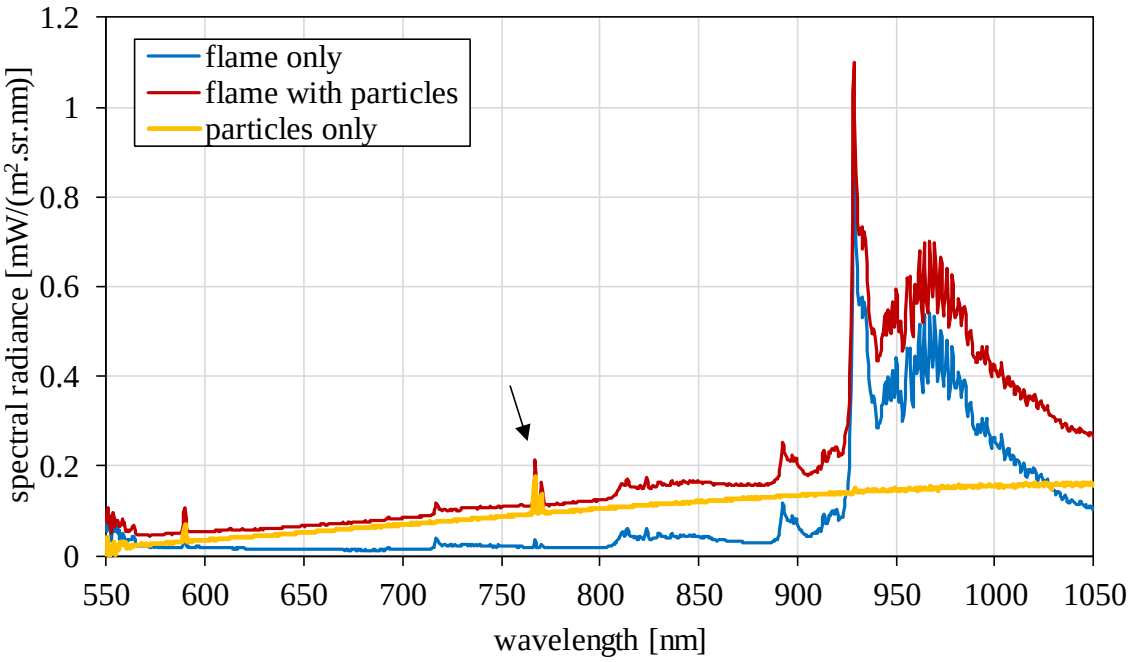

Figure 6.5 Spectral radiance from flame with and without particles.

In the optical thin case, a comparison of the spectral shape is less sensitive to measurement uncertainties than comparing absolute intensities, and becomes independent of the seed particle size. As a consequence, all spectra were normalized relative to their intensity at 790 nm and then the spectral shapes between 600 and 1,000 nm were compared to calculated Planck emission, as described in the following.

Since normalized spectra from the TaN seeded flames were used, the comparisons between the spectral shape of the measured spectra and the Planck's law calculation were of higher interest than the absolute values. In combination of Planck' law and definition of spectral, hemispherical emissivity as shown in equation (2.2) and (2.17), the theoretical spectral radiance of emission from particles is calculated as:

$$I_\lambda(\lambda,T) = \varepsilon_\lambda \cdot B_\lambda(\lambda,T) = \varepsilon_\lambda \frac{2hc^2}{\lambda^5} \frac{1}{\exp\left(\frac{hc}{\lambda kT}\right)-1} \qquad (6.1)$$

where ε_λ and B_λ are the surface spectral emissivity of particles and the spectral radiance of a blackbody at a given temperature T as a function of wavelength according to Planck's law [68]. To provide a valid comparison with the particle emission, the Planck emission has to be convoluted with the spectral emissivity of the particles. The bulk of the particles consists of TaN for which temperature dependent spectral emissivities were available from published data [108] as displayed in Figure 6.6. By interpolation from these data, spectral emissivities were obtained for each temperature used in the Planck calculations.

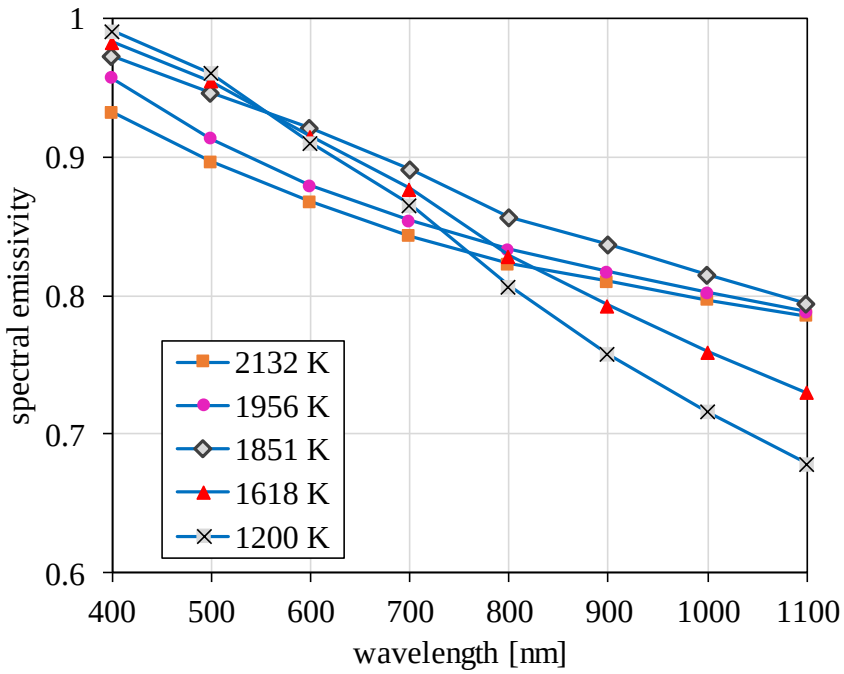

Figure 6.6 Spectral emissivity of TaN at various temperatures recreated from [108].

6.2.2 Particle size parameter

To obtain temperature information from the particle continuum emission by comparison to calculated Planck emission, it is necessary to understand the governing influences on the spectral intensity and shape. Two known major influences are scattering through the particles and the spectral emissivity of the seed material. Based on equation (2.20), for the given wavelength range between 600 and 1,000 nm, particle size parameters of ~6 and 3 are obtained for particle sizes larger than 0.5 µm. The TaN particles from Wako Chemical, Ltd were analyzed through SEM as shown in Figure 6.7. Approximately 10% of the particles were found to have sizes below 0.5 µm which corresponded to a volume fraction of less than 1% shown in Figure 6.8, suggesting that neither Rayleigh nor Mie scattering would be important.

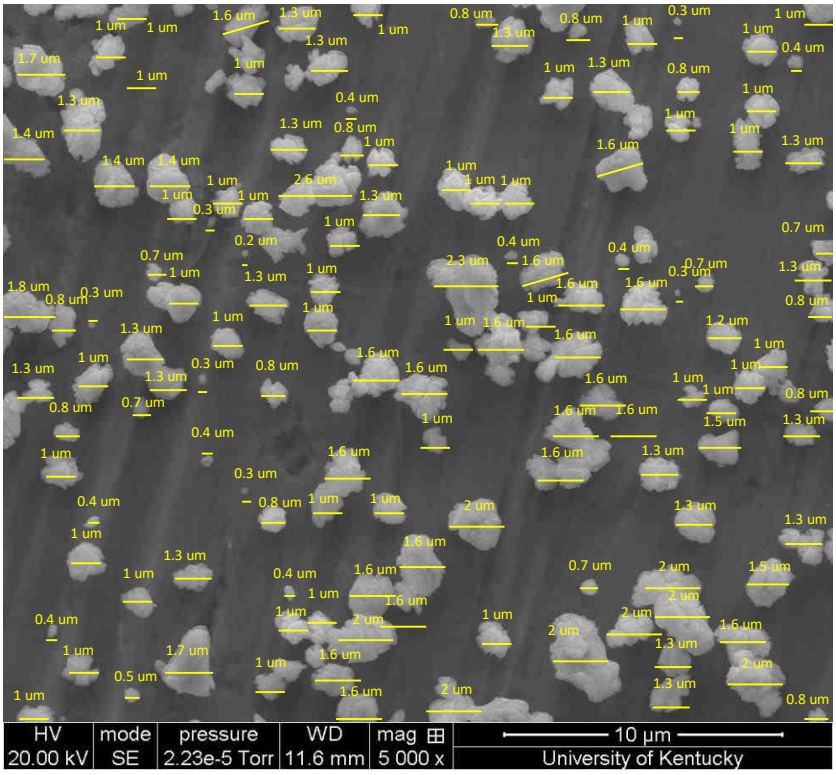

Figure 6.7 TaN particles sampled after passing through flame.

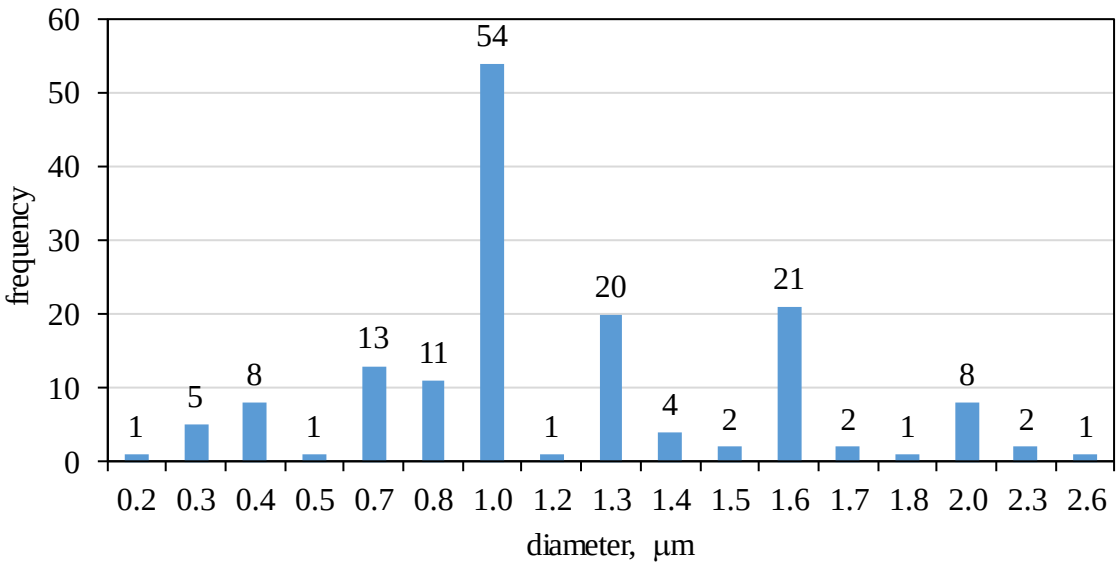

Figure 6.8 TaN particles size count.

6.2.3 *Flame transmissivity measurement*

To further verify this assumption, the transmissivity of the flame with particle seeds was determined by placing a calibration lamp emitting continuum radiation behind the flame as shown in Figure 6.9. The spectra measured with and without the lamp showed that the flame transmissivity was equal to one within the accuracy of the measurement as shown in Figure 6.10. Therefore, the flame can be considered optically thin and both scattering and absorption effects were negligible.

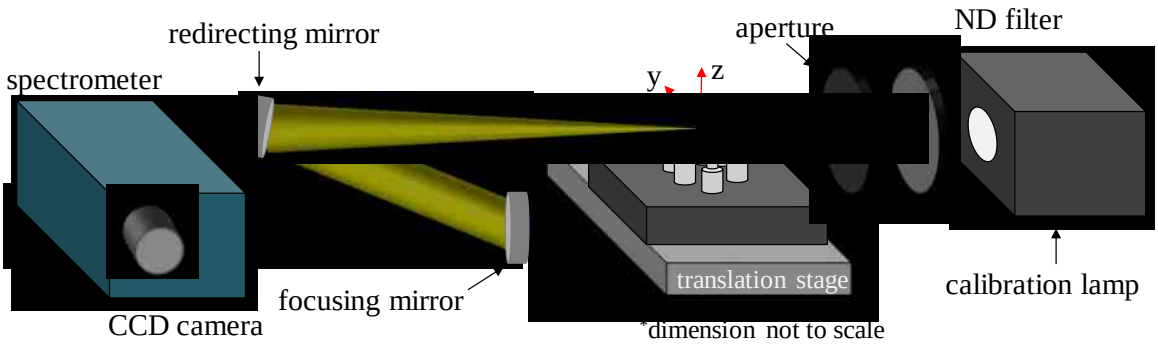

Figure 6.9 Optical setup for flame transmissivity measurement.

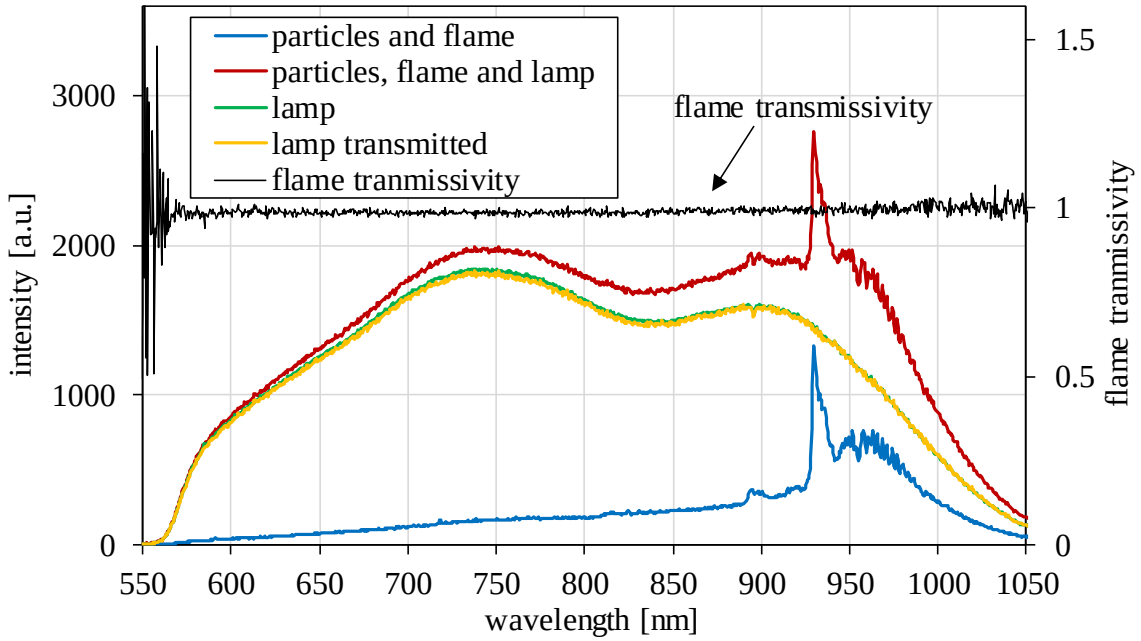

Figure 6.10 Flame transmissivity measurement.

6.2.4 Investigation of post-test particles

The second process influencing the emission of the particles is given by potential surface reactions, mainly through oxidation. When heated in the presence of oxygen, the TaN particles may undergo such oxidation reactions while passing through the flame. The generation of TaO and TaO_2 through electrodeposition has been reported in literature [109], however, Ta_2O_5 is reported as the most stable and saturated tantalum oxide. X-ray photoelectron spectroscopy (XPS) and energy dispersive X-ray (EDX) data were applied to TaN particles acquired before and after they were seeded into the flame, results of which are presented in Figure 6.11. The EDX results indeed showed the existence of oxygen on the sample surface. For the virgin particles, the oxygen signals are more or less randomly distributed over the sample. For the particles sampled when flame was established, oxygen concentrations were seen on the particles, strongly indicating oxide layers. The parallel investigation of these particles was also done by Hirasawa's group in Japan

[110]. They analyzed the particles by X-ray diffractometer (XRD), and found that the increase of fuel flow rate increased the extent of oxidation.

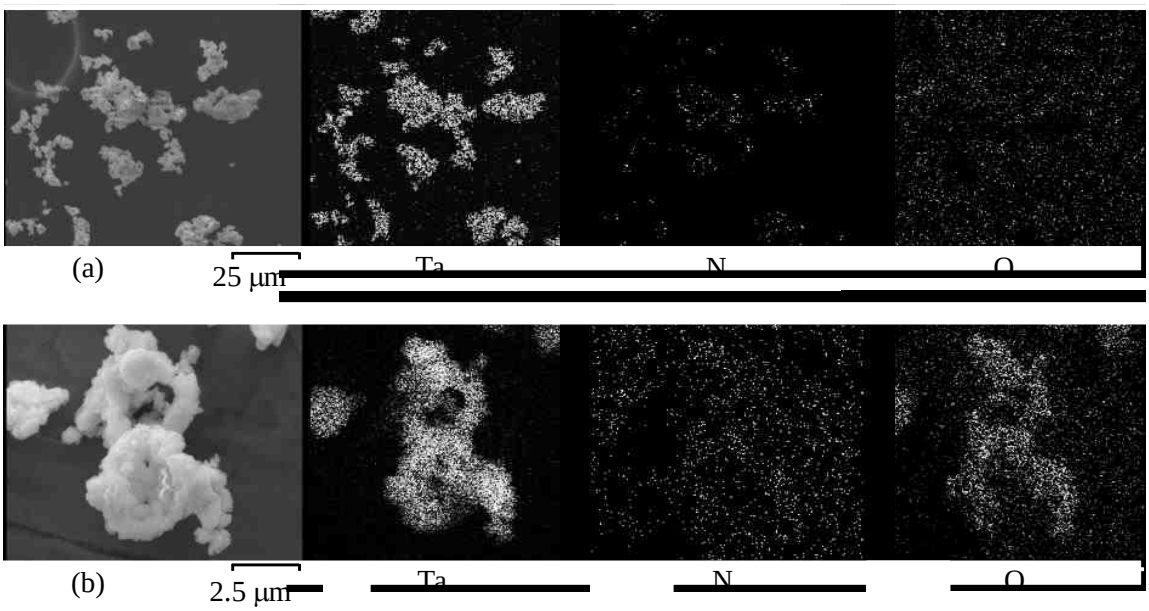

Figure 6.11 (a) SEM image of TaN particles sampled when no flame was established and EDX mapping of Tantalum, Nitrogen and Oxygen, and (b) SEM image of TaN particles sampled when a flame was established with a fuel/air flowrates of 40/50 cm^3/min, and EDX mapping of Tantalum, Nitrogen and Oxygen.

The broad XPS scan as shown in Figure 6.12 also shows significant oxygen signals (*e.g.* at ~533 eV) which might be caused by oxygen contaminants on the substrate. However, the high resolution scan reveals Ta_2O_5 signals between 26 and 29 eV [109]. Although the oxidation reaction would contribute to the heating process, a quantification of this possible heat flux contribution is not possible with the currently available experimental data. However, such an oxide layer would have an effect on the radiation emitted by the particles if it were thick enough.

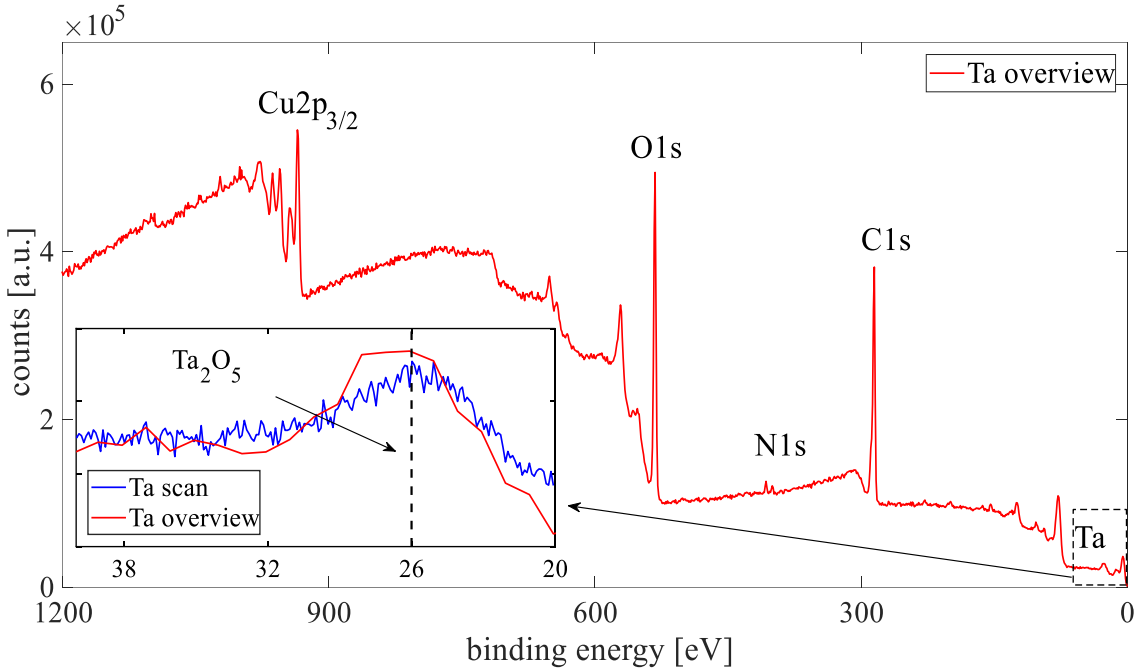

Figure 6.12 XPS Analysis of TaN particles sampled after passing through microflames with a fuel/air flowrates of 40/50 cm³/min.

The emissivity of Ta_2O_5 is very low in the wavelength range of concern [111]. Its transmittance, as reported in literature [111] for a Ta_2O_5 thickness of 370 nm, is illustrated in Figure 6.13, showing a maximum of nearly unity in the center of the observed wavelength range and an almost symmetrical decrease to values on the order of 80% at the lowest and highest observed wavelengths.

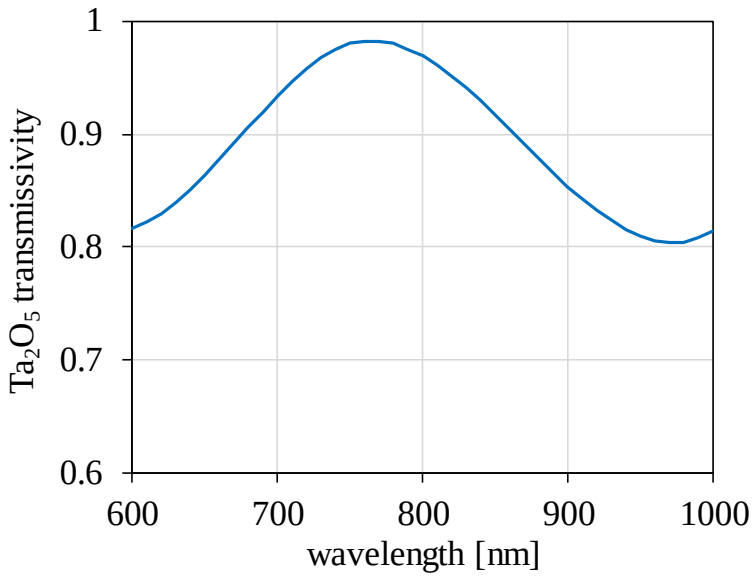

Figure 6.13 Transmittance of Ta_2O_5 recreated from [111].

The effect on the simulated Planck emission is demonstrated in Figure 6.14 for a fuel/air flowrates of 40/50 cm³/min at a distance of 5 mm to the fuel nozzles with Planck spectra of TaN with and without correction for transmission through a 370 nm thick layer of Ta_2O_5 for different particle temperatures matching the measured spectra right and left of the normalization wavelength of 790 nm. The normalized Planck emission fits the measured data in limited spectral regions but no common temperature can be found which fits the entire spectrum. This is clearly seen in the differences between Planck simulation and measurement for each temperature, normalized by the corresponding measured value, in the following referred to as percent differences. Therefore, the average Ta_2O_5 layer on the surface of the emitting particles must have been thinner than 370 nm.

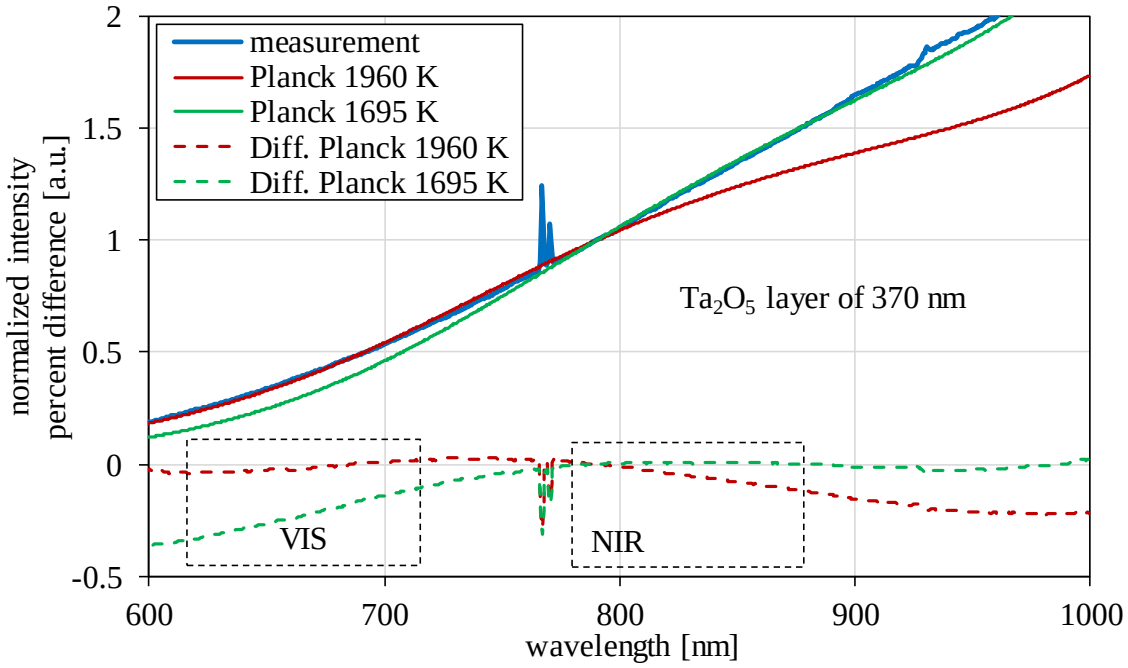

Figure 6.14 Normalized measured intensity for a fuel/air ratio of 40/50 cm³/min at a distance of 5 mm to the fuel nozzles compared to simulated Planck emission under consideration of a 370 nm thick Ta_2O_5 layer, and percent differences at temperatures matching the VIS and NIR regions.

Thinner oxide layer may be considered through the application of Beer's law [68] as shown in equation (2.14) with the layer thickness x and the spectral absorption coefficient κ_λ of Ta_2O_5 [74] which is used to calculate the spectral transmittance for different layer thicknesses than the ones reported in [111]. By applying these spectral transmittance values of Ta_2O_5 to the theoretical Planck curves within a temperature range between 1,200 and 2,400 K, optimum temperature values can be found from the best fitting Planck emission for a given Ta_2O_5 layer thickness. To obtain a quantifiable measure for the best fitting Planck curve, the difference between the measured and simulated spectra at each wavelength was built, and normalized by the measured value to obtain the disagreement of measured and simulated value in percent. The best fit was found by minimizing the sum of these percent differences in two different wavelength regions of 110 nm width left (VIS)

and right (NIR) of the normalization wavelength of 790 nm. Two temperatures can be found which minimize the sum of the squared percent differences in each wavelength region. A third temperature results from a minimization of the sum over both wavelength regions, yielding the best fitting Planck curve.

For each measured spectrum, this fitting procedure was conducted under variation of the oxide layer thickness from pure TaN surfaces up to oxide layer thicknesses of 500 nm in intervals of 10 nm, yielding a best fitting Planck curve with an originating temperature and oxide layer thickness as an average over all detected particles. For the vast majority of measured curves the originating temperature for the best fitting curve in the VIS, NIR, and over the whole detection range coincide in this point as shown in Figure 6.15.

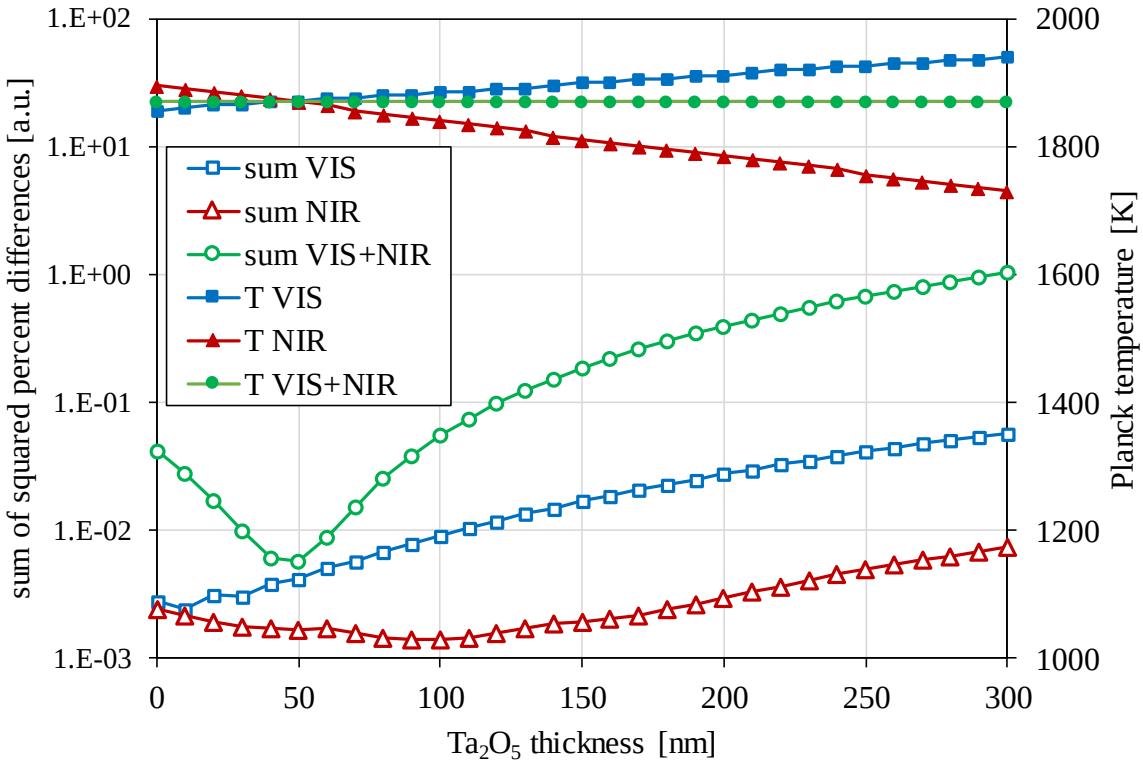

Figure 6.15 Minimal sums of squared percent differences and corresponding temperatures in the wavelength regions VIS, NIR vs. Ta_2O_5 thickness.

In some cases, (in particular when the particle radiation was weak), slightly different temperatures provided the best fits in the VIS and NIR wavelength ranges which were considered upper and lower temperature bounds. The matching Planck emission and the resulting difference to the measured spectrum for the example condition are shown in Figure 6.16.

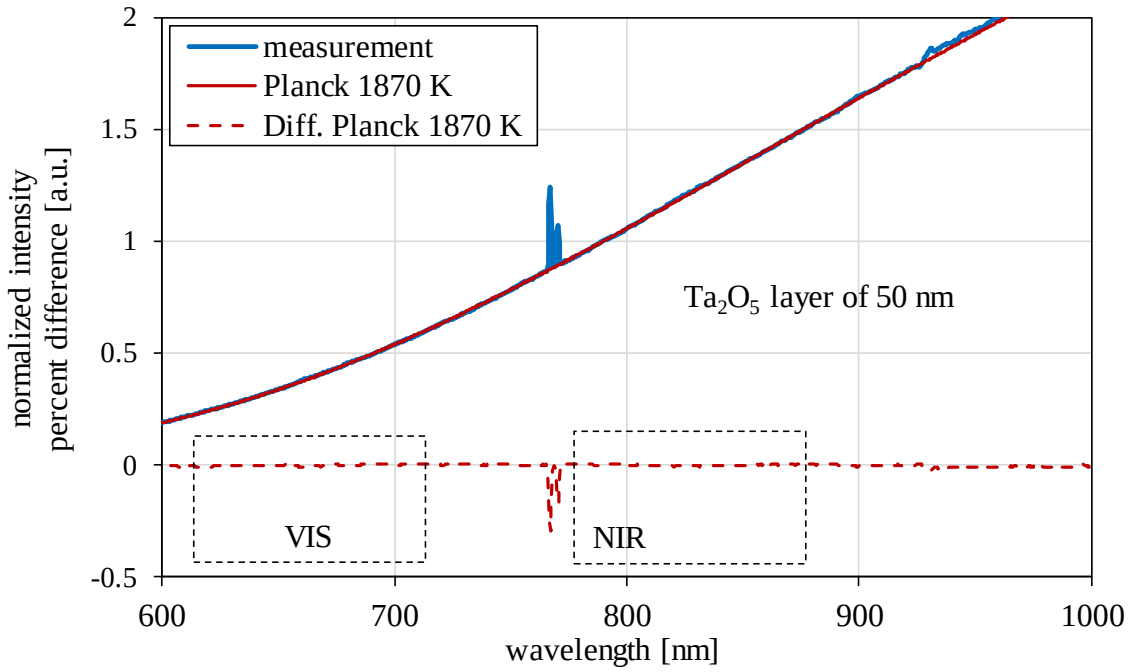

Figure 6.16 Best matching Planck emission for a temperature of 1,870 K and an oxide layer thickness of 50 nm.

6.2.5 Particle temperature distribution

This analysis was performed for all measured flame conditions yielding particle temperature profiles at different distances to the fuel nozzles. Temperature distributions of the TaN particles at different methane/air ratios and locations above the center air/seed nozzles are shown in Figure 6.17 with upper and lower bounds from the temperatures obtained from fitting the VIS and NIR region separately. In

general, the maximum seed particle temperature increased with the fuel flow rate. As anticipated, the highest particle temperatures were attained under the closed flame structures when particles are immersed directly into the flames. Regions of nearly constant high particle temperatures between 1,800 K and 1,930 K were formed. In general, increasing the fuel or air flow rate increased the extent of the high temperature plateau. The largest plateau extended from approximately 2 mm to 12 mm above the fuel nozzles at a fuel flow rate of 50 cm^3/min and air flow rate of 50 cm^3/min. At the lowest fuel flow rate of 20 cm^3/min, particle temperatures never exceeded 1,800 K. Hence, it was possible to create somewhat stable temperature regimes within the flames over extended distances with select air and fuel flow rates. In the high temperature region of the observed flames, oxide layer thicknesses were clearly less than 100 nm for all conditions and positions investigated yielding an average temperature difference of less than 5 K to the temperatures determined without consideration of an oxide layer. The uncertainty of the particle temperature may come from the background emission subtraction and also the signal-to-noise ratios. From the spectra fitting comparison, it was found that the accuracy was approximately $\pm$20 K in the high temperature region, whereas the accuracy is no better than $\pm$150 K in the low temperature region (due to the small signal-to-noise ratio). Only at positions close to the flame tip where particle temperatures decrease again, higher oxide layer thicknesses were obtained. In these regions, however, the detected thermal emission was already weak and higher uncertainties are anticipated. Due to the small thickness of the oxidation layer, the contribution of the oxidation reaction to heating the particles would be very small. The detailed comparisons of shape of microflames with particles emission are shown in Figure 6.18 through Figure 6.23.

The parallel investigation of particle-seeded flow velocity from this burner was also carried out by Hirasawa's group [60]. They found that the particle-seeded flow velocity in the center also depended on the flame structure in a way such that the point to begin increasing central flow velocity moved upstream as fuel flow rate

increased and as flame structure changed. The time during which the seed particles in future synthesis applications are at high temperature can therefore be controlled through a suitable combination of fuel and oxidizer flow rate.

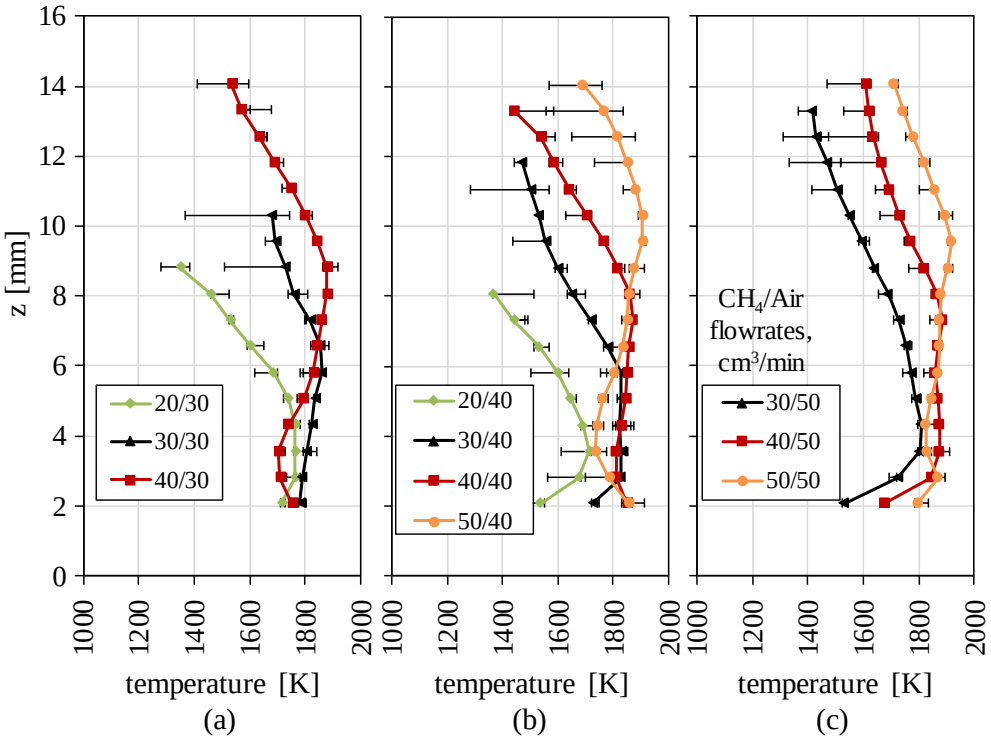

Figure 6.17 Vertical temperature distributions of the TaN particles at different CH_4/Air flowrates for 2.5 mm pitch size burner.

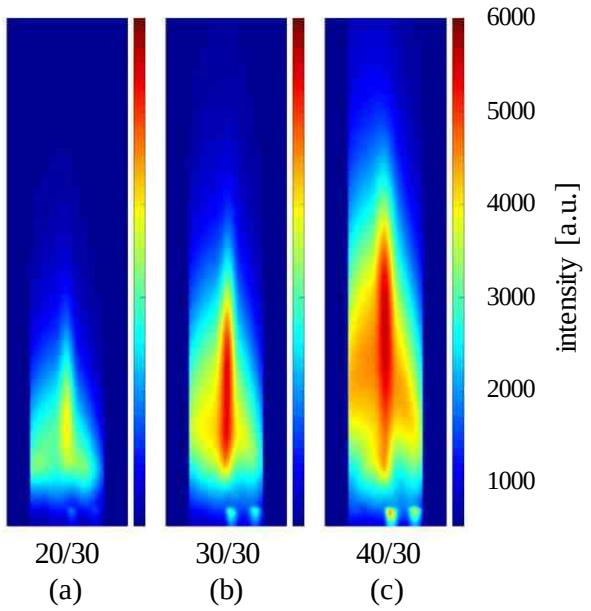

Figure 6.18 Spectrometer image of microflames with particle emission for 2.5 mm pitch size burner at 30 cm^3/min air and varied CH_4 flowrate.

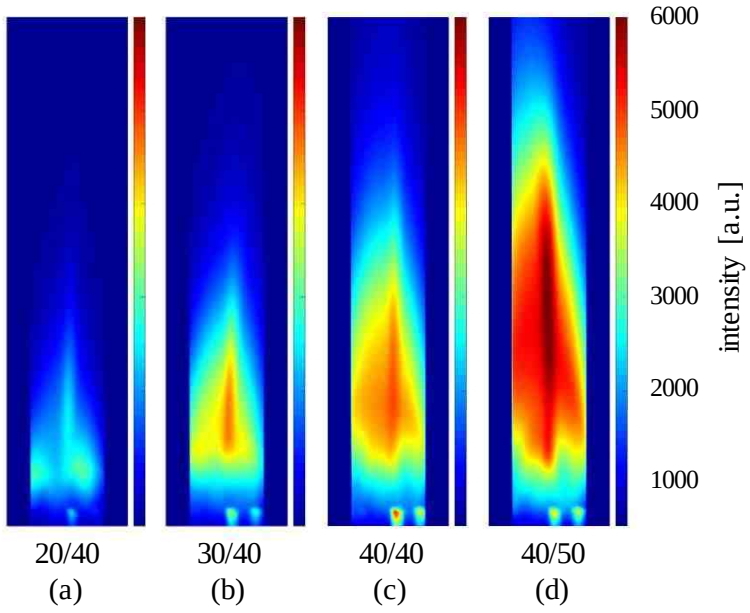

Figure 6.19 Spectrometer image of microflames with particle emission for 2.5 mm pitch size burner at 40 cm^3/min air and varied CH_4 flowrate.

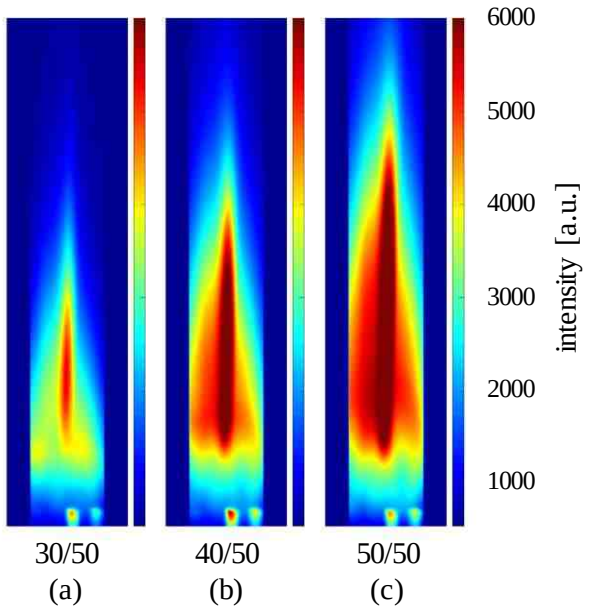

Figure 6.20 Spectrometer image of microflames with particle emission for 2.5 mm pitch size burner at 50 cm^3/min air and varied CH_4 flowrate.

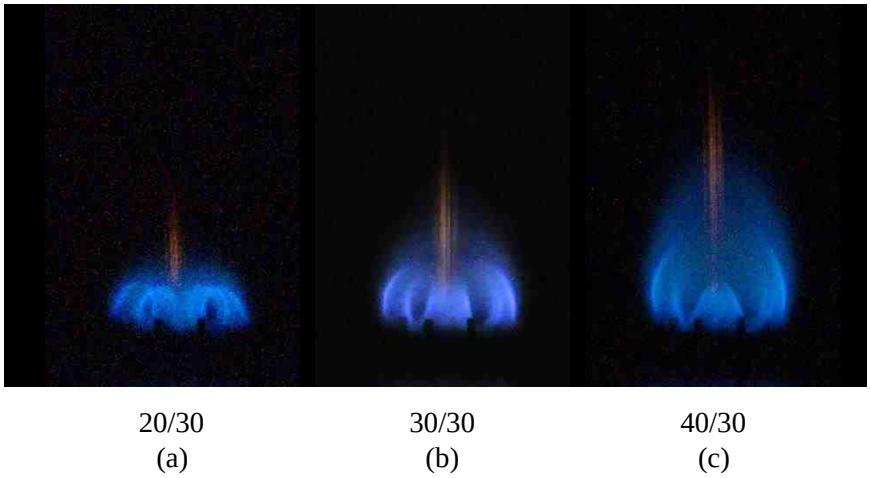

Figure 6.21 DSLR image of microflames with particle emission for 2.5 mm pitch size burner at 30 cm^3/min air and varied CH_4 flowrate.

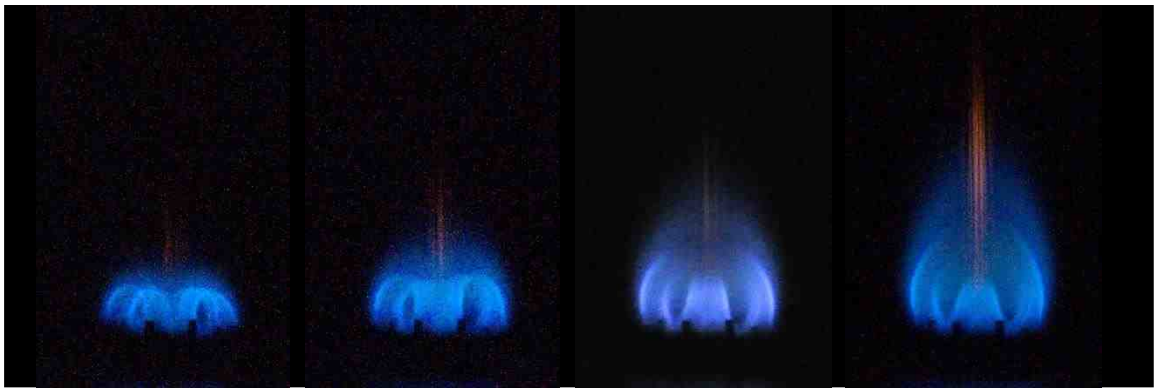

20/40 (a) | 30/40 (b) | 40/40 (c) | 50/40 (d)

Figure 6.22 DSLR image of microflames with particle emission for 2.5 mm pitch size burner at 40 cm^3/min air and varied CH_4 flowrate.

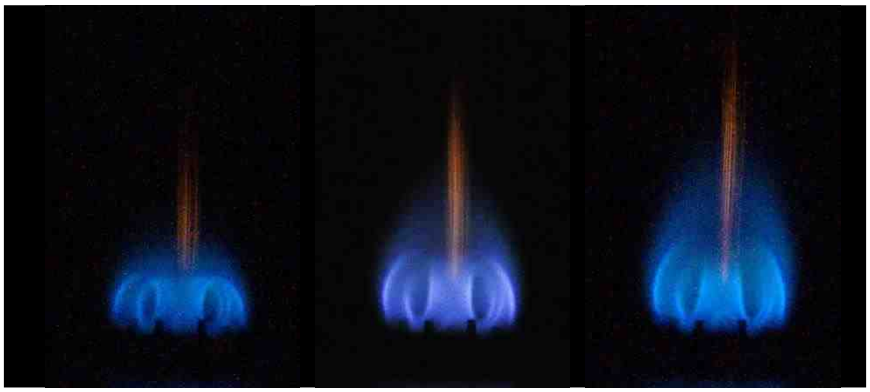

30/50 (a) | 40/50 (b) | 50/50 (c)

Figure 6.23 DSLR image of microflames with particle emission for 2.5 mm pitch size burner at 50 cm^3/min air and varied CH_4 flowrate.

As shown in Figure 6.24, not only the fuel flow rate but also air flow rate increased the extent of the high temperature region. The largest region with peak temperatures higher than 1,900 K formed at flow rates of 50 cm^3/min fuel and reached from 1 mm to 10 mm above the fuel nozzles for 50 cm^3/min air. For equal

flow rates of 50 cm³/min fuel and air, the temperature obtained with a burner pitch size of 2.0 mm is higher than the one with a burner pitch size of 3.0 mm. For flow rates of 40 cm³/min fuel and 30 cm³/min air, the temperature obtained with a pitch size of 2.0 mm is again slightly higher than with 3.0 mm. Furthermore, the extent of the hot zone is smaller with a burner pitch size of 3.0 mm. For flow rates of 40 cm³/min fuel and 50 cm³/min air and 50 cm³/min fuel and 40 cm³/min air, both burner pitch sizes yield a similar temperature distribution. The largest high temperature region is obtained with a burner pitch size of 2.5 mm and a fuel rate of 50 cm³/min. The detailed comparisons of shape of microflames with particles emission are shown in Figure 6.25 through Figure 6.30.

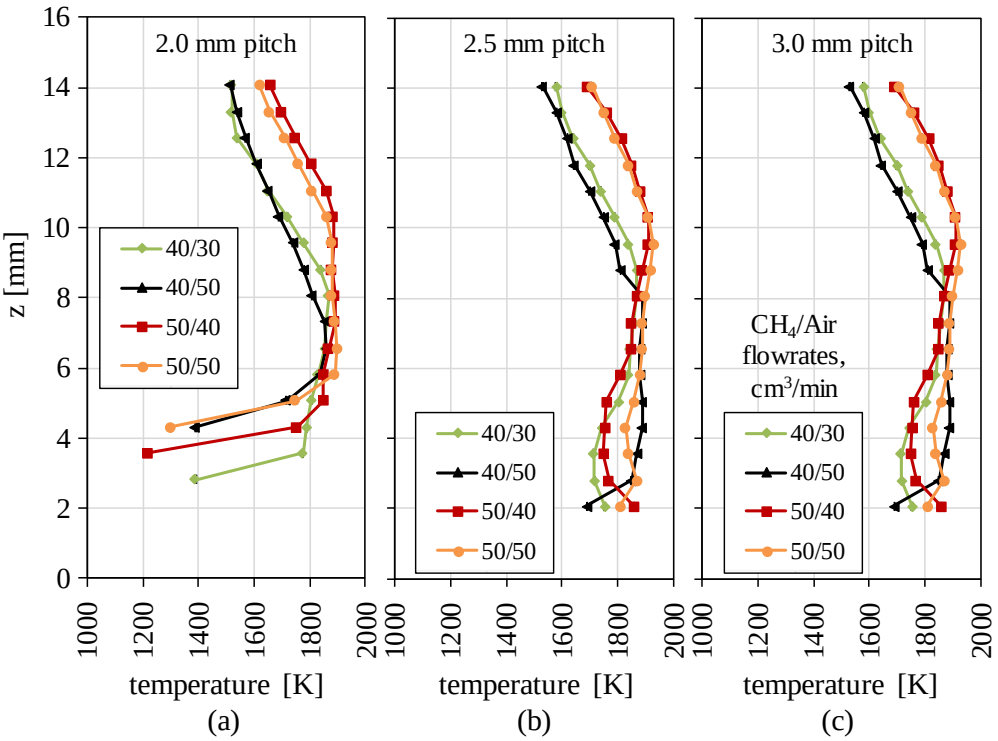

Figure 6.24 Vertical temperature distributions of the TaN particles at selected CH_4/Air flowrates for (a) 2.0 mm, (b) 2.5 mm, and (c) 3.0 mm pitch size burner.

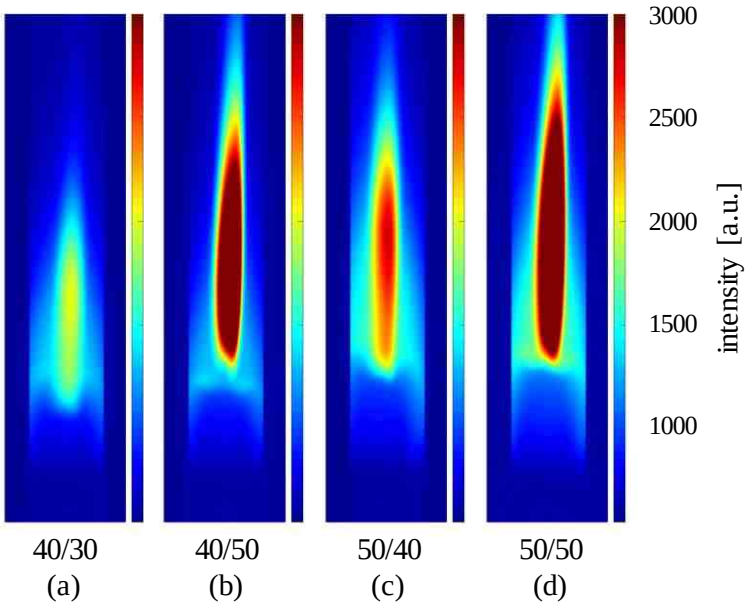

Figure 6.25 Spectrometer image of microflames with particle emission for 2.0 mm pitch size burner at selected CH_4 and air flowrate.

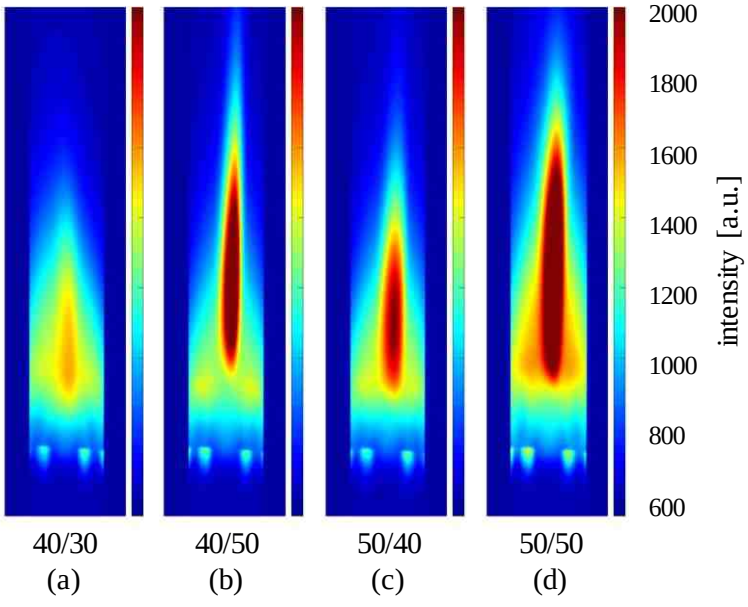

Figure 6.26 Spectrometer image of microflames with particle emission for 2.5 mm pitch size burner at selected CH_4 and air flowrate.

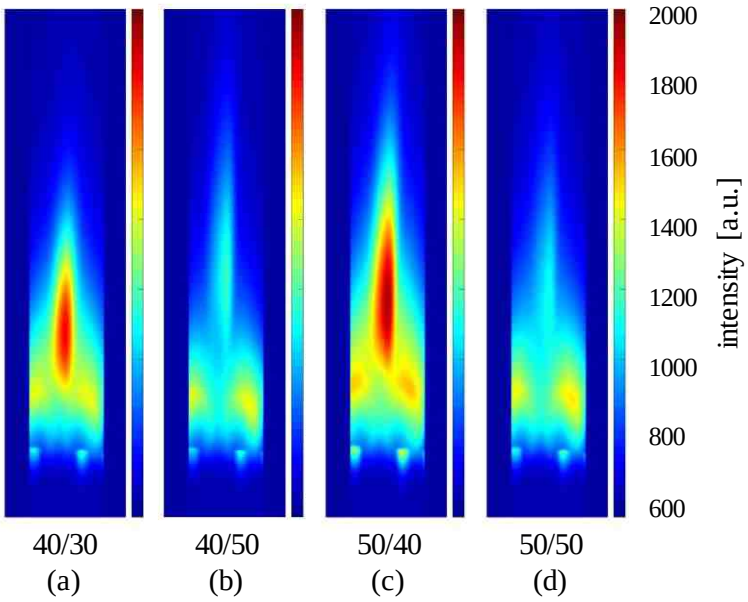

Figure 6.27 Spectrometer image of microflames with particle emission for 3.0 mm pitch size burner at selected CH_4 and air flowrate.

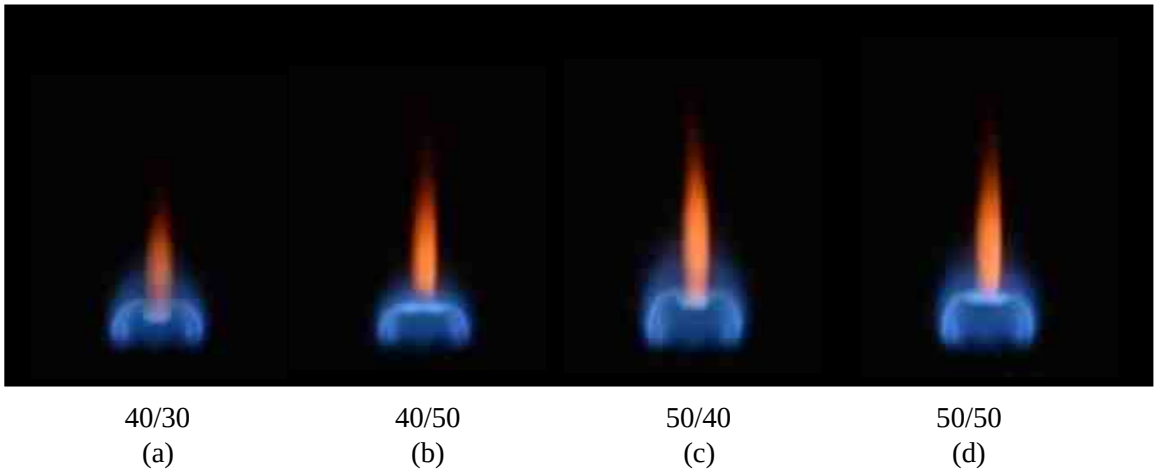

Figure 6.28 DSLR image of microflames with particle emission for 2.0 mm pitch size burner at selected CH_4 and air flowrate.

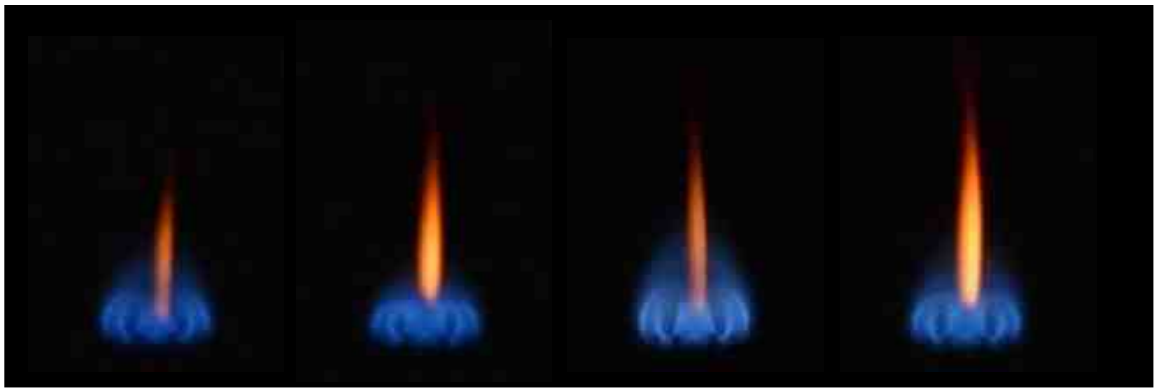

40/30 (a) | 40/50 (b) | 50/40 (c) | 50/50 (d)

Figure 6.29 DSLR image of microflames with particle emission for 2.5 mm pitch size burner at selected CH_4 and air flowrate.

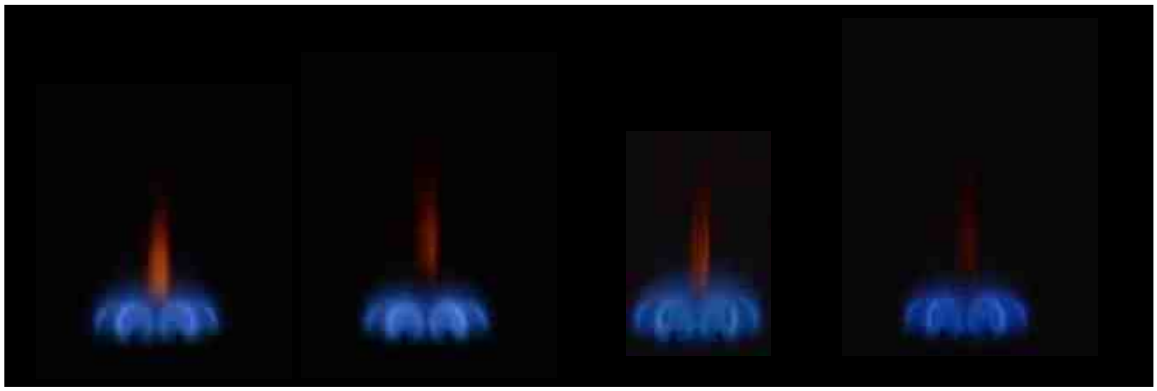

40/30 (a) | 40/50 (b) | 50/40 (c) | 50/50 (d)

Figure 6.30 DSLR image of microflames with particle emission for 3.0 mm pitch size burner at selected CH_4 and air flowrate.

CONCLUSIONS AND FUTURE WORK

7.1 Conclusions

An optical diagnostic technique to characterize complex methane-air diffusion flame for future synthesis applications was developed. Filtered imaging techniques and spectrally resolved measurements were applied to investigate thermal emission of particles and the chemiluminescence of CH^*, C_2^*, and H_2O. Several available spectral simulation codes (LIFBASE, NEQAIR) were used to support the analysis of the molecular emission. The possibility of applying the HITRAN database for analyzing the spectrally resolved H_2O emission was investigated. Accurate prediction of the thermal structure of flames requires detailed information on the radiative properties and a thorough understanding of the governing combustion processes. Three different flame conditions were investigated: an axisymmetric co-flow flame, a merged flame structure created with a microflames burner consisting of six individual microflames, and the microflames with injection of a particle stream into the center of the merged flame structure.

The following conclusions were summarized for the study of chemiluminescence measurement in co-flow flame:

- Abel inversion was applied to the line-of-sight chemiluminescence. Local two-dimensional intensity profiles from both filtered images acquired by DSLR camera and spectrally resolved spectrometer measurement were obtained.
- CH^* and C_2^* emission were generated in a thin flame sheet which thickness was estimated to be 0.25 mm. H_2O emission seemed to come from the same flame sheets and was not detected in the center of the flame. The signals of CH^* and C_2^* emission measurements became too weak at about z = 30 mm, while the signals of water emission decreased slower and became too weak at about z = 42 mm.

- HITRAN simulation results indicated that neither self-absorption nor absorption in room temperature air seem to influence the spectral shape so that the absorption can be excluded from water emission calculation.
- An underlying background emission was found in measured water emission spectra by comparing to simulated spectra at different temperatures. An attempt to determining water temperature was made by comparing modified measured spectra with background emission subtraction to the best fitting simulation spectra. The temperature distribution profiles at selected flame heights were obtained.

The thermal structure of six clustered methane-air microflames surrounding a center nozzle, feeding an airflow which can be seeded with a particle stream, was characterized by emission spectroscopy measurements of C_2^* and CH^* emission produced by chemiluminescence. Although the emission spectroscopy results by the nature of this technique not directly provide spatial resolution along the observed line of sight, a comparison with tomographically analyzed filtered imaging of the CH^* emission allowed for assigning the measured temperatures to the thin flame sheets observed in the filtered imaging work. The combination of the spectroscopic and imaging techniques was found to be a powerful tool for the characterization of 3-D flame structures. The following conclusions were summarized for the study of chemiluminescence measurement in microflames:

- Significant effects of flowrates and burner pitch size on the structure of six clustered methane-air diffusion microflames were observed. The structure of the microflames with a constant methane flowrate of 50 cm^3/min changed significantly as the air flowrate was varied for the 2.0 mm pitch burner, while no change in the structure of microflames was found when the 3.0 mm pitch burner was used. This missing change in flame structure for the 3.0 mm pitch is explained by the larger distance between the air nozzle and the fuel nozzles, which does not allow the center nozzle airflow to influence the methane flow

from the fuel nozzles. Instead, each fuel nozzle tended to establish its own individual microflame.

- Two different pitch sizes, 2.0 and 2.5 mm, the distance between the fuel nozzles to the center air nozzle, were investigated at methane flow rate of 50 cm^3/min, with and without a center air stream of 40 cm^3/min. The integrated emission of the C_2^* and CH^* $\Delta v = 0$ molecular bands from emission spectroscopy and filtered imaging measurements (performed by our collaborators) was used to characterize the active combustion zones in the complex flame structure. The results confirmed thin flame sheets and also showed the merging of the individual microflames for the smaller pitch geometry. The integrated CH^* and C_2^* emission from the spectrally resolved measurements showed very similar structures as seen in the filtered imaging although with reduced spatial resolution and without the option of CT analysis. The results strongly indicate that CH^* and C_2^* are generated in the same region of the flame. The ratio of the C_2^* emission to the CH^* emission from the spectrally resolved measurements was related to the corresponding equivalence ratio using empirical correlations reported by Kojima et al. [50] which were derived from measurements in premixed methane-air flames. As anticipated, the derived equivalence ratios were equal to one in the cases of pure diffusion flames. For a pitch size of 2.0 mm with the center airflow, however, a hat-like flame zone established above the center air nozzle inside the merged flame. Within this region, equivalence ratios between 1 and 1.2 were obtained, suggesting the formation of a fuel-rich flame zone interpreted as a premixed flame.
- CH^* emission was used to characterize the flame front by determining rotational and vibrational temperatures though comparing measured and theoretical spectra simulated with LIFBASE [106]. Rotational temperatures of CH^* were determined from a comparison of the emission of the $\Delta v = 0$ transitions of the CH $A^2\Delta$-$X^2\Pi$ system of electronically excited CH. Spatial

temperature distributions of the microflames were obtained by mapping the 2-D distribution of CH^* rotational and vibrational temperatures, the former one representing the flame temperature. The rotational temperature increased toward the flame tip, from values of about 1,500 K at about 0.75 mm below the fuel nozzle exit (z = - 0.75 mm) to peak values of about 2,450 K at the flame tip at z = 1.5 mm. The vibrational levels of CH were found to be non-thermally distributed since different temperature values were determined from the ratio of $v = 1$ and $v = 2$ to $v = 0$. The vibrational excitation of CH^* is interpreted to be controlled by chemical processes rather than by pure thermal excitation. The spatial distribution of the CH^* emission agreed well with the blue color of the methane-air flame seen in photographic images. The line of sight measurement of CH^* emission is actually the sum of the flame fronts at the measured vertical and horizontal position. The temperature does not correlate directly with the observed intensity but rather is a function of distance to the fuel nozzles exit.

- Through comparison with a spectral line-by-line simulation of the C_2^* emission using the NASA code NEQAIR, rotational and vibrational temperatures of C_2^* were determined throughout the flame structure. As already seen for the chemiluminescence of CH*, the vibrational excitation is most likely generated by the chemical reaction and considered to be not characteristic for the thermal structure of the flame. The rotational temperature, however, typically equilibrates quickly with the translational temperature and is considered a good representation of the gas-dynamic flame temperature. For the investigated flames, rotational temperatures between 1,200 and 1,800 K were derived, mainly depending on the height above the nozzle and showing only slight variation across the merged flame.

In the study of particle emission measurement in microflames, the particle temperatures of micron-size TaN particles with known emissivity injected into a cluster of microflames was investigated. Vertical temperature profiles of TaN

particles along the center axis of the clustered microflames were obtained based on optical emission spectroscopic methods. The temperature dependent spectral emittance of TaN and the effect of a potential Ta_2O_5 layer were taken into account in fitting the spectral shape of the particle radiation through Planck emission. The following summarizes the results of this study:

- Both transmittance measurements and theoretical calculation showed that the flame seeded with TaN particles of several micron diameter was optically thin and that scattering and absorption effects were negligible.
- A region of high and almost constant temperature was detected, it extended well beyond the actual flame front and its extent increased with fuel and oxidizer flow rate.
- The pitch size of the burner influences the temperature distribution at selected flow rates. The most extended regions of high temperature were obtained with a burner pitch size of 2.5 mm. With increased burner pitch size, operation with small fuel/air flow rate ratios becomes less favorable.
- By XPS analyses of flame seeded TaN, the particles were found to be coated with thin Ta_2O_5 layer after passing through the flame. The oxide layer thickness was estimated by including the Ta_2O_5 transmission in the spectral fitting process. In the high temperature regions of the flames, the Ta_2O_5 layer thickness was found to be clearly below 100 nm. In comparison to fitting without an oxide layer, the influence on the resulting temperatures was within the temperature increment of 5 K.

7.2 Future Work

The chemiluminescence of CH^* and C_2^* characterizes the flame structure in terms of flame front and the combustion process. The rotational temperature of these molecules characterizes the flame temperature. Combined spectral filtered image analysis has been proven a useful tool for flame diagnostics. Injection of particles

into the merged microflames structure generates constant plateaus of high temperature useful for future flame synthesis, the extent of these plateaus being controlled by flow rates and burner pitch. Oxidation layer formation and particle temperatures can be captured through the emission spectroscopic methods demonstrated in this work. The results obtained in this study are intended to be used for the definition of working conditions for future flame synthesis processes to be investigated with this burner design, and for validation of numerical codes currently under development.

Future work could involve measurements in horizontal planes at different vertical positions above the nozzles enabling a spatial reconstruction of these horizontal profiles from the line-integrated emission spectroscopy data to more concretely interpret beneficial approaches to reaction chemistry within controlled flames. In addition, the temperature profiles of particles and molecules should be paired with measured velocity profiles in future studies to obtain the temporal variation of particle temperatures which is one of key control factor for flame synthesis of possibly unusual particle chemistry. For future experiments to characterize the flame structure, it might, however, be beneficial to use particle materials which do not undergo such oxidation reactions, such as TaC or TiC, with a controllable feeding rate. Also, investigation of premixed flames, and sooting flames will be beneficial for obtaining more working envelops for flame synthesis.

Appendix

MATLAB code used to perform angle tilting correction:

```
%Process Imported Data
fclose('all'), clear all, clc, close all

load('H:\Diao_64GB\Matlab_Working_Folder\Matlab_CoFlow_2018-05-
17\Matlab\Spec\wavelength_c_9569\Data_Imported.mat')

%% Substitute variables!

Flame = c_z_5; % flame height of interest

BG = c_BG_60sec; % background

%% Spectra
%frames averaged
m_BG = mean(BG, 3);
m_Flame = mean(Flame, 3);

%BG Corrected
m_Flame_BG_corr = m_Flame - m_BG;

%no negative
m_Flame_BG_corr (m_Flame_BG_corr <0.0001)= 0.0001;

%Time Corrected (check TIME)
ExpTime = double(headc_BG_60sec.exp_sec);
m_Flame_BG_Time_corr = m_Flame_BG_corr/ExpTime;

%Intensity
load ('H:\Diao_64GB\Matlab_Working_Folder\Matlab_CoFlow_2018-05-
17\Matlab\Calibraion\Intensity\CorrectionFactor_c.mat')

m_Flame_BG_Time_Int_corr = m_Flame_BG_Time_corr.*CorrectionFactor;
%transpose
m_BG = m_BG';
m_Flame=m_Flame';
m_Flame_BG_Time_Int_corr = m_Flame_BG_Time_Int_corr';
```

```
save('Data_Corrected.mat','x','y','wavelength_c','ExpTime','m_BG','m_Flame','m_
Flame_BG_Time_Int_corr')
```

```
%Differentiate values to more strips
fclose('all'), clear all, clc, close all

load('Data_Corrected')

y_new = [1:size(y,2)/408:size(y,2)];

for i=1:1340
   m_Flame_BG_Time_Int_corr_400 (i,:) =
interp1(y,m_Flame_BG_Time_Int_corr(i,:),y_new);
   i+i+1;
end
sum_m_Flame_BG_Time_Int_corr = sum (m_Flame_BG_Time_Int_corr,2);
sum_m_Flame_BG_Time_Int_corr_400 =
sum(m_Flame_BG_Time_Int_corr_400,2);

factor =
sum_m_Flame_BG_Time_Int_corr./sum_m_Flame_BG_Time_Int_corr_400;

for i=1:400
   m_Flame_BG_Time_Int_corr_400_new(:,i) =
m_Flame_BG_Time_Int_corr_400(:,i).*factor;
   i=i+1;
end

save
('Data_Corrected_Interpolated.mat','x','y','wavelength_c','y_new','m_Flame_BG_
Time_Int_corr_400_new')

%Angle Correction
fclose('all'), clear all, clc, close all

load('Data_Corrected_Interpolated')

m_Flame_BG_Time_Int_corr_400_new =
m_Flame_BG_Time_Int_corr_400_new';

tform=maketform('affine',[1 .013 0; 0 1 0; 0 0 1]);
```

```
m_Flame_BG_Time_Int_Ang_corr_400_new
=imtransform(m_Flame_BG_Time_Int_corr_400_new,tform);m_Flame_BG_Tim
e_Int_corr_400_new(m_Flame_BG_Time_Int_corr_400_new<0.01)=0.01;

%truncation
m_Flame_BG_Time_Int_Ang_corr_400_new_truncated =
m_Flame_BG_Time_Int_Ang_corr_400_new ([10:409],:);

%dimension reform
bins = 8;

for i=1:1340
   B = reshape
(m_Flame_BG_Time_Int_Ang_corr_400_new_truncated(:,i),bins,400/bins);
   m_Flame_BG_Time_Int_Ang_corr (i,:) = sum(B);
i=i+1;
end

save
('Data_Corrected_Angle_Corr.mat','x','y','wavelength_c','m_Flame_BG_Time_Int
_Ang_corr')
%% write to excel
filename = 'Hitran_300l_mm_c.xlsx';
xlswrite(filename,m_Flame_BG_Time_Int_Ang_corr,'Flame_corr','l8:bi1347')
```

MATLAB code used to create Abel matrix by courtesy of Helmut Koch [112]

```
%Abel Inversion
%This script should be used to apply Abel Inversion to a measured spectra
fclose('all'), clear all, clc, close all

load('Data_Corr_ROI')

NumAbel = 21;    %Number of radial profiles

Offset = 0.34/1000;     %[m] width of on estrip

%Allocate Array for saving the fraction of the line of sight.
%Definition!! First row contains the line of sight at the center line,
%last row at outer circle.
```

```
AbelMatrix = zeros(NumAbel);

EndCol = NumAbel;

for i=1:NumAbel
   k = i;
   SumAbel = 0;
   for j=EndCol:-1:1
      AbelMatrix(i,j) = sqrt((k*Offset)^2-((i-1)*Offset)^2)*2 - SumAbel;
      SumAbel = SumAbel + AbelMatrix(i,j);
      k = k + 1;
   end
   EndCol = EndCol - 1;
end

AbelMatInv = AbelMatrix';

save ('Abel_Matrix','AbelMatrix','AbelMatInv')
```

MATLAB code used to apply Abel matrix to the measured spectra

```
fclose('all'), clear all, clc, close all

load('Abel_Matrix')

load('H:\Diao_64GB\Matlab_Working_Folder\Matlab_CoFlow_2018-05-
17\Matlab\Spec\wavelength_c_9569\c_z_5_selected\Data_Corrected_Angle_Cor
r')

LL = AbelMatrix;
LL_flipped = flip (LL);

% Matrix A X = B;       (A^-1) A X = (A^-1) B;      X = (A^-1) B;
% epsilon = zeros (n,1)+1;  I_measured_flipped = LL_flipped * epsilon  ;

strip_center =21;
width = 20;

data    =    m_Flame_BG_Time_Int_Ang_corr (:,[strip_center-
width:strip_center+width]);

for n = 1:size(data,3)
```

```
   for dim_NOT_Inv = 1:size(data,1)

I_measured_right = data (dim_NOT_Inv,[(size(data,2)+1)/2:size(data,2)],n); %
replace with new spec matrix

I_measured_left = data (dim_NOT_Inv,[1:(size(data,2)+1)/2],n);

I_measured_right = I_measured_right';

I_measured_conv_right = double(I_measured_right);

I_measured_flipped_right = flip (I_measured_conv_right);

epsilon_right(:,dim_NOT_Inv,n) = inv(LL_flipped) * I_measured_flipped_right;

I_measured_left = I_measured_left';

I_measured_conv_left = double(I_measured_left);

epsilon_left(:,dim_NOT_Inv,n) = inv(LL_flipped) * I_measured_conv_left;

dim_NOT_Inv= dim_NOT_Inv+1;
   end

epsilon_right (:,:,n) = flip (epsilon_right(:,:,n));

n=n+1

end

epsilon = epsilon_left;

epsilon ([size(epsilon_left,1):((size(epsilon_left,1)*2)-1)],:) = epsilon_right;

epsilon_modi = epsilon_left([1:size(epsilon_left,1)-1],:);

epsilon_modi (size(epsilon_left,1),:) = (epsilon_right(2,:)+
epsilon_modi(size(epsilon_left,1)-1,:))/2;

epsilon_modi ([size(epsilon_left,1)+1:size(epsilon,1)],:) = epsilon_right([2:end],:);

epsilon = epsilon';

epsilon_modi = epsilon_modi';
```

```
save ('epsilon.mat','data','epsilon','epsilon_modi','wavelength_c')
```

MATLAB code used to extract DSLR RAW file from [97] and by courtesy of Ricky Green [113]

```
function [r,g,b,ET,r_max,g_max,b_max] = rawRGBgen(startimage, endimage)

n = 1;   %counter

for i = startimage:endimage
   newi = int2str(i);
   warning off MATLAB:tifflib:TIFFReadDirectory:libraryWarning
   t = Tiff((strcat('DSC_',newi,'.DNG')),'r');
   offsets = getTag(t,'SubIFD');
   setSubDirectory(t,offsets(1));
   raw = read(t);                                % Create variable 'raw', the Bayer
CFA data
   close(t);

   meta_info = imfinfo((strcat('DSC_',newi,'.DNG')));                    % Crop
to only valid pixels
   x_origin = meta_info.SubIFDs{1}.ActiveArea(2)+1;          % +1 due to
MATLAB indexing
   width = meta_info.SubIFDs{1}.DefaultCropSize(1);
   y_origin = meta_info.SubIFDs{1}.ActiveArea(1)+1;
   height = meta_info.SubIFDs{1}.DefaultCropSize(2);

   raw = double(raw(y_origin:y_origin+height-1,x_origin:x_origin+width-1));

%Demosaicing
   temp = uint16(raw);
   rgb = double(demosaic(temp,'rggb'));

   red_RAW = rgb(:,:,1);
   green_RAW = rgb(:,:,2);
   blue_RAW = rgb(:,:,3);

   red_RAW = flip(red_RAW);
   green_RAW = flip(green_RAW);
   blue_RAW = flip(blue_RAW);
```

```
   Exposure_Time (n,:)= meta_info.DigitalCamera.ExposureTime;

   red_max (n) = max(max(red_RAW ));
   green_max (n) = max(max(green_RAW ));
   blue_max (n) = max(max(blue_RAW ));
%    blue_min (n) = min(min(blue_RAW ));

   red_All_RAW (:,:,n)     = red_RAW;
   green_All_RAW (:,:,n)   = green_RAW;
   blue_All_RAW (:,:,n)    = blue_RAW;

   i = i + 1
   n = n+1;
end

r = red_All_RAW;
g = green_All_RAW;
b = blue_All_RAW;
ET = Exposure_Time;
r_max = red_max;
g_max = green_max;
b_max = blue_max;

end

% Y = [1:4016];
% X = [1:6016];
save ('epsilon.mat','data','epsilon','epsilon_modi','wavelength_c')
```

```
fclose('all'), clear all, clc, close all

i_start = 4883;
i_end = 4930;

b_all_max_Flame = zeros(i_end-i_start+1,1);
Eexposure_Time_all_Flame = b_all_max_Flame;

for i = i_start:i_end
[r,g,b,ET,r_max,g_max,b_max] = rawRGBgen(i,i); %call rawRGBgen function

save(sprintf('%1.5fsec_Flame.mat',ET(1,:)),'r','g','b','ET','r_max','g_max','b_max' )
```

```
  j = i - i_start + 1;

b_all_max_Flame          (j,:)   = b_max;
Eexposure_Time_all_Flame  (j,:)   = ET;

save('Data_Stitched_Flame','b_all_max_Flame','Eexposure_Time_all_Flame')

i=i+1

end
```

References

[1] S.E. Pratsinis, P.T. Spicer, Competition between gas phase and surface oxidation of $TiCl_4$ during synthesis of TiO2 particles, Chemical Engineering Science, 53 (1998) 1861-1868.

[2] S.H. Ehrman, S.K. Friedlander, M.R. Zachariah, Characteristics of SiO_2/TiO_2 nanocomposite particles formed in a premixed flat flame, Journal of Aerosol Science, 29 (1998) 687-706.

[3] H.K. Kammler, S.E. Pratsinis, P.W. Morrison, B. Hemmerling, Flame temperature measurements during electrically assisted aerosol synthesis of nanoparticles, Combustion and Flame, 128 (2002) 369-381.

[4] O.I. Arabi–Katbi, S.E. Pratsinis, P.W. Morrison, C.M. Megaridis, Monitoring the flame synthesis of TiO_2 particles by in-situ FTIR spectroscopy and thermophoretic sampling, Combustion and Flame, 124 (2001) 560-572.

[5] S. Tsantilis, H.K. Kammler, S.E. Pratsinis, Population balance modeling of flame synthesis of titania nanoparticles, Chemical Engineering Science, 57 (2002) 2139-2156.

[6] Z. Sun, R.L. Axelbaum, B.H. Chao, A multicomponent sectional model applied to flame synthesis of nanoparticles, Proceedings of the Combustion Institute, 29 (2002) 1063-1069.

[7] T. Johannessen, J.R. Jensen, M. Mosleh, J. Johansen, U. Quaade, H. Livbjerg, Flame Synthesis of Nanoparticles, Chemical Engineering Research and Design, 82 1444-1452.

[8] H.K. Kammler, L. Mädler, S.E. Pratsinis, Flame Synthesis of Nanoparticles, Chemical Engineering & Technology, 24 (2001) 583-596.

[9] T.X. Li, K. Kuwana, K. Saito, H. Zhang, Z. Chen, Temperature and carbon source effects on methane–air flame synthesis of CNTs, Proceedings of the Combustion Institute, 32 (2009) 1855-1861.

[10] L. Yuan, K. Saito, C. Pan, F.A. Williams, A.S. Gordon, Nanotubes from methane flames, Chemical Physics Letters, 340 (2001) 237-241.

[11] W. Merchan-Merchan, A.V. Saveliev, L. Kennedy, W.C. Jimenez, Combustion synthesis of carbon nanotubes and related nanostructures, Progress in Energy and Combustion Science, 36 (2010) 696-727.

[12] M.J. Height, J.B. Howard, J.W. Tester, J.B. Vander Sande, Flame synthesis of single-walled carbon nanotubes, Carbon, 42 (2004) 2295-2307.

[13] R.L. Vander Wal, T.M. Ticich, Flame and Furnace Synthesis of Single-Walled and Multi-Walled Carbon Nanotubes and Nanofibers, The Journal of Physical Chemistry B, 105 (2001) 10249-10256.

[14] M.T. Swihart, Vapor-phase synthesis of nanoparticles, Current Opinion in Colloid & Interface Science, 8 (2003) 127-133.

[15] T.X. Li, H.G. Zhang, F.J. Wang, Z. Chen, K. Saito, Synthesis of carbon nanotubes on Ni-alloy and Si-substrates using counterflow methane–air diffusion flames, Proceedings of the Combustion Institute, 31 (2007) 1849-1856.

[16] L.A. Kennedy, Carbon nanotubes, synthesis, growth and orientation control in opposed flow diffusion flames, Journal of Heat Transfer, 130 (2008) 042402.

[17] K. Kuwana, H. Endo, K. Saito, D. Qian, R. Andrews, E.A. Grulke, Catalyst deactivation in CVD synthesis of carbon nanotubes, Carbon, 43 (2005) 253-260.

[18] K. Kuwana, K. Saito, Modeling CVD synthesis of carbon nanotubes: Nanoparticle formation from ferrocene, Carbon, 43 (2005) 2088-2095.

[19] K. Saito, F.A. Williams, A.S. Gordon, Structure of Laminar Coflow Methane–Air Diffusion Flames, Journal of Heat Transfer, 108 (1986) 640-648.

[20] K. Saito, F.A. Williams, A.S. Gordon, A Study of the Two-Color Soot Zone for Small Hydrocarbon Diffusion Flames, Combustion Science and Technology, 51 (1987) 285-305.

[21] K. Saito, A.S. Gordon, F.A. Williams, W.F. Stickle, A Study of the Early History of Soot Formation in Various Hydrocarbon Diffusion Flames, Combustion Science and Technology, 80 (1991) 103-119.

[22] R.L. Vander Wal, L.J. Hall, G.M. Berger, Optimization of flame synthesis for carbon nanotubes using supported catalyst, The Journal of Physical Chemistry B, 106 (2002) 13122-13132.

[23] S. Yang, Y.-H. Jang, C.H. Kim, C. Hwang, J. Lee, S. Chae, S. Jung, M. Choi, A flame metal combustion method for production of nanoparticles, Powder Technology, 197 (2010) 170-176.

[24] S.P. Burke, T.E.W. Schumann, Diffusion Flames, Industrial & Engineering Chemistry, 20 (1928) 998-1004.

[25] M.D. Smooke, P. Lin, J.K. Lam, M.B. Long, Computational and experimental study of a laminar axisymmetric methane-air diffusion flame, Symposium (International) on Combustion, 23 (1991) 575-582.

[26] K.T. Walsh, M.B. Long, M.A. Tanoff, M.D. Smooke, Experimental and computational study of CH, CH^*, and OH^* in an axisymmetric laminar diffusion flame, Symposium (International) on Combustion, 27 (1998) 615-623.

[27] S. Dworkin, B.C. Connelly, A.M. Schaffer, B.A.V. Bennett, M. Long, M.D. Smooke, M.P. Puccio, B. McAndrews, J.H. Miller, Computational and experimental study of a forced, time-dependent, methane–air coflow diffusion flame, 2007.

[28] D. Giassi, S. Cao, B.A.V. Bennett, D.P. Stocker, F. Takahashi, M.D. Smooke, M.B. Long, Analysis of CH^* concentration and flame heat release rate in laminar coflow

diffusion flames under microgravity and normal gravity, Combustion and Flame, 167 (2016) 198-206.

[29] H. Ban, S. Venkatesh, K. Saito, Convection-Diffusion Controlled Laminar Micro Flames, Journal of Heat Transfer, 116 (1994) 954-959.

[30] M. Fuchihata, T. Ida, K. Kuwana, S. Mizuno, A Study about Flame Structure of Premixed Microflame, NCTAM papers, National Congress of Theoretical and Applied Mechanics, Japan, 62 (2013) 219.

[31] Y. Nakamura, H. Ban, K. Saito, T. Takeno, Structure of Micro (Millimeter Size) Diffusion Flames, in: K. Saito (Ed.) Progress in Scale Modeling: Summary of the First International Symposium on Scale Modeling (ISSM I in 1988) and Selected Papers from Subsequent Symposia (ISSM II in 1997 through ISSM V in 2006), Springer Netherlands, Dordrecht, 2008, pp. 293-306.

[32] T. Hirasawa, K. Gotanda, H. Masuda, Y. Nakamura, Impact of Flame–Flame Interactions in Identical Twin Diffusion Microflames, Combustion Science and Technology, 184 (2012) 1651-1663.

[33] Z. Diao, M. Winter, T. Hirasawa, K. Saito, Characterization of Microflame Burner Designs Seeded with TaN Particles through Emission Spectroscopy, in: 10th U. S. National Combustion Meeting, College Park, Maryland, April 23-26, 2017.

[34] Z. Diao, M. Winter, T. Hirasawa, K. Saito, Characterization of the thermal structure of six clustered microflames seeded with TaN particles through emission spectroscopy, Experimental Thermal and Fluid Science, 96 (2018) 295-302.

[35] Y. Ishino, N. Hayashi, I.F. Bt Abd Razak, T. Kato, Y. Kurimoto, Y. Saiki, 3D-CT(Computer Tomography) Measurement of an Instantaneous Density Distribution of Turbulent Flames with a Multi-Directional Quantitative Schlieren Camera (Reconstructions of High-Speed Premixed Burner Flames with Different Flow Velocities), Flow, Turbulence and Combustion, 96 (2016) 819-835.

[36] A.A. Salaimeh, T. Hirasawa, M. Fuchihata, N. Akafuah, K. Saito, Thermal and Flow Structures of a Porous Burner Flame and an Array of Micro Flame Burners: Implications to Simulate Large Scale Mass Fires and Fire Whirls in Laboratory, in: 10th U. S. National Combustion Meeting, College Park, Maryland, April 23-26, 2017.

[37] R.I. Emori, K. Saito, K. Sekimoto, Scale Models in Engineering (Mokei Jikken no Riron to Ohyou), Third ed., Gihodo Publishing Co., Tokyo, Japan, 2000.

[38] F.M. White, Fluid Mechanics, 4th ed., McGraw-Hill, 1999.

[39] T. Hirasawa, N. Sato, Y. Nakamura, Exhaust Gas Characteristics of Methane Clustered Microflames Established on 3 x 3 Array of Micro Burners, Journal of the Japanese Society for Experimental Mechanics, 14 (2014) s67-s70.

[40] K. Kuwana, S. Kato, A. Kosugi, T. Hirasawa, Y. Nakamura, Interaction of Two Micro-slot Flames: Heat Release Rate and Flame Shape, Journal of Physics: Conference Series, 557 (2014) 012079.

[41] Y. Han, Y. Liu, M. Li, J. Huang, A review of development of micro-channel heat exchanger applied in air-conditioning system, Energy Procedia, 14 (2012) 148-153.

[42] A.G. Gaydon, Measurements of Effective Temperature and Studies with Special Sources, in: The Spectroscopy of Flames, Springer Netherlands, Dordrecht, 1974, pp. 182-220.

[43] V.N. Nori, J.M. Seitzman, CH^* chemiluminescence modeling for combustion diagnostics, Proceedings of the Combustion Institute, 32 (2009) 895-903.

[44] A.G. Gaydon, The Spectra of Organic Flames, in: The Spectroscopy of Flames, Springer Netherlands, Dordrecht, 1974, pp. 144-181.

[45] Y. Jin, Y. Song, X. Qu, Z. Li, Y. Ji, A. He, Three-dimensional dynamic measurements of CH^* and C_2^* concentrations in flame using simultaneous chemiluminescence tomography, Optics express, 25 (2017) 4640-4654.

[46] K. Kitagawa, T. Ito, T. Sakai, CO_2 Plasma Arc Heating Test in C/C Composite Penetrated with Silicone Oil, Transactions of the Japan Society for Aeronautical and Space Science, 12 (2014) 51-55.

[47] M. Winter, B. Butler, P.M. Danehy, S. Splinter, Z. Diao, F. Panerai, A. Martin, S. Bailey, Characterization of Ablation Product Radiation Signatures of PICA and FiberForm, in: 46th AIAA Thermophysics Conference, American Institute of Aeronautics and Astronautics, 2016.

[48] C.S. Panoutsos, Y. Hardalupas, A.M.K.P. Taylor, Numerical evaluation of equivalence ratio measurement using OH^* and CH^* chemiluminescence in premixed and non-premixed methane–air flames, Combustion and Flame, 156 (2009) 273-291.

[49] M. Winter, C. Srinivasan, R. Charnigo, D.K. Prabhu, Spectroscopic Analysis of Nonequilibrium Excited State Chemistry in a NASA Arc Jet, accepted for publication the AIAA Journal of Thermophysics and Heat Transfer, (January 2018).

[50] J. Kojima, Y. Ikeda, T. Nakajima, Spatially resolved measurement of OH^*, CH^*, and C_2^* chemiluminescence in the reaction zone of laminar methane/air premixed flames, Proceedings of the Combustion Institute, 28 (2000) 1757-1764.

[51] J. Kojima, Y. Ikeda, T. Nakajima, Basic aspects of OH(A), CH(A), and C_2(d) chemiluminescence in the reaction zone of laminar methane–air premixed flames, Combustion and Flame, 140 (2005) 34-45.

[52] B. Higgins, M.Q. McQuay, F. Lacas, S. Candel, An experimental study on the effect of pressure and strain rate on CH chemiluminescence of premixed fuel-lean methane/air flames, Fuel, 80 (2001) 1583-1591.

[53] A. Hossain, Y. Nakamura, A numerical study on the ability to predict the heat release rate using CH^* chemiluminescence in non-sooting counterflow diffusion flames, Combustion and Flame, 161 (2014) 162-172.

[54] K. Saito, Chapter 2 - Flames, in: E.A. Johnson, K. Miyanishi (Eds.) Forest fires: Behavior and ecological effects, Academic Press, San Diego, 2001, pp. 11-54.

[55] W. Meier, C. Dem, C.M. Arndt, Mixing and reaction progress in a confined swirl flame undergoing thermo-acoustic oscillations studied with laser Raman scattering, Experimental Thermal and Fluid Science, 73 (2016) 71-78.

[56] J. Kiefer, M.C. Weikl, T. Seeger, F. von Issendorff, F. Beyrau, A. Leipertz, Non-intrusive gas-phase temperature measurements inside a porous burner using dual-pump CARS, Proceedings of the Combustion Institute, 32 (2009) 3123-3129.

[57] F. Vestin, D. Sedarsky, R. Collin, M. Aldén, M. Linne, P.-E. Bengtsson, Rotational coherent anti-Stokes Raman spectroscopy (CARS) applied to thermometry in high-pressure hydrocarbon flames, Combustion and Flame, 154 (2008) 143-152.

[58] R.J. Hall, P.A. Bonczyk, Sooting flame thermometry using emission/absorption tomography, Applied optics, 29 (1990) 4590-4598.

[59] D.P. Correia, P. FerrÃO, A. Caldeira-Pires, Advanced 3D Emission Tomography Flame Temperature Sensor, Combustion Science and Technology, 163 (2001) 1-24.

[60] Y. Kato, T. Hirasawa, Z. Diao, M. Winter, Y. Ishino, Three-Dimensional Flame Structure and Characteristics of Heating Particles in Methane Clustered Microflames on Six Fuel and One Air Jets, in: Proceedings of the Annual Conference of the Japan Institute of Energy, Nagoya, Japan, Aug. 1-2, 2017.

[61] P.E. Best, P.L. Chien, R.M. Carangelo, P.R. Solomon, M. Danchak, I. Ilovici, Tomographic reconstruction of FT-IR emission and transmission spectra in a sooting laminar diffusion flame: Species concentrations and temperatures, Combustion and Flame, 85 (1991) 309-318.

[62] P.E. Best, R.M. Carangelo, J.R. Markham, P.R. Solomon, Extension of emission-transmission technique to particulate samples using FT-IR, Combustion and Flame, 66 (1986) 47-66.

[63] L.G. Blevins, M.W. Renfro, K.H. Lyle, N.M. Laurendeau, J.P. Gore, Experimental study of temperature and CH radical location in partially premixed CH_4/air coflow flames, Combustion and Flame, 118 (1999) 684-696.

[64] F.A. Williams, Combustion Theory, 2nd ed., Benjamin Cummings, California, 1985.

[65] A. Linan, F.A. Williams, Fundamental aspects of combustion, New York, NY (United States); Oxford University Press, United States, 1993.

[66] W.B. Jensen, The Origin of the Bunsen Burner, Journal of Chemical Education, 82 (2005) 518.

[67] I. Glassman, R.A. Yetter, Chapter 6 - Diffusion Flames, in: I. Glassman, R.A. Yetter (Eds.) Combustion (Fourth Edition), Academic Press, Burlington, 2008, pp. 311-377.

[68] M.F. Modest, CHAPTER 1 - FUNDAMENTALS OF THERMAL RADIATION, in: M.F. Modest (Ed.) Radiative Heat Transfer, Academic Press, Burlington, 2003, pp. 1-29.

[69] J. Howell, R. Siegel, M.P. Mengüç, Thermal Radiation Heat Transfer, 2010.

[70] M.F. Modest, CHAPTER 11 - RADIATIVE PROPERTIES OF PARTICULATE MEDIA, in: M.F. Modest (Ed.) Radiative Heat Transfer (Second Edition), Academic Press, Burlington, 2003, pp. 361-412.

[71] C.L. Tien, B.L. Drolen, Thermal radiation in particulate media with dependent and independent scattering, in: Annual Review of Numerical Fluid Mechanics and Heat Transfer, vol. 1, Hemisephere, New York, pp. 1-32, 1987.

[72] H.C.v.d. Hulst, Light scattering by small particles, Quarterly Journal of the Royal Meteorological Society, 84 (1958) 198-199.

[73] H.C. Hottel, A.F. Sarofim, W.H. Dalzell, I.A. Vasalos, Optical Properties of Coatings Effect of Pigment Concentration, AIAA Journal, 9 (1971) 1895-1898.

[74] M.F. Modest, CHAPTER 9 - THE EQUATION OF RADIATIVE TRANSFER IN PARTICIPATING MEDIA, in: M.F. Modest (Ed.) Radiative Heat Transfer (Second Edition), Academic Press, Burlington, 2003, pp. 263-287.

[75] L. Rayleigh, Phil. Mag., in, vol. 12, 1881.

[76] G. Mie, Beiträge zur Optik trüber Medien, speziell kolloidaler Metallösungen, Annalen der Physik, 25 (1908) 377-445.

[77] G. Zizak, Flame Emission Spectroscopy : Fundamentals and Applications, in: the ICS Training Course on Laser Diagnostics of Combustion Processes, NILES, University of Cairo, Egypt, Nov. 18-22, 2000.

[78] M.F. Modest, CHAPTER 10 - RADIATIVE PROPERTIES OF MOLECULAR GASES, in: M.F. Modest (Ed.) Radiative Heat Transfer (Second Edition), Academic Press, Burlington, 2003, pp. 288-360.

[79] HITRANonline, HITRAN parameters http://hitran.org/docs/definitions-and-units/.

[80] L.S. Rothman, I.E. Gordon, A. Barbe, D.C. Benner, P.F. Bernath, M. Birk, V. Boudon, L.R. Brown, A. Campargue, J.P. Champion, K. Chance, L.H. Coudert, V. Dana, V.M. Devi, S. Fally, J.M. Flaud, R.R. Gamache, A. Goldman, D. Jacquemart, I. Kleiner, N. Lacome, W.J. Lafferty, J.Y. Mandin, S.T. Massie, S.N. Mikhailenko, C.E. Miller, N. Moazzen-Ahmadi, O.V. Naumenko, A.V. Nikitin, J. Orphal, V.I. Perevalov, A. Perrin, A. Predoi-Cross, C.P. Rinsland, M. Rotger, M. Šimečková, M.A.H. Smith, K. Sung, S.A. Tashkun, J. Tennyson, R.A. Toth, A.C. Vandaele, J. Vander Auwera, The HITRAN 2008 molecular spectroscopic database, Journal of Quantitative Spectroscopy and Radiative Transfer, 110 (2009) 533-572.

[81] J.R. Taylor, An introduction to error analysis, University Science Books, Sausalito, Calif., 1997.

[82] J. Stewart, Multivariable Calculus, 3rd ed., 1995.

[83] N.I.G. Physics, https://www.newport.com/t/grating-physics.

[84] C.H. Colwell, Resource Lesson: Thin Lens Equation, in, PhysicsLab.org. , 2015.

[85] M. Winter, Basics of Optical Techniques and Set-ups., ME 627 - Radiation Heat Transfer classnote, Univ. of Kentucky, Dep. of Mech. Eng., (Fall 2013).

[86] NIST-database, in, National Institute of Standards and Technology (NIST), 2017.

[87] M. Winter, R. Bickel, D.P. Sekulic, H. Koch, H. Fu, B. Butler, Spectral, Directional Emittance of Stainless Steel at Elevated Temperatures, submitted to AIAA Journal of Thermophysics and Heat Transfer, (July 2018).

[88] M.W.G. Winter, Emissionsspektroskopische Untersuchung der Umströmung von Probenkörpern in hochenthalpen Plasmaströmungen, in, Universität Stuttgart, 2006.

[89] P.M. Danehy, B.F. Bathel, C.T. Johansen, M. Winter, S.O. Byrne, A.D. Cutler, Molecular-Based Optical Diagnostics for Hypersonic Nonequilibrium Flows, in: E. Josyula (Ed.) Nonequilibrium Hypersonic Flows: Fundamentals and Recent Advances, American Insitute of Aeronautics and Astronautics (AIAA), 2015, pp. 343-470.

[90] C.J. Dasch, One-dimensional tomography: a comparison of Abel, onion-peeling, and filtered backprojection methods, Applied optics, 31 (1992) 1146-1152.

[91] M. Winter, D. Prabhu, Excited State Chemistry in the Free Stream of the NASA IHF Arc Jet Facility Observed by Emission Spectroscopy, in: 42nd AIAA Thermophysics Conference, American Institute of Aeronautics and Astronautics, 2011.

[92] B. Ma, S. Cao, D. Giassi, D.P. Stocker, F. Takahashi, B.A.V. Bennett, M.D. Smooke, M.B. Long, An experimental and computational study of soot formation in a coflow jet flame under microgravity and normal gravity, Proceedings of the Combustion Institute, 35 (2015) 839-846.

[93] H. Guo, J.A. Castillo, P.B. Sunderland, Imaging Measurements of Soot Temperature and Volume Fraction in Flames, in, 2013.

[94] B. Ma, G. Wang, G. Magnotti, R.S. Barlow, M.B. Long, Intensity-ratio and color-ratio thin-filament pyrometry: Uncertainties and accuracy, Combustion and Flame, 161 (2014) 908-916.

[95] P.B. Kuhn, B. Ma, B.C. Connelly, M.D. Smooke, M.B. Long, Soot and thin-filament pyrometry using a color digital camera, Proceedings of the Combustion Institute, 33 (2011) 743-750.

[96] P.A.M. Kalt, M.B.Long, OMA-Image Processing for Mac OS X., www.oma-x.org, (2010).

[97] R.C. Sumner, Processing RAW Images in MATLAB, https://rcsumner.net/raw_guide/RAWguide.pdf, (2014).

[98] S. Eddins, Tips for reading a camera raw file into MATLAB, http://blogs.mathworks.com/steve/2011/03/08/tips-for-reading-a-camera-raw-file-into-matlab/, (2011).

[99] Adobe Systems Inc. Digital Negative Specifications, http://wwwimages.adobe.com/www.adobe.com/content/dam/Adobe/en/products/photoshop/pdfs/dng_spec_1.4.0.0.pdf, (2012).

[100] International Sooting Flame (ISF) Workshop, category ISF-3 Co-flow 3, http://www.adelaide.edu.au/cet/isfworkshop/data-sets/laminar/, (2015).

[101] S. Nakaya, T. Funahashi, Y. Asakami, I. Fujio, S. Takahashi, M. Tsue, Thermometry of combustion gas measuring two-band near-infrared emissions less than 1.1 μm from water molecules, Experimental Thermal and Fluid Science, 94 (2018) 1-8.

[102] Z. Diao, K. Saito, M. Winter, T. Hirasawa, Structure of Six Clustered Methane-Air Diffusion Microflames, in: Eighth International Symposium on Scale Modeling (ISSM-8), Portland, Oregon, USA, Sept. 12-14, 2017.

[103] S. Karnani, D. Dunn-Rankin, Visualizing CH^* chemiluminescence in sooting flames, Combustion and Flame, 160 (2013) 2275-2278.

[104] R.W. Schefer, Flame Sheet Imaging Using CH Chemiluminescence, Combustion Science and Technology, 126 (1997) 255-279.

[105] C. Park, Nonequilibrium hypersonic aerothermodynamics, John Wiley and Sons, New York, 1989.

[106] J. Luque, D.R. Crosley, LIFBASE: Database and spectral simulation (version 1.5), in, SRI International Report MP 99-009, 1999.

[107] E.E. Whiting, C. Park, Y. Liu, J.O. Arnold, J.A. Paterson, NEQAIR96,Nonequilibrium and Equilibrium Radiative Transport and Spectra Program: User's Manual, in, NASA Ames Research Center; Moffett Field, CA United States, 1996.

[108] G.M. Kibler, T.F. Lyon, M.J. Linevski, V.J. Desantis, Refractory material research, in, Technical Report No. WADD-TR-60-646 Part IV, 1964.

[109] J.G.S. Moo, Z. Awaludin, T. Okajima, T. Ohsaka, An XPS depth-profile study on electrochemically deposited TaO_x, Journal of Solid State Electrochemistry, 17 (2013) 3115-3123.

[110] Y. Kato, T. Hirasawa, Z. Diao, M. Winter, Characteristic of Seeded Particle Oxidation by Clustered Six Microflames, in: Proceedings of the Fifty-Fifth Symposium on Combustion, Toyama, Japan, Nov. 13-15, 2017.

[111] F. Rubio, J.M. Albella, J. Denis, J.M. Martinez-Duart, Optical properties of reactively sputtered Ta_2O_5 films, Journal of Vacuum Science & Technology, 21 (1982) 1043-1045.

[112] M. Winter, H. Koch, J. Beyer, Characterization of a 10.5 kW RF-Plasma Generator by Optical Methods, in: 2018 AIAA Aerospace Sciences Meeting, American Institute of Aeronautics and Astronautics, 2018.

[113] M. Winter, R. Green, C. Borchetta, E. Josyula, J.R. Hayes, J.S. Jewell, B. Hagen, Experimental Investigation of Image Distortion in a Mach 6 Hypersonic Flow, in: 2018 Aerodynamic Measurement Technology and Ground Testing Conference, American Institute of Aeronautics and Astronautics, 2018.

VITA

Zhaojin Diao

Education

Northeastern University, Boston, MA, USA
M.S., Mechanical Engineering *09/2009 - 08/2011*
Shanghai University of Electric Power, Shanghai, China
B.S., Thermal Engineering *09/2005 - 06/2009*

Peer Reviewed Publications

1. **Zhaojin Diao**, Michael Winter, Taro Hirasawa, Yuichi Kato, Yojiro Ishino and Kozo Saito, *Characterization of Six Clustered Methane-Air Diffusion Microflames through Spectroscopic and Tomographic Analysis of CH^* and C_2^* Chemiluminescence*, International Journal of Experimental Thermal and Fluid Science. (*submitted*)
2. **Zhaojin Diao**, Michael Winter, Taro Hirasawa, and Kozo Saito, *Characterization of the Thermal Structure of Six Clustered Microflames Seeded with TaN Particles through Emission Spectroscopy*, International Journal of Experimental Thermal and Fluid Science, Volume 96, September 2018, Pages 295-302.
3. **Zhaojin Diao**, Kozo Saito, Michael Winter and Taro Hirasawa, *Structure of Six Clustered Methane-Air Diffusion Microflames*, Proceedings of the 8th International Symposium on Scale Modeling (ISSM-8), Portland, Oregon, USA, Sept. 12-14, 2017. (*accepted for Progress in Scale Modeling*)
4. M. Winter, B. Butler, P.M. Danehy, S. Splinter, **Z. Diao**, F. Panerai, A. Martin, and S. Bailey, *Characterization of Ablation Product Radiation Signatures of PICA and FiberForm*, the 46th AIAA Thermophysics Conference (AIAA 2016-3233).

Conference Proceedings

1. Yuichi Kato, Taro Hirasawa, **Zhaojin Diao**, Michael Winter, *Characteristic of Seeded Particle Oxidation by Clustered Six Microflames*, Proceedings of the 55th Symposium (Japanese) on Combustion, Toyama, Japan, Nov. 13-15, 2017.
2. Yuichi Kato, Taro Hirasawa, **Zhaojin Diao**, Michael Winter, Yojiro Ishino, *Three-Dimensional Flame Structure and Characteristics of Heating Particles in Methane Clustered Microflames on Six Fuel and One Air Jets*, Proceedings of the Annual Conference of the Japan Institute of Energy, Nagoya, Japan, Aug. 1-2, 2017.
3. **Zhaojin Diao**, Michael Winter, Taro Hirasawa, and Kozo Saito, *Characterization of Microflame Burner Designs Seeded with TaN Particles through Emission Spectroscopy*, the 10th US National Combustion Meeting, College Park, Maryland, USA, April 23-26, 2017.
4. Taro Hirasawa, **Zhaojin Diao**, Michael Winter, *CH^* Emission and Thermal Characteristics of Clustered Microflames on Six Fuel and One Air Jets*, Proceedings of the 54th Symposium (Japanese) on Combustion, Sendai, Japan, Nov. 23-25, 2016.
5. Taro Hirasawa, **Zhaojin Diao** and Michael Winter, *A Study on Heating of Particles by Methane Clustered Microflames and Its Flame Structure*, Proceedings of the Thermal Engineering Conference 2016, Matsuyama, Japan, Oct. 22-23, 2016.
6. **Zhaojin Diao**, Michael Winter, Taro Hirasawa, and Kozo Saito, *Characterization of a Methane-Air Diffusion Microflame with Seeding Particles through Emission Spectroscopy*, 2016 Spring Technical Meeting Central States Section of the Combustion Institute, Knoxville, Tennessee, USA, May 15-17, 2016.
7. Michael Winter, **Zhaojin Diao**, Tianxiang Li, *A Novel Approach to Measuring Soot Concentration with Spectroscopic Methods*, 2015 Spring Technical Meeting Central States Section of the Combustion Institute, Cincinnati, Ohio, USA, May 17-20, 2015.